Gaze Control in a Dynamic Paradigm of Head-in-space Orientation

Dissertation

zur

Erlangung der naturwissenschaftlichen Doktorwürde

(Dr. sc. nat.)

vorgelegt der

Mathematisch-naturwissenschaftlichen Fakultät

der

Universität Zürich

von

Jakob Skibsted Thomassen

aus

Dänemark

Promotionskomitee

Prof. Dr. Kevan A. C. Martin (Vorsitz)

Prof. Dr. Bernhard J. M. Hess (Leitung der Dissertation)

Prof. Dr. Peter Thier

Zürich, 2011

Table of Content

Summary

The oculomotor system is one of the most thoroughly studied motor systems. Its prime function is to control and steer gaze in space, which requires not only controlling the eye in head but also involves control of the composite orientation of eye, head, and body relative to space. Detailed studies of the complex composite movements and orientations of eye, head and body have only more recently begun with the development of computer-controlled multi-axes motion devices and appropriate multi-dimensional recording and analysis techniques. This thesis presents a new technology, that has been developed to cope with problems arising when measuring both eye and head movements in head-unrestrained subjects on a multi-axes turn chair. Turn chairs are widely used in oculomotor and vestibular research to passively move subjects while measuring eye movements. This dissertation presents a new technique for recording eye and head movements in all degrees of freedom and demonstrates its application in a study of head orientation and coordination of eye and head during an active and a passive motion paradigm. In the active paradigm, the subjects were required to track the circular motion of a target whereas in the passive paradigm they had to fixate a stationary target during a similar circular passive self-motion.

Chapter 1 provides a general introduction to the field of vestibuloocular research explaining some of its most basic functions. It introduces the reader to the physiology of the vestibular organs and describes the basic anatomy of the oculomotor plant as well as some kinematic rules of the eye such as Listing's law. Furthermore it provides a short introduction to the algebraic representation of rotations used in the thesis in addition to a few pertinent mathematical tools. Finally the most widely used method of 3D (three-dimensional) eye movement recording, the scleral search coil technique, is explained, which is essential for understanding the description of the newly developed expansions to this technique.

Chapter 2 is a reprint of the article “Decoding 3D search coil signals in a non-homogeneous magnetic field” (Thomassen, Benedetto & Hess, 2010). This work extends the range of applications of the search coil technique in which the orientation of a small sensor coil (attached to the eye) is measured in an ambient magnetic field provided by a frame of large primary field coils. In brief, this technique depends on the currents inducted in the sensor coil as a function of its angular orientation relative to the primary field. Originally, the technique has been dependant on keeping the subject within the center of the frame, where the magnetic field is linear. To achieve this, either the head of the subject had to be restraint or very large frame coils had to be used. In the here presented technique the non-linearity of the field is taken into account by calculating the field geometry using the Biot-Savart law. This approach allows recording 3D eye movements with small frame coils even if the head is unrestrained. The technique is evaluated by simulations as well as by *in vivo* experiments, in which trained rhesus monkeys fixated targets with the head free to move. The experiments showed that the new procedure significantly improved both accuracy and precision of the eye movement recording.

In Chapter 3 the new recording technique is used to study head-unrestrained gaze control in four rhesus monkeys by focusing on relatively small gaze movements in a periprimary range of ±15°. Previously it has been shown that during large eye–head saccades the head has a preference for contributing in the horizontal direction while the eye rotates more in the vertical direction. Furthermore, it has been shown that the three-dimensional head orientation between these saccades tends to follow a specific restraint that keeps the inter-ocular axis more aligned with the horizon. Confirmation or rejection if this behavior also holds for small gaze movements could provide important information about the underlying mechanisms. The results from the eye–head coordination study provided conclusive evidence for direction specificity similar to that found in large eye–head saccades, suggesting that this strategy is of static (anatomical) rather than dynamic origin. The results on head orientation revealed a different strategy

regarding the head contribution compared to large eye–head gaze movements: these relative small gaze movements resembled the behavior of eye movements which follow Listing's law, suggesting that the tendency to keep the inter-ocular axis horizontally is overruled by a strategy that optimizes the kinematics of the head movement.

Zusammenfassung

Das okulomotorische System ist eines der am besten untersuchten motorischen Systeme. Es kontrolliert die Blickrichtung (line of sight), welche nicht nur von der Position des Auges in der Orbita abhängt, sondern sich aus der Ausrichtung von Körper, Kopf und Auge zusammensetzt. Detaillierte Untersuchungen dieser komplexen Bewegungen haben erst in jüngerer Zeit mit der Entwicklung geeigneter Instrumente begonnen. Die vorliegende Arbeit stellt eine neu entwickelte Technologie vor, welche die Messung von Augenbewegungen bei frei beweglichem Kopf auf einem speziell dafür modifizierten Drehstuhl ermöglicht. Drehstühle werden normalerweise zur Durchführung von Ganzkörper-Rotationen bei okulomotorischen und vestibulären Untersuchungen der Augenbewegungen verwendet. Diese Arbeit stellt die neue Messtechnik vor und zeigt ihre Anwendung beim Studium von Augen-Kopf-Koordination und Kopf-Orientierung bei Probanden, die aktiv ein visuelles Ziel verfolgen oder während passiven Eigenbewegungen fixieren möchten.

Das erste Kapitel dieser Arbeit gibt eine allgemeine Einführung in die vestibulokuläre Forschung und erklärt die grundlegenden Prinzipien. Es führt den Leser in die Anatomie des okulomotorischen Apparates sowie in die Physiologie des Vestibularorgans ein und erklärt die kinematische Beschreibung einiger Regeln des Auges wie zum Beispiel das Listingsche Gesetz. Zusätzlich zu den verwendeten mathematischen Werkzeugen wird die Drehungsdefinition vorgestellt, welche in vorliegender Arbeit verwendet wird. Schließlich wird die herkömmliche Methode zur Messung von Augenbewegungen, die sklerale Sensorspulentechnik, erklärt, welche für das Verständnis der neuen, erweiterten Technik grundlegend ist.

Kapitel 2 ist ein Nachdruck des Artikels, "Decoding 3D search coil signals in a non-homogeneous magnetic field" (Thomassen, Benedetto & Hess, 2010), welcher die neue, erweiterte Anwendung der skleralen Sensorpulentechnik im

Detail vorstellt. Bei der skleralen Sensorspulentechnik wird die Winkelorientierung einer kleinen Spule gemessen, die auf der Lederhaut (der Sklera) des Auges des Probanden angebracht ist. Der in der Sensorpule induzierte Strom entspricht dem Verhältnis ihrer Winkelorientierung zu einem oder mehreren magnetischen Wechselfeldern, die mittels möglichst großen Spulen erzeugt werden. Bei Anwendung der originalen skleralen Sensorspulentechnik befindet sich die Versuchsperson in der Mitte eines von relativ grossen Spulen erzeugten Feldes, wo der Strom konstant und linear verläuft, wobei der Kopf der Versuchsperson stabilisiert wird. Die in dieser Arbeit vorgestellte Erweiterung der Technik ermöglicht erstmals die Messung von Augenbewegungen mit kleinen Feldspulen bei frei beweglichem Kopf des Probanden, indem die Nichtlinearität des magnetischen Feldes mittels des Biot-Savart Gesetzes kompensiert wird. Evaluiert wurde die Technik durch Simulationsversuche sowie in *in vivo* Experimenten mit einem relativ kleinen Magnetspulensystem. Die Ergebnisse zeigen, dass die neue Technik die Genauigkeit und Präzision der Messung von Augenbewegungen signifikant verbessert.

In Kapitel 3 wird mit der neuen, erweiterten Technik die Blickkontrolle von vier Rhesusaffen bei frei beweglichem Kopf im periprimären Sehbereich (± 15°) studiert. In früheren Studien hatte sich gezeigt, dass der Kopf bei großen Augen-Kopf-Sakkaden primär einen Beitrag in horizontaler Richtung liefert, während das Auge bevorzugt zur vertikalen Bewegung beiträgt. Darüber hinaus hatte sich gezeigt, dass die Orientierungen des Kopfes dem Donderschen Gesetz folgen, wobei sich die interokuläre Achse möglichst nach der Horizontalen ausrichtet. Eine Verifizierung oder Falsifizierung dieser Befunde für Augenbewegungen innerhalb des periprimären Bereiches kann wichtige Informationen über die zugrunde liegenden Mechanismen liefern. Die Ergebnisse dieser Arbeit zeigen, dass die Augen-Kopf-Koordination im periprimären Sehbereich ähnlich wie bei grossen Augen-Kopf-Sakkaden richtungsspezifisch organisiert ist. Dies lässt vermuten, dass die Koordination statischen (anatomischen) Ursprungs ist und

nicht einem neural gesteuerten dynamischen Muster folgt, etwa um Energie zu sparen. Andererseits weisen die Befunde der Kopforientierungsstudie auf ein Kontrollmuster der Kopfbewegungen im periprimären Bereich hin, welches dem Verhalten von Augenbewegungen gemäss dem Listingschen Gesetz entspricht. Dies lässt vermuten, dass die Optimierung der Bewegungen wichtiger ist als eine möglichst horizontale Ausrichtung der interokulären Achse.

Acknowledgements

The work I have accomplished during the last four and a half years and resulting in this dissertation has been done with help of several people.

First and foremost I would like to thank my supervisor Prof. Bernhard Hess for always taking time for discussions, for motivating and for giving me the opportunity to join the Zürich Vestibulo-Oculomotor Lab.

My special gratitude goes to Bernadette Disler for friendship and assistance during the first years of this work. Her expertise at animal care was invaluable and likewise the amusement on the skiing slopes. Many thanks go also to Urs Scheifele for his help with the experimental setup, programming control software, construction of hardware and for his helpful and entertaining discussions about topics such as geometry, programming, hardware and even astronomy.

I would also like to thank Albert Zuger, Carla Bettoni, Elena Buffone and Marco Penner for their technical assistance and the rest of the present and former members of the Zürich Vestibulo-Oculomotor Lab for friendship and interesting discussions.

My gratitude goes also to Prof. Kevan Martin and Prof. Peter Thier for taking part in my thesis committee and to Dr. Daniel Kiper for taking part in the examination at my thesis defense. I am also very thankful for the financial support from the European Commission's Marie-Curie Actions (FP6) under Contract Number: MEST-CT-2004-007825 and the Betty and David Koetser Foundation.
Finally, I would like to thank my family, girlfriend and friends for their support and patience, especially during the last phases of this work.

Disclaimer

All animal experiments and procedures were performed according with the NIH Guide for the Care and Use of Laboratory Animals and were approved by the Veterinary Office of the Canton of Zürich.

Surgeries were performed by Prof. Bernhard Hess and assisted by either Dr. Tamara Tchelidze, Dr. Jean Laurens or myself. Animal care was carried out by the Biologisches Zentrallabor at the University Hospital Zürich along with Bernadette Disler and Carla Bettoni.

The main experimental setup (motion device and eye movement recording hardware) was build by lab personnel and modified by myself. Early investigation in unrestrained head movement recording was made by Giacomo Di Benedetto.

All data presented in this thesis and the preceding animal training were collected and performed by myself. The Matlab software for data analysis was written by me with exception of the standard build in functions and Spike2 software for data acquisition written by Urs Scheifele.

All figures and illustrations are made by myself unless otherwise stated.

1. General Introduction

The human brain continues to inspire scientist and engineers. This organ of approximately 1500 grams of fatty tissue with up to as many as one hundred billion nerve cells is believed to be the most complex composition known to man.

One of the most important tasks of this structure is to acquire and react to various stimuli around us. The most vital of these systems in the primate is the visual system. Of all the senses, this is believed to be the most prominent and evolved and to occupy most of the brain.

The path of information begins with photons entering the eye through the cornea and the lens where they are refracted to the photoreceptor cells of the retina. The information is then transformed to electro-chemical pulses and led through the optic nerve to the brain. However, only a small part around the center of the primate retina, the fovea, has high visual acuity that is necessary for tasks like reading or tracking a moving object. To redirect this foveal vision, called line of sight, the eye makes use of the six oculomotor muscles situated behind the eye in the ocular orbit (Figure 1-1). Of these the lateral- and medial rectus control horizontal movements while the superior- and inferior rectus along with the superior- and inferior oblique control vertical and torsional movements.

Eye movements have long been studied in static laboratory setups within simple environments and have resulted in a vast amount of knowledge about visual control. Although research with these setups continues to be important since the various processes involved are still not fully understood, the movement of the eyes in their sockets is only a subsystem of visual control and usually does not fully account for the control of the line of sight during natural behavior. For the moving body the control of the line of sight relies on control of different reference frames embedded within each other; the eyes move within the

reference frame of the head while the head moves within the reference frame of the thorax and so on. Thus, the line of sight is the product of movements of many different body parts all controlled by the brain.

In order to efficiently control vision during these complex movements the brain uses not just the feedback from the visual input but also sensation of head movement. This is acquired from the vestibular organs and is an important input for the brain to stabilize the line of sight relative to space.

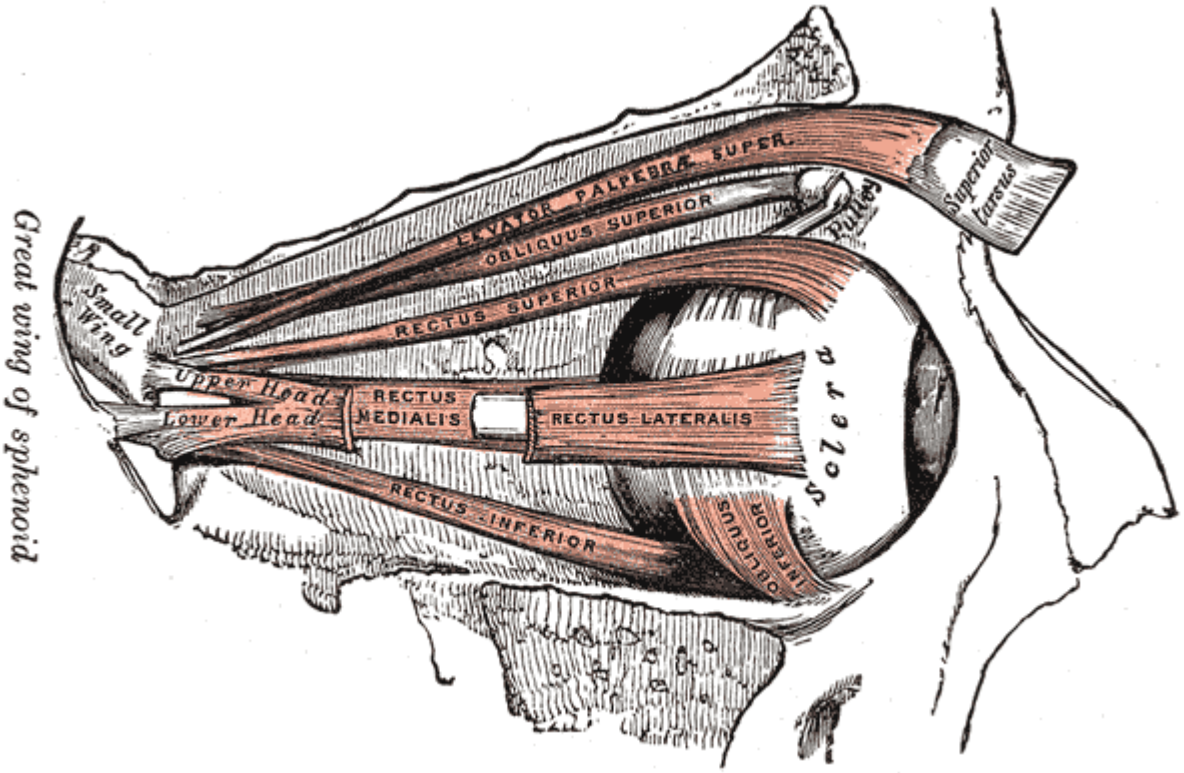

Figure 1-1. The six extraocular muscles in the orbit.
(From Gray, 1918).

1.1 The vestibular system

One important task for animals that move in their environment is to regulate their orientation relative to external forces such as gravity or self-induced forces such as those produced during locomotion. The primary functions of the vestibular system are to help keeping balance, to stabilize vision and to update spatial orientation.

Two peripheral receptor organs are located in the inner ear at each side of the head and each consists of five separate components. Three nearly mutually orthogonal semicircular canals detect angular head motion while two otolithic organs – the utricle and the saccule – detect linear head motion and gravity (see Figure 1-2).

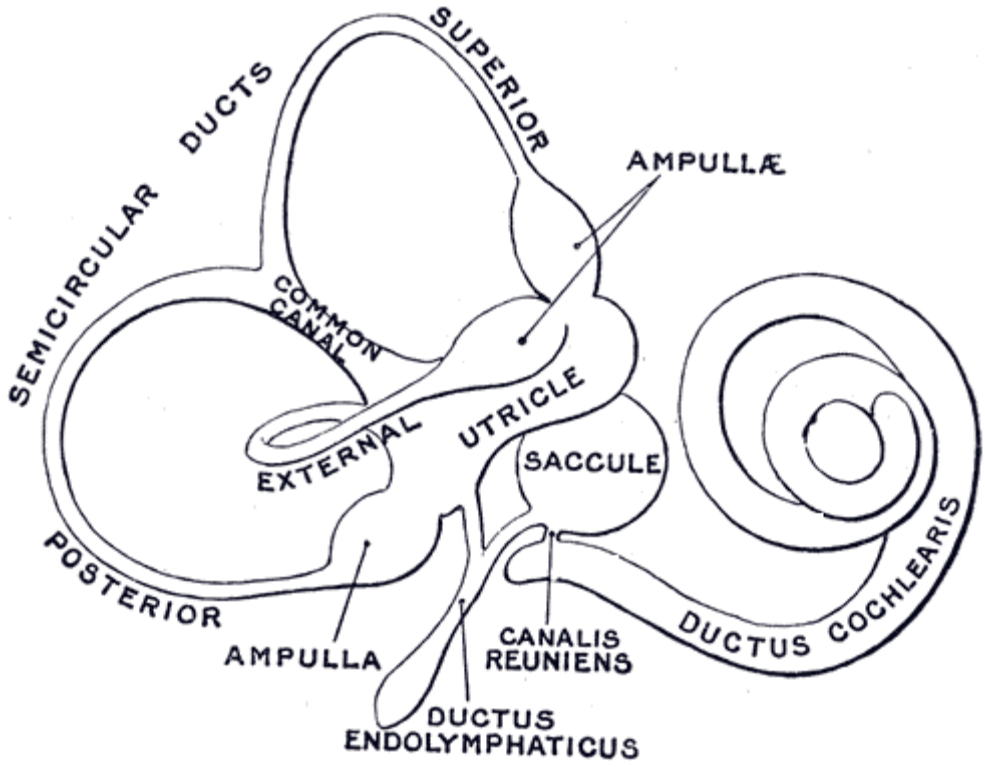

Figure 1-2. The right membranous labyrinth viewed from the anterolateral aspect. (From Gray, 1918).

1.1.1 The semicircular canals

The three canals are oriented roughly so that the lateral (external) canal is maximally sensitive to head movements around a vertical axis (yaw movement) when the head is tilted 30° downwards, while the superior (anterior) and posterior canals are orthogonal to the lateral canal and each approximately 45° from the interaural axis and the naso-occipital axis. This makes the latter two canals sensitive to both downwards (pitch) and sideways (roll) movements.

Each canal consists of a tube, named duct, filled with a fluid called endolymph. At one end there is an enlargement, the ampulla, where sensitive hair cells located in the crista project into a cupula which works as a flexible membrane that stops the endolymph from flowing past (McLaren & Hillman, 1976). When the labyrinth rotates along with the head, the inertia of the endolymph will exert a pressure on the cupula causing it to bend and thereby stimulate the hair cells, which in turn connect to vestibular afferent cells that send the signal to the brain via the vestibular branch of the 8th cranial nerve.

Each hair cell has several 'hairs', called stereocilia, that are arranged with shorter ones at one side of the cell, and increasing in length towards the other end with the last one, called kinocilium being the longest. When the cupula deflects, the hairs will bend either towards the kinocilium or away from it, depending on the direction of the head rotation. The cell is polarized so that when the stereocilia are bended towards the kinocilium the cell will depolarize and thereby cause excitation (i.e. increased rate of action potentials). Bending away from the kinocilium will hyperpolarize the cell and thereby cause inhibition (decreased rate of action potentials).

The canals are set up so that the two lateral canals on each side are roughly parallel but mirrored. This creates a push-pull relationship where leftward rotations of the head will cause depolarization of the hair cells in the left lateral canal and hyperpolarization of the hair cells in the other while rightward rotations will reverse the relationship. The same relationship applies to the

superior and posterior canals although they are cross-paired since the left superior canal is parallel with the right posterior canal and vice versa.

The advantage of the push-pull relationship is increased sensitivity because neurons in the vestibular nuclei receive the signal from each side of the head and compare the firing rates. This way the sensitivity is theoretically doubled and slower head rotations can be detected.

The deflection of the cupula caused by head rotation acts as an *acceleration* transducer since the inertial force from the endolymph on the cupula is created by conservation of momentum. However, due to the dynamics of the endolymph flow this is only the case for very low frequencies where the system's sensitivity is low. During higher frequencies (> 1 Hz), where the vestibular system plays a more important role, the deflection encodes the *velocity* of the head. At even higher frequencies above the naturally occurring head movements (>20 Hz, Grossman, Leigh, Abel, Lanska & Thurston, 1988) the encoding starts to act as a position transducer.

The integrating property from acceleration to velocity can be shown by calculating the fluid mechanics with the Navier-Stokes equations of the viscous drag of the endolymph on the wall of the duct, while other models include estimations of the elastic property of the cupula which defines the second integration at high frequencies (Van Buskirk, Watts & Liu, 1976; Grant, 1999). A torsion pendulum model early proposed by Steinhausen (1933), describes the general idea. Its dynamic follows the second-order transfer function for a band-pass filter:

$$TF(s) = K \frac{s}{(1+\tau_1 s)(1+\tau_2 s)} \tag{1-1}$$

where s is the Laplace operator and τ_1 and τ_2 are the time constants defining the lower and upper cut-off frequencies originating from the viscous drag and the cupula elasticity. Figure 1-3 shows a bode plot relative to head velocity for the transfer function with parameters from Fernandez & Goldberg (1971). It is seen

that for the range of natural head movements, the semicircular canal encodes head *velocity*, as indicated by the near zero phase. For slow head movements it encodes acceleration as indicated by the 90 degree phase shift but the magnitude is attenuated. The position encoding for higher frequencies is shown to be of only minimal influence for natural head movements.

The above description assumes that the deflection of the cupula is proportional to the discharge of the hair cell afferents (see e.g. Yamauchi, Rabbitt, Boyle & Highstein, 2002). Furthermore, it should be noted that the three canals have some interaction via their shared endolymph in the utricle (Rabbitt & Damiano, 1992).

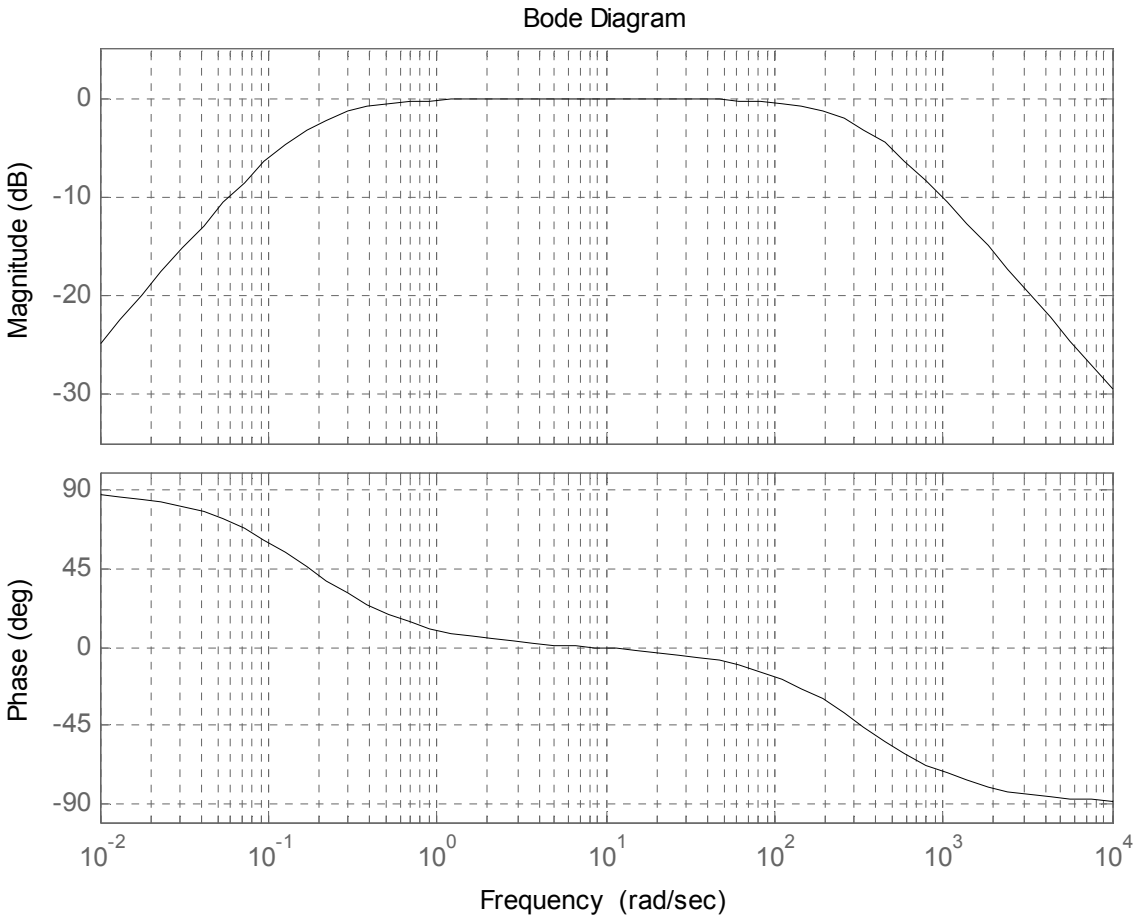

Figure 1-3. Bode plot of the transfer function of a semicircular canal re velocity.

For natural head movements the semicircular canal works as a velocity transducer. (Parameters from Fernandez & Goldberg, 1971).

1.1.2 The otolith organs

The two otolith organs, the utricle and the saccule, are inertial motion sensors like the three semicircular canals. They are, however, unlike the semicircular canals sensitive to linear acceleration. A constant source of linear acceleration is the gravitational force. Other linear movements such as horizontal acceleration like the ones occurring when speeding up or breaking with a car or vertical acceleration like the ones occurring while jogging or riding an elevator are superimposed on the gravitational force (Einstein's equivalence principle: gravitational and inertial forces are indistinguishable) and the result, the gravitoinertial force, is sensed by the otoliths.

The otolith organs are situated between the semicircular canals and the cochlea. They are mostly flat layered structures that lie inside the labyrinth and are directed so that the utricle is mainly sensitive to accelerations in the horizontal plane while the saccule mainly has vertical sensitivity.

Like in the ampullae of the semicircular canals, there are polarized hair cells embedded in a structure, here called the macula. However, their stereo- and kinocilia project into a flexible gel layer in which otoconia are embedded, i.e. crystals made of calcium carbonate which have a higher mass density than the surrounding endolymph. This way the otoconia will be displaced when the gravitoinertial force acts in the plane of the organ and the underlying stereocilia of the hair cells will be bended along with the shearing deformation of the gel layer.

In contrast to the hair cells in the semicircular canals, the macular hair cells are not all maximally sensitive to the same direction. Both the utricle and the saccule have a deformation, called striola, where the hair cells on each side are oppositely directed. In the utricle the kinocilia of the hair cells point towards the striola while in the saccule the kinocilia point away from the striola. Because the striola is curved, the hair cells are sensitive in many directions. This way each organ effectively maps the acceleration in more than just one direction. This

differentiation is preserved and mediated to the brain via the vestibulocochlear nerve.

The otoliths can be seen as acceleration transducers for normal head movements. The transfer function can be simplified to a first-order low-pass filter:

$$TF(s) = K \frac{1}{(1+\tau_1 s)} \tag{1-2}$$

where τ_1 is the cut-off frequency.

For more complex models of the transfer function see e.g. Fernandez & Goldberg (1976) or Grant (1999). Figure 1-4 shows a bode plot relative to linear head acceleration with parameters from Crane & Demer (1999).

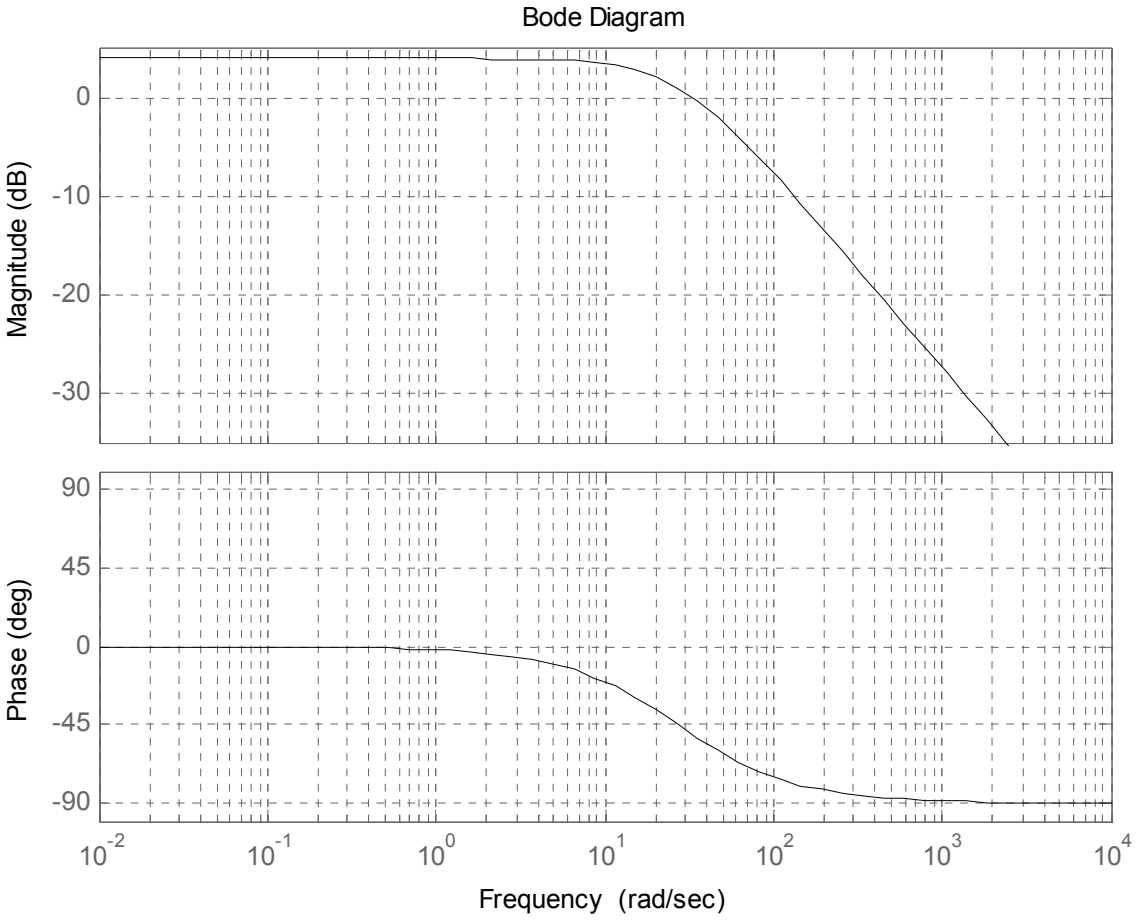

Figure 1-4. Bode plot of the transfer function of an otolith organ re acceleration.

For natural head movements the organ works as an acceleration transducer. (Parameters from Crane & Demer, 1999).

1.2 The vestibulo-ocular reflex

As mentioned, one of the most important functions of the vestibular system is to stabilize our vision during head movement. This function is facilitated by the vestibulo-ocular reflex (VOR). When the head moves, the eyes will move in their sockets in such a way that the eye relative to a stationary target will remain fixed. This reflex involves both the semicircular canals and the otoliths; when the head rotates around some imaginary axis and the canals are stimulated, the eyes will rotate around an axis parallel to that, but in the opposite direction (rotational VOR or rVOR), and if the head is translated and thus the otoliths stimulated, the eyes will rotate appropriately depending on the distance to the target so that the eyes will remain fixed on the target (translational VOR or tVOR, see e.g. Angelaki, 2004).

The rVOR is processed very fast by the brain by a pathway called the 'three-neuron arc'. This enables a latency of only about 8 ms for the head rotation stimulus to go through the brainstem to the eye muscle (Tabak, Collewijn, Boumans & van der Steen, 1997). For comparison, the feedback loop of the visual system is at least one order of magnitude slower.

The first of the three neurons are the primary afferents of the semicircular canals, which connect to the second order neurons in the vestibular nuclei of the brainstem via the 8th cranial nerve. The axons from these neurons cross the midline and contact motor neurons in the contra-lateral abducens nuclei that project to the lateral rectus muscle of the ipsilateral eye and to internuclear neurons, which in a second pathway project to the contralateral medial rectus muscle. As mentioned, the canals work in a push-pull relationship so for rightwards rotation the right canal will activate agonist muscles that pull the eye to the left (i.e. the left lateral and via internuclear pathway the right medial rectus) while the left canal will impede the antagonist muscles (i.e. the right lateral and left medial rectus).

However, it is important to note that the eyes can not be fully controlled by velocity signals alone. Because of the elasticity of the orbital tissues, the eyes would seek towards a neutral position straight ahead if not provided with a tonic signal to hold them in place. This function is provided by a neural integrator that performs a mathematical integration of the velocity signals into position signals (Robinson, 1968). It was shown by Cohen & Komatsuzaki (1972) that stimulation upstream of the integrator in the reticular formation produced eye movements with constant velocity and thus an integration of the stimulus signal necessary for the buildup of the tonic signal to the motoneurons. The location of these neural integrators are different for horizontal and vertical eye movements: whereas horizontal eye velocity is primarily integrated in the Nucleus Prepositus Hypoglossi (NPH) (Cannon & Robinson, 1987), the vertical (and torsional) eye velocity integration has been found to be located in the Interstitial Nucleus of Cajal (INC) (Crawford, Cadera & Vilis, 1991; Fukushima, 1991).

For large head rotations, e.g. if a person spins continuously on an office chair, it is clear that the eyes quickly will reach a natural limit of rotation in the head. This is defined by the oculomotor range and is for humans around ±45°. For continuous head rotation, the eyes are therefore resetting their position to fixate a new target in space. This involuntary eye movement, also called nystagmus, is often analyzed as two components; the VOR part, also called the slow phase and the resetting part, called the fast phase. For studying the properties of the VOR the slow phase is of particular interest. Figure 1-5A illustrates the horizontal eye position component of a VOR elicited in a macaque monkey by a sudden onset of continuous rotation in the dark around a vertical axis starting at time=0 s with a velocity of 30°/s. The slow phase is seen as the thick black line while the thin vertical lines are the fast phases (or saccades). Initially the slow phase nearly matches the rotation in terms of velocity, i.e. the gain is almost one. The exponential decay is predicted from the transfer function but the time constant of the decay is actually bigger than τ_1 of Equation (1-1). The nystagmus continues

for some time after the signal from the semicircular canals has decayed. This is because of a mechanism in the brainstem called velocity storage which helps prolong the control of the eyes (Raphan, Matsuo & Cohen, 1979). Figure 1-5B shows the response obtained when the rotation has been stopped (at time=230 s). This is called post rotatory nystagmus, which goes in the other direction because the endolymph has built up a momentum relative to space and therefore stimulates the semicircular canals in the opposite direction.

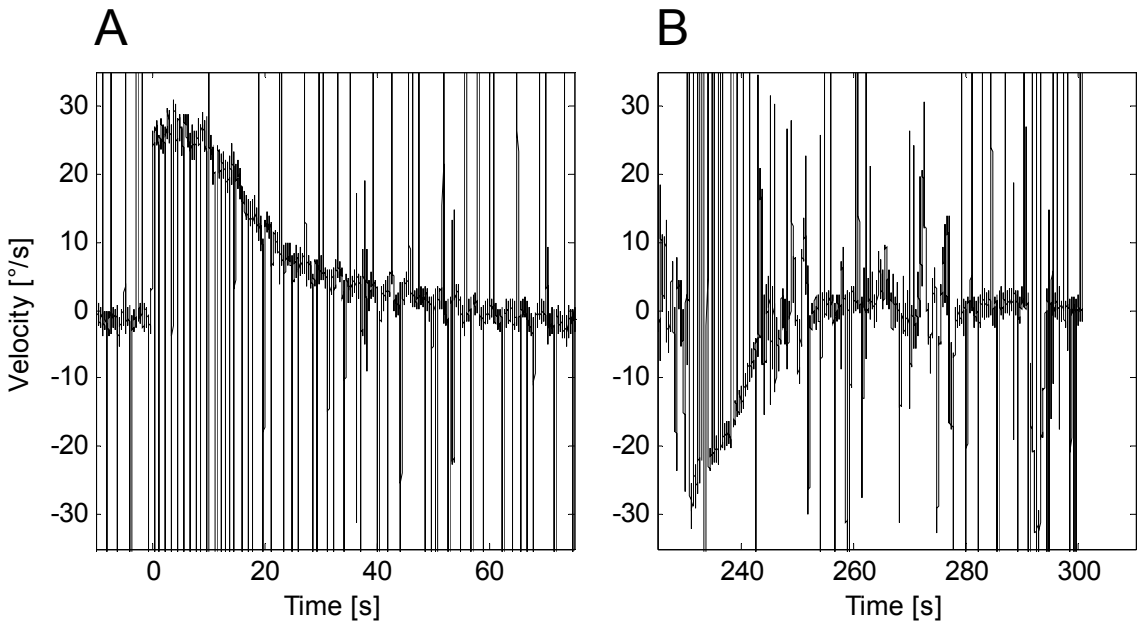

Figure 1-5. Vestibuloocular Reflex of a velocity step of 30°/s.

A: Slow-phase response to a step from zero to 30°/s. *B*: Response to a step from 30°/s to zero after steady state. Data from subject M3 (see also e.g. Waespe, Henn & Isoviita, 1980).

1.3 Eye-head coordination

Saccades

The eyes seek new visual targets by rotating the eyes with high acceleration and velocity also known as saccades. The horizontal position trace for a typical saccade made by a head movement-restrained macaque monkey is shown in Figure 1-6A. A primary saccade rotates the eye from the initial position at straight ahead towards the target at 20 degrees to the left (see section 1.4 for sign convention). However, the saccade lands short of the target and after around 250 milliseconds (ms) a new smaller saccade corrects the error. This shows that (1) the saccadic system is not always perfectly tuned and can often show some degree of dysmetria (under- or overshoot of the target also called hypo- or hypermetria) and (2) the system corrects or reduces this error by a second saccade and (3) the time it takes to correct the error and thus the latency from the error is projected on the retina to the eye muscles starts to rotate the eye is, in this case, around 250 ms (some saccades called express saccades can be performed somewhat faster (Fischer & Boch, 1983). The error is also called the retinal error and the second saccade is known as a corrective saccade.

Figure 1-6B shows the angular velocity corresponding to the eye position in Figure 1-6A. The velocity profiles are typically symmetrical and bell shaped or triangular with rounded corners although for large saccades (>25°) the profile becomes increasingly asymmetric with higher acceleration than deceleration (Van Opstal & Van Gisbergen, 1987).

It turns out that both the width and the height of this profile (or duration and peak velocity respectively) are close to linearly related to the amplitude of the saccade; higher amplitude gives higher peak amplitude and longer duration. This is also known as the main sequence (Bahill, Clark & Stark, 1975). The peak velocity will however be reached for saccades shorter than the oculomotor range and thus

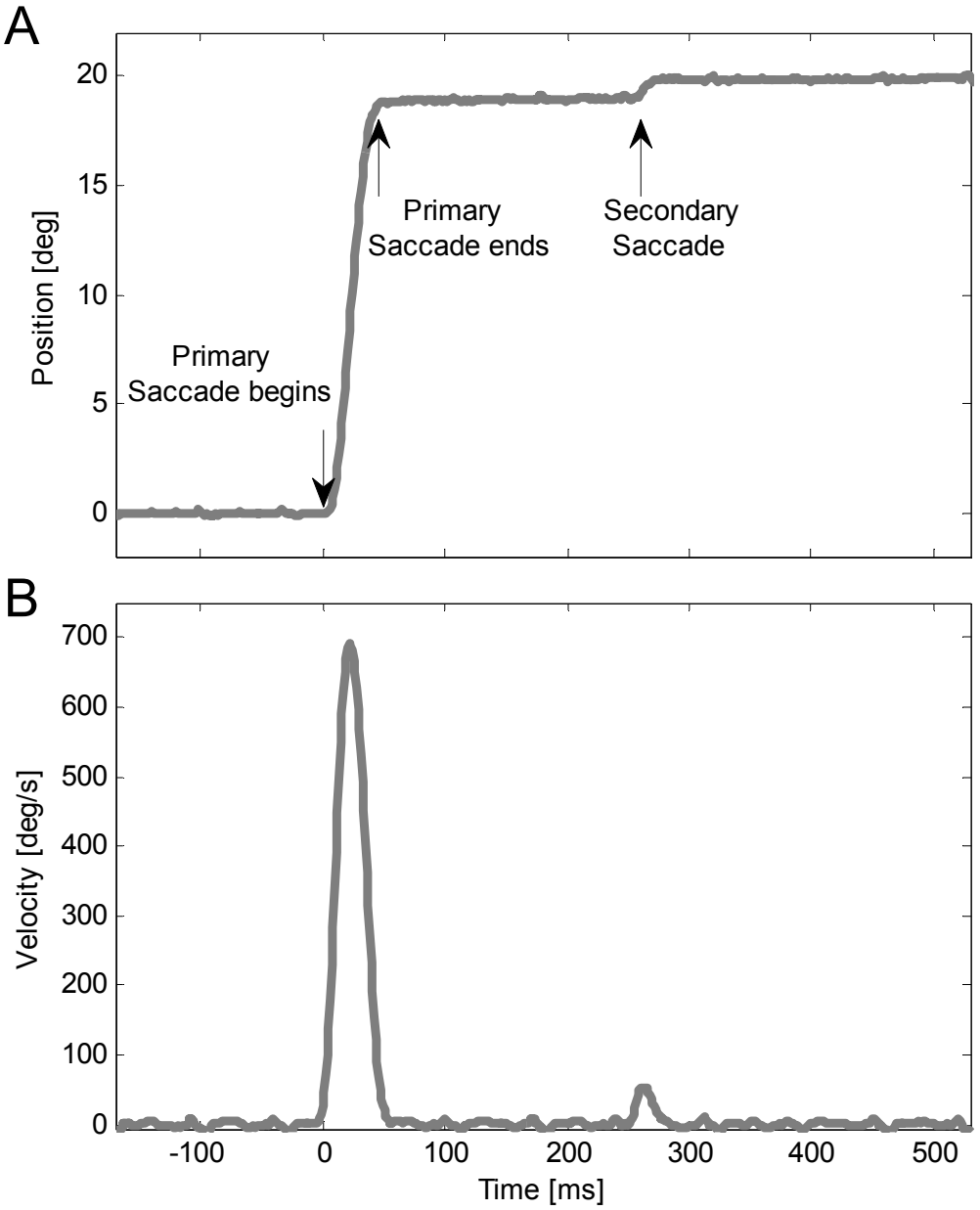

Figure 1-6. Typical saccade in the horizontal plane with the head restrained.

A: Horizontal position component of Primary- and secondary saccade. *B*: Horizontal angular velocity component. Data from subject M3 (see also Fig. 1 in Becker, 1989).

the linear relationship for peak velocity does not include saccades bigger than about 20°. For larger saccades the velocity saturates. For the relationship between

duration and amplitude the linearity seems to hold for the full range of saccade amplitudes (Baloh, Sills, Kumley & Honrubia, 1975).

When the head is free to move it often assists the eyes during gaze shifts. In the primate, the oculomotor range is around ±45°, so when reaching targets beyond this range head movement is an absolute necessity. However, the head also contributes when targets within the oculomotor range are pursued. For gaze shifts of more than 20° from the center of the oculomotor range the head starts to contribute linearly with gaze amplitude (Freedman & Sparks, 1997). Here, head contribution is defined as the amount of head movement during the gaze shift, that is, from the beginning of eye movement until the gaze has reached the target. Figure 1-7 shows a typical horizontal gaze shift made from straight ahead to 18° right with the head free to move. Like in the head restrained case the gaze shift, shown in dark gray, rapidly moves towards the target. The gaze shift is mostly accomplished by rotation of the eye, shown in black, and only very little head contribution (light gray) is performed before the gaze shift has ended and the target is reached. The total head movement, defined by the amplitude from the beginning to the end of head movement, is however relatively large in this case and fully compensates for the gaze shift. That amount of head movement for such a small gaze shift might be considered atypical, but, as shown in chapter 3 for smooth pursuit, the amount of head movement can have a high degree of variance for the same stimulus (see also spread in fig. 5B in Freedman, 2008).

The amount of head *contribution* depends not only on the amplitude of the gaze shift but also on the initial eye position relative to the head (Tomlinson & Bahra, 1986a; Stahl, 2001). The effect of initial eye position can be seen as an offset that can increase or decrease the amount of head contribution for some saccade amplitude. For example, if the eye is initially positioned at 20° right with the head at straight ahead and a 40° gaze shift to the left is performed, little or no head contribution is carried out since the final eye position is only 20° to the left. If however, both the eye and the head are initially positioned at straight ahead

and the 40° gaze shift to the left is performed, the head contribution would increase.

As mentioned above, higher gaze shift amplitude gives higher peak saccade velocity for head restrained saccades. For head unrestrained gaze saccades within 20° from the center of the orbit where head contribution is minimal, this relationship also holds. However, as head contribution becomes significant the peak saccade velocity declines. In fact, for gaze shifts of constant amplitude but with varying initial eye-in-head positions it has been shown that the duration-amplitude relationship of the saccade reverses (Freedman & Cecala, 2008).

From the above we have established that head contribution reduces the saccade velocity and elongates the duration. It is then tempting to think that the VOR is responsible for this velocity decline, but evidence have shown that the VOR is turned off during the saccade and that the effect even starts before the head movement begins, which indicates an interaction of head movement commands and saccade velocity (Tomlinson & Bahra, 1986b; Guitton & Volle, 1987; Lefevre, Bottemanne & Roucoux, 1992; Roy & Cullen, 1998). The VOR is however responsible for stabilizing the gaze during the terminal head movement after the saccade is finished and the target is fixated i.e. during most of the head movement shown in Figure 1-7. Gaze shifts in the vertical and horizontal directions have similar kinematic properties, but head contribution has been shown to be less in the vertical direction when considering large oblique head unrestrained gaze shifts (Tweed, Glenn & Vilis, 1995; Freedman & Sparks, 1997).

Smooth pursuit

The eye can track moving visual targets by rotating the eye with a regulated velocity that fits the velocity of the target, also known as smooth pursuit. While saccades minimizes errors by correcting the *position* error (retinal error) by another saccade smooth pursuit eye movements are continuously correcting the

velocity error, called the retinal slip, by increasing or decreasing the velocity in a closed loop control system with visual feedback. Initially the mechanism nevertheless works as an open loop system since there is a certain latency of about 100 ms (Rashbass, 1961; Robinson, 1965; Krauzlis & Lisberger, 1994) and during the closed loop state small saccades are seen more or less regularly (Collewijn & Tamminga, 1984).

Smooth pursuit eye movements when the head is free to move is the subject of Chapter 3 and will be discussed there.

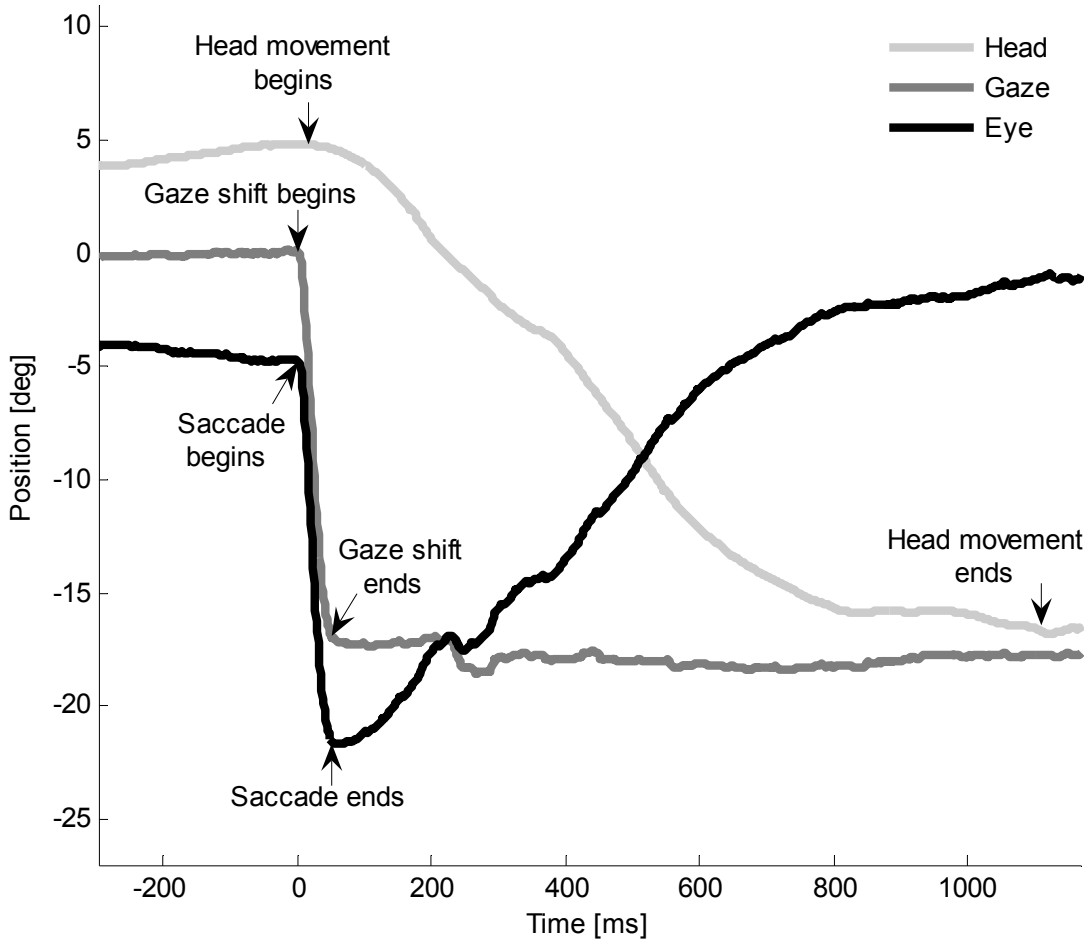

Figure 1-7. Typical gaze saccade in the horizontal plane with the head unrestrained.

The gaze (dark gray) shifts from the straight ahead to 18° left. Almost the entire shift is performed by the eye (black) while the head almost only turns after the gaze shift has ended. This relationship changes for larger gaze shifts. Data from subject M3 (see also e.g. Fig. 4 in Freedman, 2008)

1.4 Rotation representation and reference frames

When measuring the orientation of the eye or head in three dimensions it is important to first define the rotation representation along with the reference frame. Generally, the rotation of a solid object (rigid body) in three dimensions is defined as a movement where the distance from a fixed axis to any given point of the object remains constant. The representation of a given rotation is made by describing the final orientation relative to a reference frame, where the reference frame is an ordinary Cartesian coordinate system.

Several different ways to represent rotation have been used in the eye movement literature and the five most common will be briefly reviewed here (for more see e.g. Haustein, 1989; Hepp, 1990; Tweed, Cadera & Vilis, 1990; Haslwanter, 1995). As discussed later in section 1.6 and 2.3.2, eye and head position data are obtained as rotation matrices. However, for the purpose of visualizing and computation of data the rotation vector is superior. Hence, all data in this thesis are shown in rotation vectors relative to a right-handed coordinate system where the x-axis is pointing forward, the y-axis is pointing leftwards and the z-axis is pointing upwards.

1.4.1 The rotation matrix

The rotation matrix describes the position of three orthogonal unit vectors $\vec{u}$, $\vec{v}$ and $\vec{w}$ relative to the reference frame. The three vectors are fixed to the object (eye or head) and align with the reference coordinate system when the object is in reference position. In fact, the nine components in the matrix describe the basis of a new coordinate system relative to the reference coordinate system. The matrix consists of three rows and three columns where each column describes each of the three orthogonal vectors:

$$R = \begin{bmatrix} u_1 & v_1 & w_1 \\ u_2 & v_2 & w_2 \\ u_3 & v_3 & w_3 \end{bmatrix} \tag{1-3}$$

In the reference orientation the orthogonal unit vectors $\vec{u}$, $\vec{v}$, and $\vec{w}$ are pointing forwards, leftwards and upwards, respectively. From this it is clear that a rotation purely around the vertical axis (z-axis) will give:

$$R_{hor}(\theta) = \begin{bmatrix} \cos(\theta) & -\sin(\theta) & 0 \\ \sin(\theta) & \cos(\theta) & 0 \\ 0 & 0 & 1 \end{bmatrix} \tag{1-4}$$

This is called a horizontal rotation and will be denoted by theta (θ).

A rotation purely around the leftward pointing axis (y-axis) will give the rotation matrix:

$$R_{ver}(\phi) = \begin{bmatrix} \cos(\phi) & 0 & \sin(\phi) \\ 0 & 1 & 0 \\ -\sin(\phi) & 0 & \cos(\phi) \end{bmatrix} \tag{1-5}$$

This is called a vertical rotation and will be denoted by phi (φ).

A rotation purely around the forward pointing axis (x-axis) will give the rotation matrix:

$$R_{tor}(\psi) = \begin{bmatrix} 1 & 0 & 0 \\ 0 & \cos(\psi) & -\sin(\psi) \\ 0 & \sin(\psi) & \cos(\psi) \end{bmatrix} \tag{1-6}$$

This is called torsional rotation and will be denoted by psi (ψ).

But what is the rotation matrix if multiple rotations are combined? To answer this it is important to recognize that rotations in three dimensions are non-commutative. Thus, the sequence of the rotations matters. Figure 1-8A shows a

horizontal rotation, $R_{hor}(\pi/2)$, followed by a vertical rotation, $R_{ver}(\pi/2)$. When the sequence is inversed, as shown in Figure 1-8B, it is seen that the final orientation is different. Note that these are fixed axis rotations (active rotations), which means that the rotations are performed relative to the space fixed reference frame. The final orientation can be calculated by matrix multiplication as seen in Equation (1-7).

$$R_{final} = R_2 R_1 \tag{1-7}$$

where R_1 is the first rotation and R_2 is the second.

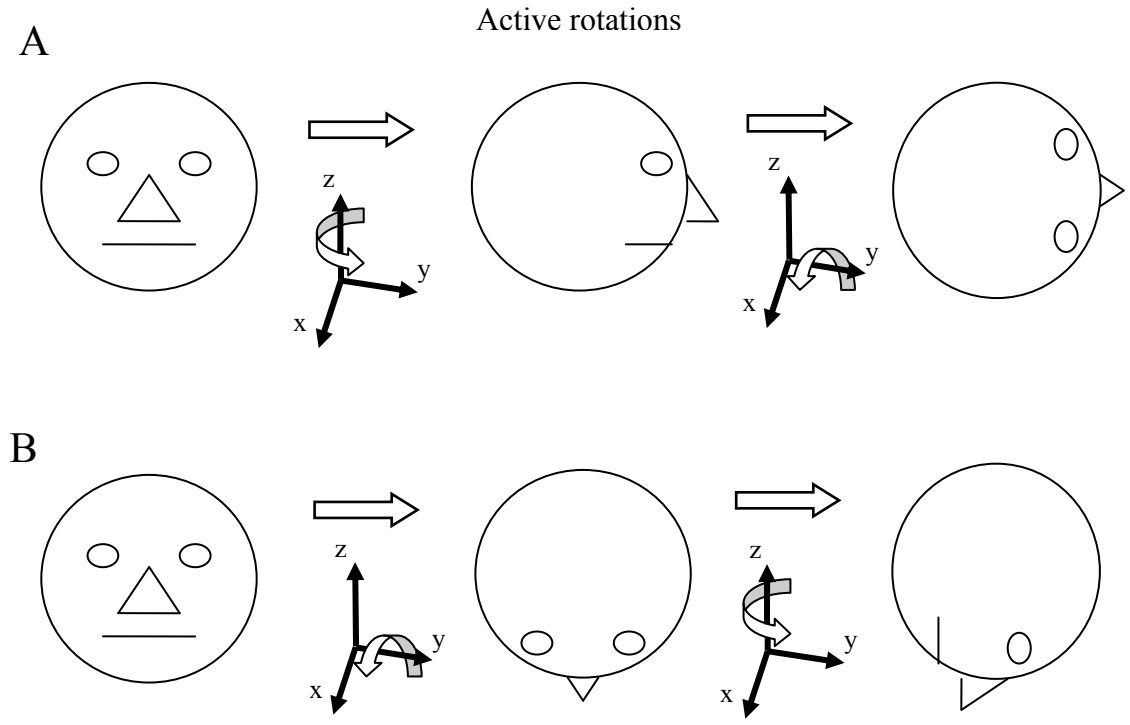

Figure 1-8. Fixed axis rotations (active rotations).

Single z- and y-axis rotations in different sequences give different results. *A*: z- then y-axis rotation. *B*: y- then z-axis rotation.

1.4.2 Fick- and Helmholtz angles

As opposed to the fixed axis rotations (also called active rotations) shown above, rotations can also be described relative to the moving object (also called passive rotations). This means that the coordinate system will move with the object and thus the axes of rotation will depend on the subsequent rotations. In other words, the first rotation will be made like an active rotation since the coordinate systems are initially aligned. But hereafter the rotations will now rotate relative to the current orientation of the object (see Figure 1-9A). As active rotations, passive rotations are non-commutative, so it is necessary to define the sequence of rotations. Two common sequence definitions are the Fick- and Helmholtz sequences. Figure 1-9A shows the Fick sequence: first horizontal, then vertical, then torsional, which is also called yaw, pitch and roll respectively. Figure 1-9B shows the Helmholtz sequence: first pitch, then yaw, then roll. In black is shown the fixed coordinate system while the gray depicts the moving coordinate system.

Rotation matrix representation can be obtained from Fick angles by:

$$R_{Fick} = R_{hor}(\theta)R_{ver}(\phi)R_{tor}(\psi) \tag{1-8}$$

Similarly the Rotation matrix for Helmholtz angles can be obtained by:

$$R_{Helmholz} = R_{ver}(\phi)R_{hor}(\theta)R_{tor}(\psi) \tag{1-9}$$

For both equations θ, φ and ψ are Yaw, Pitch and Roll respectively. Notice that for passive rotations the order of multiplication is reversed (compare with Eq. (1-7)). Also note that once a rotation matrix of the final orientation is obtained it describes the whole rotation unambiguously and any preceding sequence of rotations needs not to be defined.
Fick angles can be obtained from a rotation matrix by:

$$\begin{aligned}\theta_{Fick} &= \text{atan2}(R_{21}, R_{11}) \\ \varphi_{Fick} &= \text{atan2}(-R_{31}, \sqrt{R_{11}{}^2 + R_{21}{}^2}) \\ \psi_{Fick} &= \text{atan2}(R_{32}, R_{33})\end{aligned} \tag{1-10}$$

And Helmholtz angles are similarly given by:

$$\begin{aligned}\varphi_{Helm} &= \text{atan2}(R_{31}, R_{11}) \\ \theta_{Helm} &= \text{atan2}(R_{21}, \sqrt{R_{31}{}^2 + R_{11}{}^2}) \\ \psi_{Helm} &= \text{atan2}(R_{23}, R_{22})\end{aligned} \tag{1-11}$$

Where atan2 is the two-argument variation of the inverse tangent function and R_{ik} is defined as the matrix element in row "i" and column "k". These equations are made by solving eq. (1-8) and (1-9) symbolically and extracting the Fick- and Helmholtz angles. This is shown in Appendix D.

One important feature of passive rotations is that they can be used to describe gimbaled rotations. That is rotations around nested axes such as the ones made by the 3D turn chair used in experiments in this thesis.

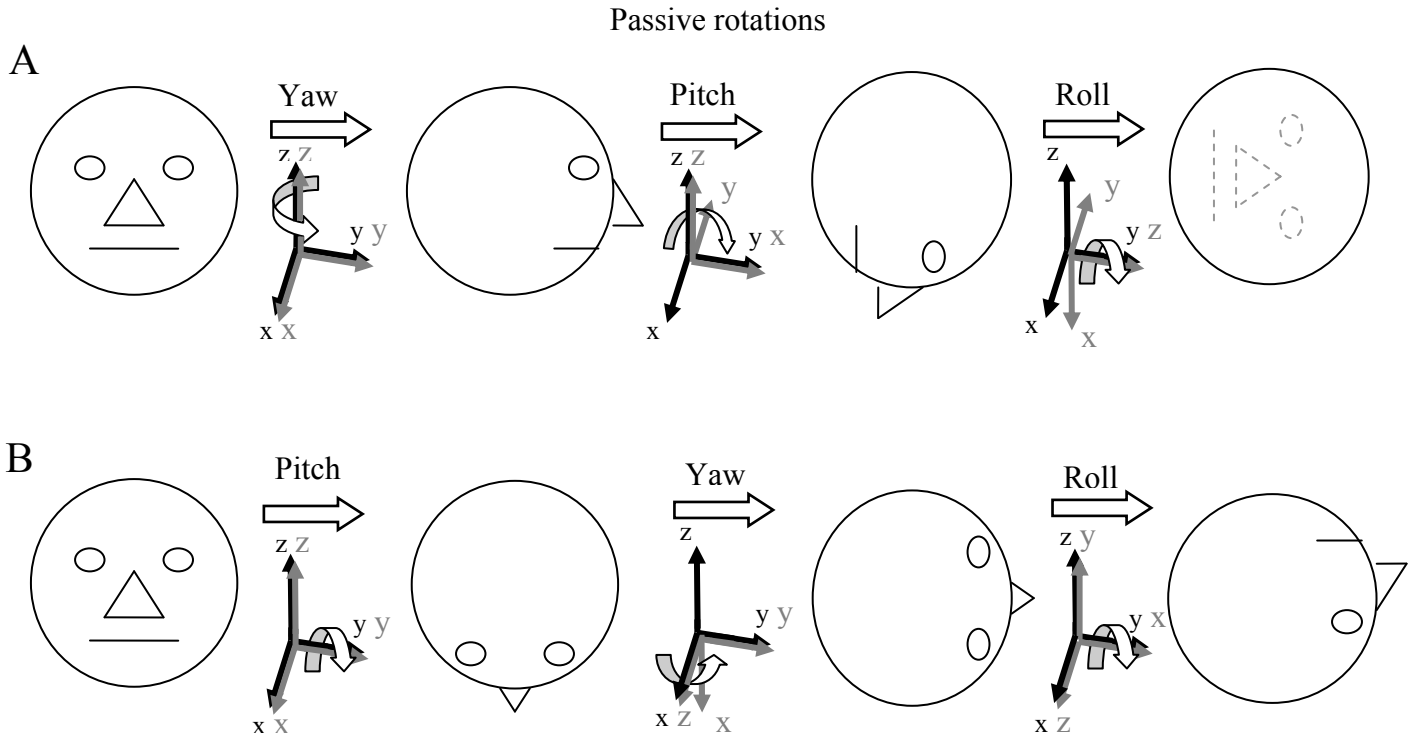

Figure 1-9. Ninety degree gimbaled rotations (passive rotations).

Sequence of Fick (*A*) and Helmholtz (*B*) rotations. Black arrows show the fixed coordinate system and gray arrows the moving coordinate system. The dashed lines in the last orientation in (*A*) indicate that the head is seen from behind.

1.4.3 Quaternions and rotation vectors

Euler's rotation theorem says that any orientation in 3D can be reached from another orientation with one single rotation around a fixed axis. A graceful way to describe this fact is by using the quaternion first developed by Hamilton (1899). A quaternion can be seen as having two parts: a vector component and a scalar component.

$$q = q_0 + \vec{q} \tag{1-12}$$

The vector $\vec{q}$ is parallel to the axis of rotation and points in the direction according to the right-hand rule. This means that when the thumb of the right hand is pointing in the direction of the vector, the fingers will curl in the direction of the rotation. The relationship between the magnitude of the vector and the magnitude of the rotation is $|\vec{q}| = \sin(\theta/2)$, where θ is the angle rotated. The scalar part equals $q_0 = \cos(\theta/2)$.

Another way to describe rotations around a single fixed axis is the rotation vector. The rotation vector is related to the quaternion but instead of a quadruple consisting of a scalar and a three component vector part, the rotation vector only consists of the vector scaled by the scalar part i.e. $\vec{r} = \vec{q}/q_0$. Thus the rotation vector only has three components versus the four components of the quaternion. The magnitude of the rotation vector is $|\vec{r}| = \tan(\theta/2)$. When visualizing rotation vector data it can be useful to adjust the magnitude of the rotation vector to equal the rotation in degrees. This modified vector will be called the "orientation vector" and is defined by: $\vec{o} = \arctan(\vec{r}) \cdot 360/\pi$ so that $|\vec{o}| = \theta$.

To combine two rotations, for example first the rotation of the head relative to space (Head) and then the eye relative to the head (Eye) to give the orientation of the eye relative to space (Gaze) the following equation can be used (Haustein, 1989):

$$\vec{r}_{Gaze} = \vec{r}_{Head} \circ \vec{r}_{Eye} = \frac{\vec{r}_{Eye} + \vec{r}_{Head} - \vec{r}_{Eye} \times \vec{r}_{Head}}{1 - \vec{r}_{Eye} \bullet \vec{r}_{Head}} \tag{1-13}$$

Several considerations must be taken into account when considering which rotation representation to use. As will become clear later the rotation matrix is directly obtained from the measurement of the eye position. However, this representation is difficult to interpret and visualize. Furthermore, it contains nine elements yet only three are adequate to describe the three dimensions and therefore it is inefficient for storing of large data sets.

The Fick and Helmholtz angles offer better readability than the rotation matrix and contain only three elements. Nevertheless, the axes are arbitrary and need to be defined *a priori* along with the sequence of rotations. The fact that the axes are nested and therefore dependent on each other may also be a disadvantage when analyzing data. However, for specific purposes for example when analyzing head movements the Fick angles can be advantageous while Helmholtz angles have advantages when analyzing converged eye movements.

The rotation vector only contains the minimum of three elements like the Fick and Helmholtz angles. However, it does not depend on sequential rotations around arbitrary axes. It can be argued that because the extraocular muscles are fixed in and pull from the head, a fixed axis rotation representation appears more suitable (also called head-fixed coordinates). Furthermore, it simplifies calculations and all axes are treated equally which makes it optimal for some analysis. For example, as we shall see in the next section, to verify if eye movements obeys Listing's law rotation vectors are very suitable.

1.5 Donders' law, Listing's law and the half angle rule

The six extraocular muscles control the eye in all three dimensions of rotation. While all rotational degrees of freedom are utilized under various conditions, there are situations where the rotational degree of freedom is in fact only two-dimensional. This means that wherever the eye moves in the horizontal-vertical plane the orientation the eye changes as a fixed function of gaze position. In other words, for any direction of the line of sight the *cyclotorsion* (the rotation of the eye around the gaze line) that the eyes assumes is independent of how the eye rotates to reach that particular gaze direction. This restraint is called Donders' law (Donders, 1848). If eye (or head) movements that obey Donders' law are described by rotation vectors the end-points of the vectors will form a surface. Johann Listing defined this surface for eye fixations and found that they lie, for far viewing, in a plane provided that the head is upright and stationary (von Helmholtz, 1867). This also means that there exists an orientation of the eye (called primary position) for which the line of sight is perpendicular to the rotation axes of all other orientations. This more strict restraint is called Listing's law and the plane formed is called Listing's plane.
Figure 1-10 shows orientation vectors for macaque eye positions forming such a plane seen from the behind (A), right (B) and above (C) relative to the subject.

It has been shown that Listing's law is obeyed in far viewing for both saccades, fixations (Ferman, Collewijn & van den Berg, 1987; Tweed & Vilis, 1990; Minken, Van Opstal & van Gisbergen, 1993) and smooth pursuit eye movements (Haslwanter, Straumann, Hepp, Hess & Henn, 1991; Tweed, Fetter, Andreadaki, Koenig & Dichgans, 1992) provided that the head does not move. When the eyes are observing the far distance the Listing's planes of the two eyes are parallel but when the eyes converge to observe objects in the near the planes will tilt outwards (Mok, Ro, Cadera, Crawford & Vilis, 1992; Schor, Maxwell & Graf,

2001; Cabungcal, Misslisch, Hepp & Hess, 2002). Notice that outward tilting planes mean that the eyes will produce extorsion when looking down and intorsion when looking up. This is also called the binocular extension to Listing's law or simply L2 (Tweed, 1997). Measurements of the tilt angle have differed but around ¼ of the vergence angle is considered to be the theoretical ideal since this ratio keeps the retinas aligned (Van Rijn & Van den Berg, 1993). When the head is tilted statically eye movements also obey Listing's law although the plane shifts due to counter-roll of the eyes (Haslwanter, Straumann, Hess & Henn, 1992; Hess & Angelaki, 2003).

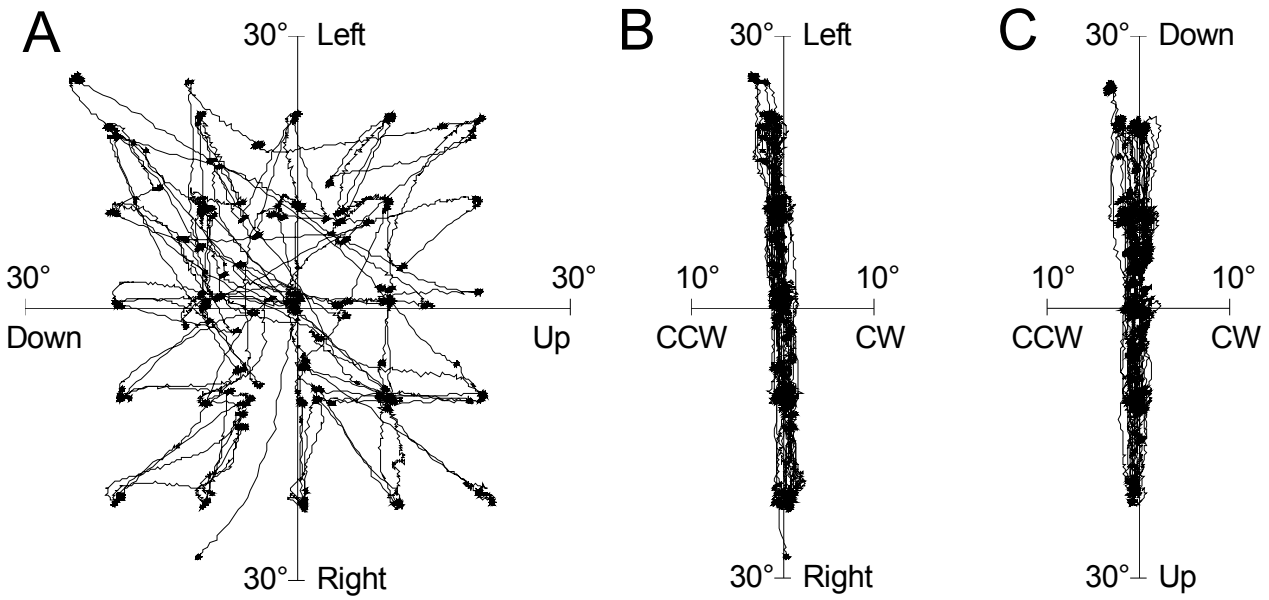

Figure 1-10. Listings plane from orientation vector end-points.

Fixations and saccades made by subject M1. *A*: Behind-view. *B*: Side-view (from right). *C*: Top-view. (see e.g. Fig. 2 in Angelaki & Hess, 2004)

Note that Listing's plane consists of the end-points of the rotation vectors that are required for moving the eye from the primary position to any other position. This means that the rotation vector moving the eye from primary position to, say, 10 degrees up and 10 degrees left (position A) lies in Listing's plane and the rotation

vector moving the eye from primary position to 10 degrees up and 10 degrees right (position B) lies in Listing's plane. But what about the rotation vector that moves the eye from A to B? Since, as described earlier rotations in three dimensions are non-commutative, this vector cannot lie in Listing's plane too. This is also the reason why it is not possible to calculate the angular velocity by simply taking the derivative of the rotation vector. The angular velocity also depends on the instantaneous orientation. From Eq. (1-13) it can be shown that the angular velocity vector is equal to (Hepp, 1990):

$$\vec{\omega} = \frac{2(\dot{\vec{r}} + \vec{r} \times \dot{\vec{r}})}{1 + |\vec{r}|^2} \tag{1-14}$$

Where $\dot{\vec{r}}$ is the derivative of $\vec{r}$.

This angular velocity vector can be shown to tilt in the torsional direction with exactly half the angle of the present eye position relative to primary position (Figure 1-11). This is also called the half angle rule and provides an alternative characterization of Listing's law. Only because of the half angle rule will the eye orientation during saccades and smooth pursuit lie in Listing's plane.

This geometrical fact is also of high physiological interest since the velocity axis defines the axis which the motor system must produce to move the eye. But, is it defined by the efferent signal from the brain (neural) or by the structure of the muscles and ligaments of the oculomotor plant (mechanical)? Does the oculomotor plant obey Listing's law or follow a VOR strategy when supplied with only horizontal and vertical commands? Although the oculomotor system is one of the most studied motor systems some of these fundamental questions have not been fully answered and are still topics of research. Demer and co-workers (1995) have found structures in the ocular orbit, called pulleys, that surround the tendons of the rectus muscles and thus can change their pulling direction in a way that favors a mechanical implementation of Listing's law (see Figure 1-12). Subsequent studies about their role have lead to speculations, although the

general consensus points towards that they help keeping the eye in Listing's plane. Nevertheless have neurons in the brainstem been shown to code for the half angle rule during smooth pursuit suggesting a neural implementation (Angelaki & Dickman, 2003), while single unit recordings from motoneurons of the eye muscles have suggested a mechanical implementation (Ghasia & Angelaki, 2005).

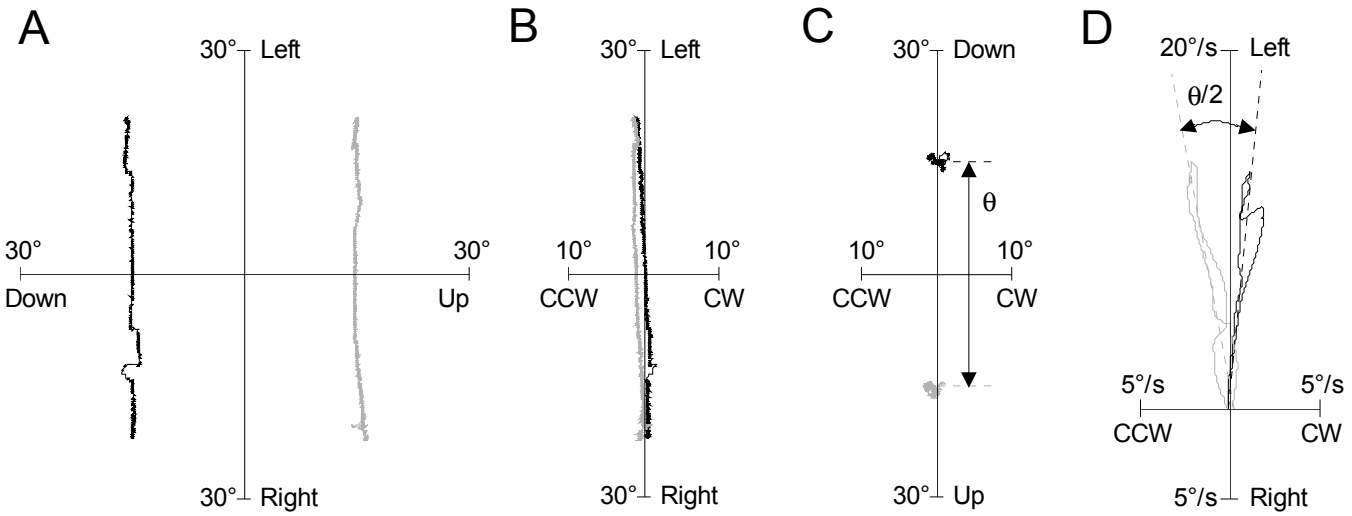

Figure 1-11. The half angle rule shown by two traces of smooth pursuit.

Different elevations: 15º in black and –15º in gray. *A*: Behind-view of end-points of orientation vectors. *B*: Side-view from right. *C*: Top-view. Inserted: the mean angle between the two traces (θ = 30º). *D*: Velocity vectors of the two traces. Inserted: the angle between the least-squares fit (15 º). Data from subject M1 (see also Tweed & Vilis, 1990).

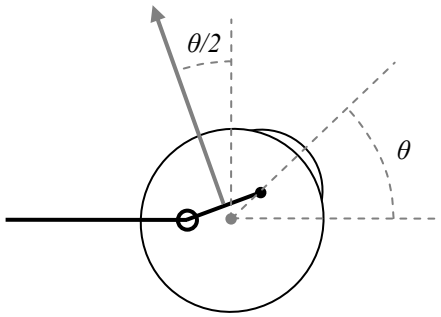

Figure 1-12. Mechanical implementation of Listing's law.

A pulley (small ring) holds the rectus muscle (black line) at the same distance behind the center of rotation (gray dot) as the muscle insertion (black dot) is in front of the center of rotation so that the effective pulling direction will tilt the axis of rotation (gray arrow) by half of the angle of the gaze-line θ.

1.6 The scleral search coil technique

When Helmholtz measured eye movements in the 19th century he used visual after-images made with a ribbon in contrast with a background with horizontal lines. This way the cyclotorsion could be estimated for different positions of gaze. The technique, which depends on the subjective estimate from the tested subject, was invented about a century earlier by Wells (1792) and rediscovered again by Ruete (1845) (see e.g. Wade (2007) for a historical review). Later in the 19th century and in the early 20th century different objective eye tracking methods were developed. One used a lever attached to the eye which could directly draw the traces of one dimensional movement, while others used photographic equipment to record the eye movements (Delabarre, 1898; Huey, 1898; Huey, 1900; Dodge & Cline, 1901). However, a precise and accurate method was not available until Robinson (1963) invented the scleral search coil. The method has since been improved and expanded to record in three dimensions (Humans: Collewijn, van der Steen, Ferman & Jansen, 1985; Animals: Hess, 1990) but the basic principle is still the same: a coil of wire attached to the eye will induce a current relative to the angular position of the eye when the subject is sitting inside an alternating homogeneous magnetic field. Although video-based eye recording systems have gained popularity in recent years, the scleral search coil method is today still the gold standard of measuring three-dimensional eye movements and the preferred method for many researchers due to its high spatial and temporal resolution.

Figure 1-13A shows a sketch of a coil (in side-view) inserted in a homogeneous alternating magnetic field. From Faraday's law we know that the electromotive force (emf), which is proportional to the inducted current, will be equal to the change in magnetic flux through the coil's surface times the number of turns of wire in the coil. The magnetic flux is defined as the scalar product of magnetic field and the area element vector. If the alternating magnetic field is homogeneous and the number of turns in the coil and the area spanned by the coil

is kept constant, the only variable will be the orientation of the area element vector, which is also the direction of the coil.

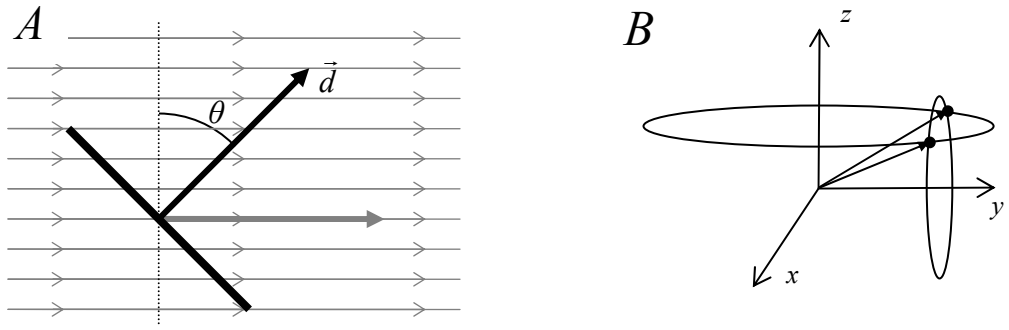

Figure 1-13. Search coil in a magnetic field.

If a search coil is inserted in an alternating magnetic field the coil will induce a current defined by Faraday's law. However, calculation of absolute values is not necessary for determining the angle relative to the magnetic field if a calibration is made. *A*: A single magnetic field will define an angle θ of the coil vector $\vec{d}$ relative to the field direction (here defined from the perpendicular of the field direction). This restricts the possible positions of the vector-tip to lie on a ring. *B*: For two perpendicular magnetic fields (in y- and z-directions) the angles defined relative to the fields will restrict the location to be at one of the two intersections of the two rings.

However, to find this direction it is not necessary to know the absolute values of all the components involved. We can define a vector, called the coil vector (also called the sensitivity vector and denoted by $\vec{d}$) which is parallel to the area element vector and perpendicular to the surface of the coil. If we define the magnitude of this vector to be equal to the maximally inducible current (when the coil is directed with the area element vector parallel to the magnetic field), then this vector will contain the constant parameters. The magnitude of such a vector can then easily be defined by a calibration, for example by placing the coil directly into the magnetic field and measuring the output. Any given direction of the vector, hence the coil, will then have the output $d_{out} = \left|\vec{d}\right| \sin(\theta)$ where θ is the angle of the coil vector from perpendicular to the magnetic field (see Figure

1-13A). Thus the angle can be calculated as $\theta = \arcsin(d_{out} / |\vec{d}|)$. But in three dimensions this information will only allow us to define the vector–tip to be somewhere on a circle (see Figure 1-13B). If we add a second magnetic field, perpendicular to the first and separable with either a 90° phase shift or with a different frequency from the first magnetic field, we can limit the possible locations to two positions, namely the intersections of two circles (mirrored by the plane spanned by the magnetic fields). For measuring eye movements in head-restrained subjects this causes no practical problem if the coil is placed with the coil vector near the line of sight and the plane spanned by the magnetic fields is aligned with the coronal plane of the subject since the limitation of the oculomotor range will easily define which of the two possible orientations is correct. If a third magnetic field is added, orthogonal to the other two and separated in frequency, the vector is given by the three outputs explicitly and no calibration is necessary provided that the three magnetic fields are equally strong. This can however be difficult to achieve perfectly and offset currents are usually present so a calibration is most often necessary also for systems with three magnetic fields.

Knowing the position of the coil vector of a search coil only defines the orientation in two dimensions. Rotations around the axis of the coil vector are undisclosed. This means that if only one search coil is attached to the eye and that coil has a coil vector aligned with the gaze (direction coil), rotations around the line of sight will be undetected. To measure three dimensional eye movements we must add a second search coil which is not parallel to the direction coil. For highest sensitivity this coil (called torsion coil) should be near perpendicular to the direction coil.

This coil will however, as opposed to the direction coil, have potential to have its coil vector on both sides of the plane spanned by the y- and z-axis (the subjects coronal plane) during normal eye movements. The coil vector can therefore not by itself be measured explicitly in only two magnetic fields. I.e. of the two

possible positions (Figure 1-13B), it will not be possible to say which one is correct. This can nevertheless be predicted if the angle between the two search coils is known *a priori*, hence by calibration. A detailed explanation of the procedure can be found in Hess, Van Opstal, Straumann & Hepp (1992).

A set of both direction and torsion coils can be imbedded in one unit, called a dual search coil (Figure 1-14). In rhesus monkeys the dual search coil is sutured to the sclera under the bulbar conjunctiva and the lead wires are led posterior into the subconjunctival space where a small loop of wire is left for the eye to be able to rotate freely (Fuchs & Robinson, 1966; Judge, Richmond & Chu, 1980; Hess, 1990). The wires are then exiting the orbit over the zygomatic process of the temporal bone and led subcutaneously to a connector plug on the skull.

Figure 1-14. A dual search coil.

The dual search coil consists of a large coil, called direction coil, with only three turns and two small serially connected miniature coils with about 150 turns each. The two miniature coils, called torsion coils, are firmly fixed approximately diametrically opposed on the periphery of the direction coil with their coil vectors aligned about 90° from the coil vector of the direction coil. The two twisted wire-pairs from the direction coil and the torsion coils leave the dual search coil on diametrically opposed sides. Described in detail in Hess (1990).

2. Decoding 3D search coil signals in a non-homogeneous magnetic field*

2.1 Abstract

We present a method for recording eye–head movements with the magnetic search coil technique in a small external magnetic field. Since magnetic fields are typically non-linear, except in a relative small region in the center small field frames have not been used for head-unrestrained experiments in oculomotor studies.

Here we present a method for recording 3D eye movements by accounting for the magnetic non-linearities using the Biot-Savart law. We show that the recording errors can be significantly reduced by monitoring current head position and thereby taking the location of the eye in the external magnetic field into account.

* This chapter has been published as: Thomassen J.S., Benedetto G.D. & Hess B.J. (2010). *Vision Res.*, 80 (13), 1203-1213.

2.2 Introduction

In vestibulo-oculomotor studies, rotating or translating devices are often used to stimulate the vestibular sensory organs of the inner ear while monitoring the eye movements. The preferred method for monitoring eye movements is the magnetic search coil technique, which is well established in humans, in non-human primates and other animals (Robinson, 1963; Fuchs & Robinson, 1966; Judge et al., 1980; Collewijn et al., 1985; Hess, 1990). In recent years eye movement recording techniques based on video have gained popularity due to their lesser invasiveness (Imai, et al., 2005; Houben, Goumans & van der Steen, 2006). However, the search coil technique still remains the method of choice for many researchers, due to important advantages such as high spatial and temporal resolution, signal-to-noise ratio, stability, reproducibility and minimal sensitivity to blinking and pupil stability. The search coil technique offers particular and hitherto unmatched advantages in studies of three dimensional (3D) eye movements with or without the head moving.

When using the search coil technique in 3D eye movement studies, a dual search coil consisting of two, roughly, perpendicular coils in a single rigid construction (Collewijn et al., 1985; Hess, 1990) or simply a pair of independent coils (Tweed et al., 1990) are used as sensors. In this study we deal solely with the rigid dual search coil, although the method applies in principle also for two independent coils. With the search coil firmly fixed to the eye, the subject is sitting inside a magnetic field that consists of two or three alternating magnetic fields (primary fields) generated by orthogonally arranged external field coils (frame coils). The primary fields induce currents in the two search coils depending on their orientation relative to the primary fields. From these currents the 3D orientation of the search coils (and thus the eye's orientation) can be determined. Since reliable measurements can only be obtained within the region, where the fields are homogeneous and mutually orthogonal, subjects are typically placed with the

head fixed in the center. When measuring eye–head movements, large rectangular frame coils (e.g. 2 × 2 × 2 m) are typically used such that the subject can move its head without leaving the homogeneous part of the field (see e.g. Tweed et al., 1995).

To minimize distortions of the primary field, e.g. by the metallic parts in the vicinity, the frame needs to be placed around the head of the subject within a motion device. This imposes considerable restrictions on the size of the frame coils such that eye movements are often not reliably recorded when the subject's head is free to move. Certain geometric frame configurations like the Helmholtz configuration or other configurations with a larger number of frame coils (Rubens, 1945; Collewijn, 1977; Ditterich & Eggert, 2001) provide better linearity than a simple cubic frame, yet at the cost of reducing the subject's field of view. Visuo-vestibular studies typically require the fixation of point targets in far-viewing as visual stimulus and a smaller field of view than the approximate 90° provided by the cube configuration would cause a significant restriction during combined eye–head movement studies.

Here, we present a method for measuring eye movements with the search coil method by taking the non-linear spatial field characteristics into account using the Biot-Savart law. The recording technique was evaluated in two steps: (1) a simulation of eye movements made by an 'artificial eye' which was positioned in various orientations at different locations in the magnetic field and (2) an *in vivo* experiment, where rhesus monkeys were trained to fixate targets with their heads unrestrained. The head movements were measured with an ultrasonic system to locate the spatial eye position in the primary field.

2.3 Materials and methods

2.3.1 General experimental setup

For practical purposes, we used two different setups for these experiments. The simulation experiment, which required the manipulation of a three-axis gimbal protractor at different locations, was performed in a large magnetic field frame with side length of 75 cm (Angle-Meter NT, Primelec, Regensdorf, Switzerland). The *in vivo* experiment was done in a similar but much smaller system with side length of approximately 30 cm (Eye Position Meter 3000, Skalar Instruments, Delft, The Netherlands), fitted inside the inner frame of a motorized four-axis gimbaled motion device (Acutrol, Acutronic Schweiz AG, Bubikon, Switzerland). Although the Primelec system is a three-field system generating three primary magnetic fields in contrast to the Skalar system, we used only the output signals of two primary magnetic fields in both sets of experiments (for a three-field approach see Appendix A). One of these fields was directed vertically along the subject's rostro–caudal axis and the other was directed horizontally along the interaural axis of the subject. Physically, each field resulted in fact from superimposing the magnetic fields produced by two parallel-arranged square shaped coils at each side of the frame (Figure 2-1). The two coil pairs generated two homogeneous magnetic fields in the center of the frame that were in space quadrature. The Primelec system used frequency encoding to enable separate detection of the fields whereas the Skalar system used phase encoding.

In both sets of experiments, we used the same type of (implantable) dual search coil (Hess, 1990). In brief, the dual search coils consisted of one three-turn wire coil with a diameter of ca. 15 mm (direction coil) and two serially connected oval-shaped miniature wire coils of ca. 1.5 × 2.2 mm diameters and 150 turns each (torsion coil). The torsion coils were rigidly mounted at diametrically opposed positions on the circumference of the direction coil such that the direction of maximal sensitivity was roughly at 90° with respect to the sensitivity direction of the direction coil. The dual search coil was finally sealed with an

electrically insulating Araldite (XD4510, Astorit, Switzerland) and surface coated with a bio-compatible plastic compound (Rilsan PA11, Arkema, France).

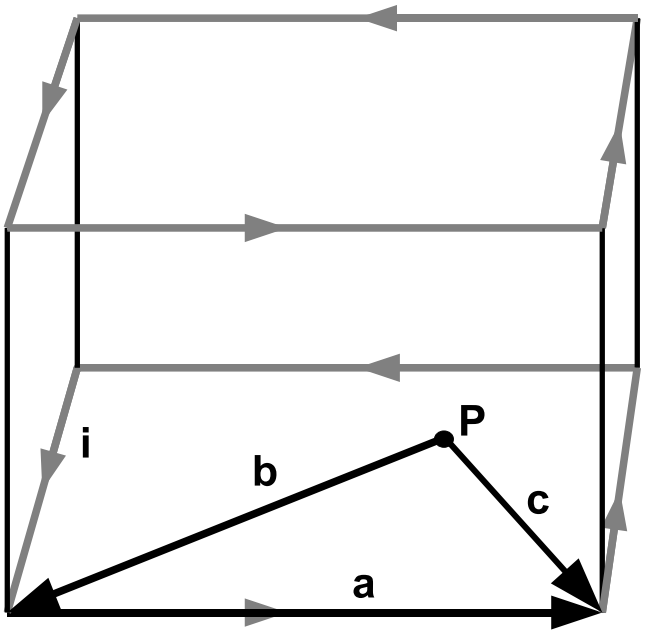

Figure 2-1. Magnetic field frame

The magnetic field Htotal at point P is calculated by superposition of the eight sticks of the two primary coils. It is mainly directed in the vertical direction. The similar calculations are made for the other primary magnetic field which is mainly directed horizontally.

All search coil induction data were digitized at 833.33 Hz with a resolution of 12-bit. The data were analyzed offline using MATLAB (The Mathworks Inc., Natrick, MA, USA) and 3D eye orientations were expressed as rotation vectors in space-fixed *x*- (orthogonal to the *y*- and *z*-coordinates), *y*- (interaural axis), and *z*-coordinates (head vertical axis). The eye's orientation while looking straight-ahead was taken as reference position (Haustein, 1989; Hess et al., 1992).

2.3.2 Search coil signal demodulation using the Biot-Savart law

We used the Biot-Savart law to compute the direction and relative strength of the magnetic field at the position of the search coil (the eye). The rectangular frame coils consisting of straight aluminum bars were approximated by sticks of zero thickness. With this simplification the integration in the Biot-Savart law can be circumvented by using the more computer efficient vector calculations (Haus & Melcher, 1989).

$$H = \frac{i}{4\pi} \frac{c \times a}{|c \times a|^2} \left(\frac{a \bullet c}{|c|} - \frac{a \bullet b}{|b|} \right) \tag{2-1}$$

This equation describes the magnetic field vector "*H*" resulting from one of the eight sticks of the frame coils. Each stick is described by a vector, say "*a*" with base at one end of the stick and endpoint at the other end, pointing in the direction of the current flow, denoted by "*i*" (Figure 2-1). To compute the magnetic field vector "*H*" at point *P* of the current "*i*" in stick "*a*", the equation further requires the vector "*b*" with base at point *P* and endpoint at the base of "*a*" and the vector "*c*" with base at *P* and endpoint at the endpoint of vector "*a*". The resulting magnetic field H_{total} can then be determined by the superposition principle of the eight sticks (or bars) in the frame for each of the coil pairs that generate a primary field. An estimation of the amount of current flow "*i*" is not important because the calculated field does not need to be in absolute values. The field should simply be calculated relative to the center of the frame coils i.e. no correction is made in the center. Appendix E shows the implementation in Matlab of both the absolute (Appendix E.1) and the relative (Appendix E.2) calculation for an array of data.

The following describes how to demodulate the search coil signals using only two primary fields (*Y* and *Z*). The procedure for three primary fields (*X*, *Y* and *Z*) is shown in Appendix A.

We used a right-handed orthogonal coordinate system with positive *x*-direction pointing straight forward (parallel to the naso-occipital axis of the tested subject), positive *y*-direction pointing leftward (parallel to the subject's interaural axis) and the *z*-direction pointing upward (parallel to the subject's rostro-caudal axis). As seen from the subject, positive rotations about the *x*-, *y*- and *z*-axis are clockwise, downward and leftward.

To describe the geometry of the magnetic flow field, we denote the magnetic field vector of the primary *Y*-field at point *P* by $\vec{v}(P)$. It associates with each point *P* inside the frame coils a vector according to the relation (superscript "*T*" stands for transpose):

$$\vec{v}(P) = [v_1, v_2, v_3]^T \tag{2-2}$$

Similarly, we denote the magnetic field vectors of the primary *Z*-field at the point *P* by:

$$\vec{w}(P) = [w_1, w_2, w_3]^T \tag{2-3}$$

Consider now a search coil, which we will call *direction coil* due to its close alignment with the direction of the line of sight, with the sensitivity vector $\vec{d} = [d_1, d_2, d_3]^T$ (orthogonal to the plane spanned by the search coil) at position *P* in the external field (Figure 2-2). The sensitivity vector carries information about the magnitude of the induced currents measured in the center of the external field (i.e. calibration at point $P = 0$) and the present direction of the coil. The induced output signals, d_v and d_w, at any position $P=[x_P,y_P,z_P]$ in the external field can be obtained by taking the dot products of the sensitivity vector and the respective magnetic fields $\vec{v}(P)$ and $\vec{w}(P)$:

$$d_v(P,E) = \vec{d}(E) \bullet \vec{v}(P) = d_1 \cdot v_1 + d_2 \cdot v_2 + d_3 \cdot v_3 \tag{2-4}$$

$$d_w(P,E) = \vec{d}(E) \bullet \vec{w}(P) = d_1 \cdot w_1 + d_2 \cdot w_2 + d_3 \cdot w_3 \tag{2-5}$$

Note that field vectors $\vec{v}(P)$ and $\vec{w}(P)$ are normalized by the magnitudes calculated at the center of the frame coils ($P = 0$). The dummy variable "E" refers to the fact that these signals depend on eye orientation when the coil is fixed to the eye.

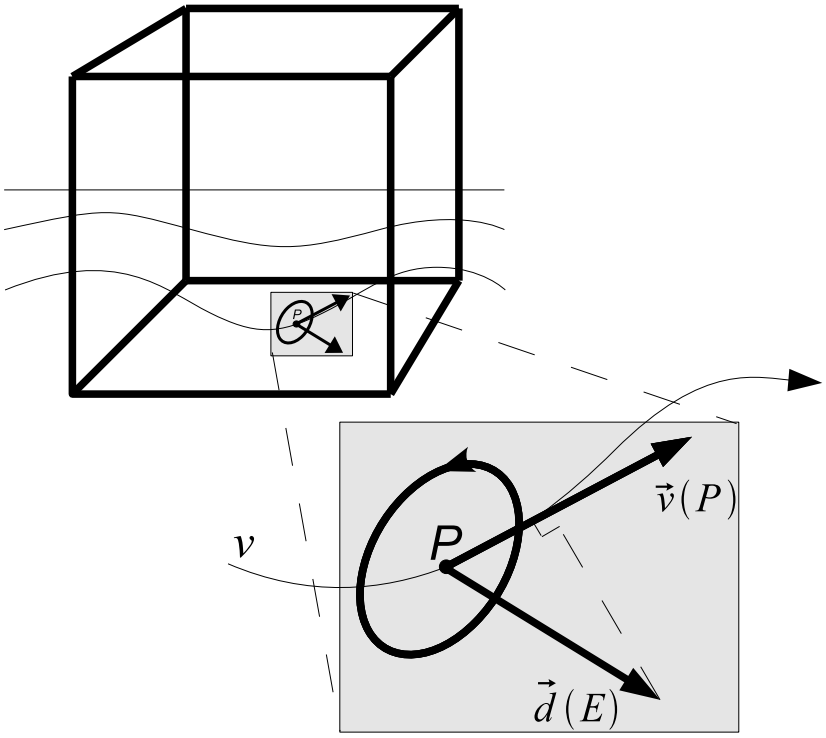

Figure 2-2. Search coil in non-linear magnetic field

A magnetic search coil inserted at point P in the alternating magnetic field "v" will pick up an alternating current. The induced current will be proportional to the dot product of the sensitivity vector "$\vec{d}(E)$" (perpendicular to the plane of the coil windings) and the magnetic field vector of the alternating field "$\vec{v}(P)$" at the location P (see inset showing the direction coil represented by vector $\vec{d}(E)$).

To measure the 3D orientation of the eye we need information from two search coils, which must be fixed to the eye ball in non-parallel planes. Thus, the second search coil, called *torsion coil*, with the sensitivity vector $\vec{t} = [t_1, t_2, t_3]^T$ should not be parallel to the first coil but rather perpendicular to it for optimal 3D decoding. The output signals t_v and t_w of the torsion coil can likewise be written as functions of the direction and position of the coil in the external field:

$$t_v(P,E) = \vec{t}(E) \bullet \vec{v}(P) = t_1 \cdot v_1 + t_2 \cdot v_2 + t_3 \cdot v_3 \tag{2-6}$$

$$t_w(P,E) = \vec{t}(E) \bullet \vec{w}(P) = t_1 \cdot w_1 + t_2 \cdot w_2 + t_3 \cdot w_3 \tag{2-7}$$

As in the previous two equations the dummy variable "*E*" stands for eye position. Eqs. (2-4) and (2-5) can be solved for d_2 and d_3, and Eqs. (2-6) and (2-7) can be solved for t_2 and t_3:

$$d_2 = d_1 \cdot a_2 + b_{2d} \tag{2-8}$$

$$d_3 = d_1 \cdot a_3 + b_{3d} \tag{2-9}$$

$$t_2 = t_1 \cdot a_2 + b_{2t} \tag{2-10}$$

$$t_3 = t_1 \cdot a_3 + b_{3t} \tag{2-11}$$

where, $a_2 = \dfrac{v_1 \cdot w_3 - w_1 \cdot v_3}{w_2 \cdot v_3 - v_2 \cdot w_3}$, $a_3 = \dfrac{v_2 \cdot w_1 - w_2 \cdot v_1}{w_2 \cdot v_3 - v_2 \cdot w_3}$, $b_{2d} = \dfrac{d_w \cdot v_3 - d_v \cdot w_3}{w_2 \cdot v_3 - v_2 \cdot w_3}$,

$b_{3d} = \dfrac{d_v \cdot w_2 - d_w \cdot v_2}{w_2 \cdot v_3 - v_2 \cdot w_3}$, $b_{2t} = \dfrac{t_w \cdot v_3 - t_v \cdot w_3}{w_2 \cdot v_3 - v_2 \cdot w_3}$, and $b_{3t} = \dfrac{t_v \cdot w_2 - t_w \cdot v_2}{w_2 \cdot v_3 - v_2 \cdot w_3}$.

Assuming a rigid geometric configuration of the direction search coil, the sensitivity, represented by the vector length, can be obtained *a priori* from a calibration of the search coil at the center of the field (for details see Section 2.3.5):

$$\left|\vec{d}\right| = \sqrt{d_1^{\,2} + d_2^{\,2} + d_3^{\,2}} \quad \text{(measured at P=0)} \tag{2-12}$$

Then d_1 can now be found by substituting Eqs. (1-8) and (1-9) in Eq. (1-12):

$$ad_1^{\,2} + b_d d_1 + c_d = 0 \tag{2-13}$$

where $a = 1 + a_2^{\,2} + a_3^{\,2}$, $b_d = 2a_2 b_{2d} + 2a_3 b_{3d}$ and $c_d = b_{2d}^{\,2} + b_{3d}^{\,2} - \left|\vec{d}\right|^2$

Solving Eq. (2-13) yields two solutions for d_1 with opposite signs. The actual sign depends on the winding direction of coil, which can be determined from the calibration. It is important to note that a two field system with primary fields in *y*- and *z*-directions, as indicated in Eqs. (2-4) and (2-5), only allows measurements of less than ±90° from the *x*-direction for the direction coil and loses accuracy when approaching this limit. The limit can also be described by a plane spanned by the *y*- and *z*-directions. Direction coil directions beyond the limit are indistinguishable from those within the limit and will therefore by itself be assumed to be within the limit. In practice, it is the torsion coil of the dual search sensor that will reveal if the limit is exceeded.

Because of this limitation of a two field system it is not possible to reliably predict t_1 from the vector length since this coil is likely to operate close to the plane spanned by the *y*- and *z*-directions. However, by assuming that the relative orientation of the torsion and direction coils remains constant, we can use the information about the configuration of the coil vectors from the calibration to calculate the angle ρ between the two coils:

$$\cos(\rho) = \left(d_1 t_1 + d_2 t_2 + d_3 t_3\right) \Big/ \left(|\vec{d}\,||\,\vec{t}\,|\right) \tag{2-14}$$

, measured at P=0.

And by substituting Eqs. (2-10) and (2-11) in Eq. (1-14), we obtain for:

$$t_1 = \frac{|\vec{d}\,||\,\vec{t}\,|\cos(\rho) - d_2 b_{2t} - d_3 b_{3t}}{d_1 + d_2 a_2 + d_3 a_3} \tag{2-15}$$

Finally t_2 and t_3 are obtained from Eqs. (2-10) and (2-11).

Because of the geometry underlying Faraday's law of induction, the structure of the rotation matrix is closely related to the search coil vectors. Even though we will ultimately use rotation vectors for describing the eye orientation the most straightforward way to evaluate the search coil signals is in the format of 3 × 3 rotation matrices using Euler angles before transforming them into other representations (see Appendix A.5 for a short review of the definition and properties of rotation vectors).

The rotation matrix describes the 3D orientation relative to the field frame by three orthonormal vectors in right-handed orientation. Thus the first column simply is the normalized direction coil vector:

$$\hat{d} = \left[\hat{d}_1, \hat{d}_2, \hat{d}_3\right]^T = \vec{d} \Big/ \left|\vec{d}\right| \tag{2-16}$$

The second column is the unit vector that aligns with the direction of the projection of the torsion coil vector onto the plane orthogonal to the direction coil vector. With $\hat{t} = \vec{t}/|\,\vec{t}\,|$ we have:

$$\hat{t}^{\perp} = \left(\hat{t} - \hat{d}\cos(\rho)\right) \Big/ \left|\hat{t} - \hat{d}\cos(\rho)\right| \tag{2-17}$$

Finally, the last column-vector, which must be orthogonal to the first two column-vectors, is the cross product of the first and second column. Thus, the resulting rotation matrix at point *P* reads:

$$R(P) = \begin{bmatrix} \hat{d}_1 & \hat{t}_1^{\perp} & \left(\hat{d} \times \hat{t}^{\perp}\right)_1 \\ \hat{d}_2 & \hat{t}_2^{\perp} & \left(\hat{d} \times \hat{t}^{\perp}\right)_2 \\ \hat{d}_3 & \hat{t}_3^{\perp} & \left(\hat{d} \times \hat{t}^{\perp}\right)_3 \end{bmatrix} \tag{2-18}$$

Note that this rotation matrix describes the orientation of the dual search coil relative to the magnetic field frame, which is not necessarily aligned with gaze direction. The orientation of the eye relative to the dual search coil can be determined from a calibration (see Section 2.3.5).

2.3.3 Biot-Savart based- versus experimentally measured magnetic field characteristics

To compare the calculated field based on the Biot-Savart law with the actual magnetic field characteristics we used a custom-made robot that systematically moved three mutually orthogonal single search coils (diameters of 20 mm) inside the magnetic field frame. We recorded the 3D linear positions of the search coils together with the induced currents at every second centimeter in the *x*-, *y*- and *z*-directions in one octant of the Primelec system and mirrored the data to the other octants in order to map out the magnetic field. The measured magnetic field vectors were then normalized to unity at the center of the primary fields and interpolated (cubic spline) to obtain an estimate of the magnetic field at the relevant positions inside the field frame. Based on these measurements, the magnetic field was used to demodulate search coil signals in a similar way as described for the calculated field in the previous section (using the Biot-Savart law). A comparison between the two methods was made with the data recorded in the simulation experiment described in the following section.

2.3.4 Validation procedures based on simulated 3D eye positions

This procedure was used to measure the quality of the theoretically calculated and robot measured magnetic fields in terms of precision and accuracy of 3D eye position demodulation. For this, we mounted a test dual search coil on a three-axis gimbal protractor, which could be rotated through any angle in horizontal, vertical and torsional directions (for a description of the nesting of the gimbal axes see Hess et al., 1992). The protractor was tracked with an optical position measurement system for precise positioning inside the magnetic field (OPTOTRAK 3020, Northern Digital, Canada).

We recorded the induced output for nine different orientations of the dual search coil: reference orientation (0° for all axes) and all combinations of ±30° horizontal, ±30° vertical and ±20° torsional directions (see Table 2 in Hess et al., 1992). The orientation was determined by reading off the values on each axis of the gimbal protractor. This procedure was repeated at each of 25 positions in the *x*–*y* plane (Figure 2-3A), as well as at three additional positions towards the upper right front corner of the magnetic field frame (Figure 2-3B, positions FRU1, FRU2 and FRU3), giving a total of 252 samples (9 × 28) for each of the three dimensions (horizontal, vertical, and torsional).

In the *x*- and *y*-direction, the field was measured every 5 cm whereas along the diagonal (in the *x*–*y* plane) recordings were made at intervals of 7.1 cm (i.e. displaced 5 cm in the *x*- and 5 cm in the *y*-direction). Positions along the *z*-direction (above the *x*–*y* plane) were likewise spaced out at 5 cm intervals, yielding diagonal intervals between recording points in the *x*-, *y*- and *z*-direction of $\sqrt{5^2+5^2+5^2}cm = 8.66cm$. For each position with each orientation of the dual search coil, the difference between the actual orientation on the gimbal protractor and the predicted orientation from the induced currents was compared, with and without using the Biot-Savart based demodulation or by using the demodulation based on the experimentally measured magnetic field.

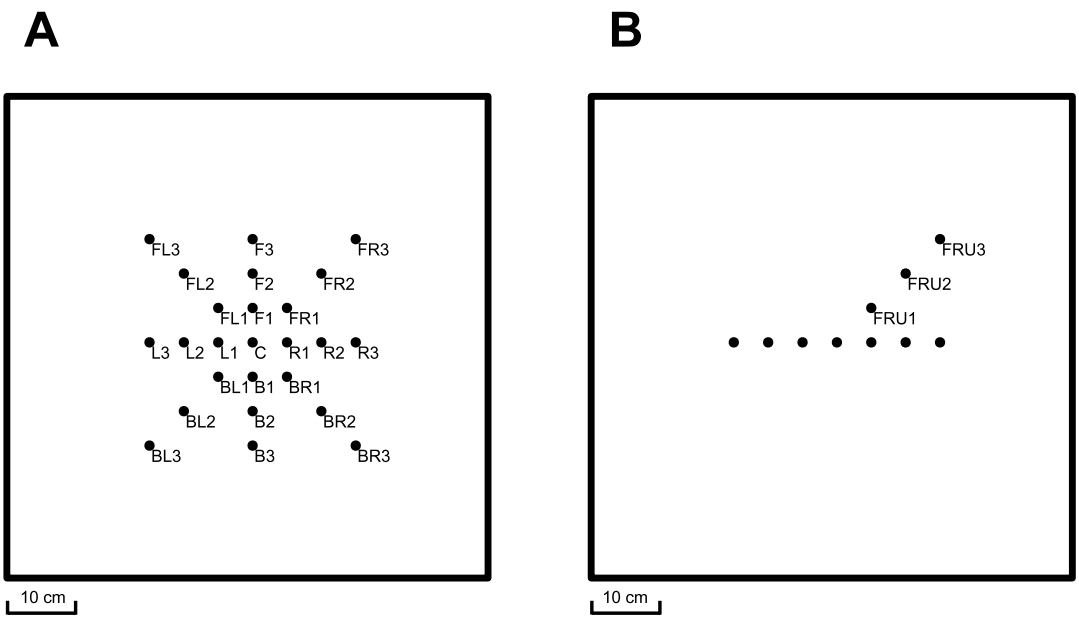

Figure 2-3. Gimbal positions

A: Top-view of the 25 positions in the horizontal plane where the gimbal was placed. The 30 × 30 cm measured plane cuts though the center of the field frame with side lengths of 75 × 75 × 75 cm. *B*: Behind-view of the three additional positions recorded towards the upper right front corner. The seven unlabeled dots indicate the edge-on view of the plane of 25 positions shown in *A*.

2.3.5 Calibration of dual search coil parameters with two primary fields

In contrast to systems with three primary fields, 3D search coil recordings in systems with only two primary fields require a precalibration to characterize the sensitivities and mutual orientations of the two coils constituting the dual search coil. This precalibration, also called *in vitro* calibration needs to be done prior to applying the coil on the eye and requires a rigidly assembled dual search coil. We thus determined the sensitivity of each of the two search coils, and the angle between them by measuring the induced currents after rotating the dual search coil with the help of a gimbal protractor in the center of the field frame to known orientations. The orientation of a dual search coil (on the eye/gimbal) was determined by a second calibration, called *in vivo* calibration, during which the

subject with the head at rest fixated vertical targets placed in the sagittal plane though the eye at known vertical angles. Because only two of the three components of the orientation of the search coil are captured by a two field system, the third component had to be computed from the predetermined sensitivities of the direction and torsion coil in the *in vitro* calibration. For a complete and detailed explanation of these procedures see Hess et al. (1992) and for calibration of non-rigid search coils see e.g. Bartl, Siebold, Glasauer, Helmchen & Buttner (1996).

Although it is not always possible to situate the subject so that the eye with the search coil is exactly in the center of the primary fields during the calibrating procedure, this usually poses no problems as long as the subsequent experiments are performed in the same position. In head-unrestrained experiments, however, it is desirable to obtain the calibration parameters from the center of the magnetic fields because offset voltages, which are not related to the coil orientation in the magnetic fields, can only then be distinguished from the non-linear distortions. To overcome this problem we introduced a recursive method to estimate the offset voltages even when the calibration was performed in the non-linear part of the magnetic field. In an initial step, the Biot-Savart correction was applied to the raw output signals; the offsets were calculated and subtracted from the raw output. In the subsequent steps, this procedure was repeated as follows: the Biot-Savart correction was applied now to the (first order) offset-corrected output signals, new offset voltages were computed and the summed (first and second order) offset voltages were subtracted again from the raw output signals. This recursive loop was run until the Biot-Savart corrected output signals yielded near zero (high-order) offset voltages (Figure 2-4). As a consequence, the recursively computed coil parameters and the accumulated offsets reached values after the last iteration as if the calibration was done in the center of the magnetic field. A reasonable accuracy is usually obtained after about 4–5 iterations.

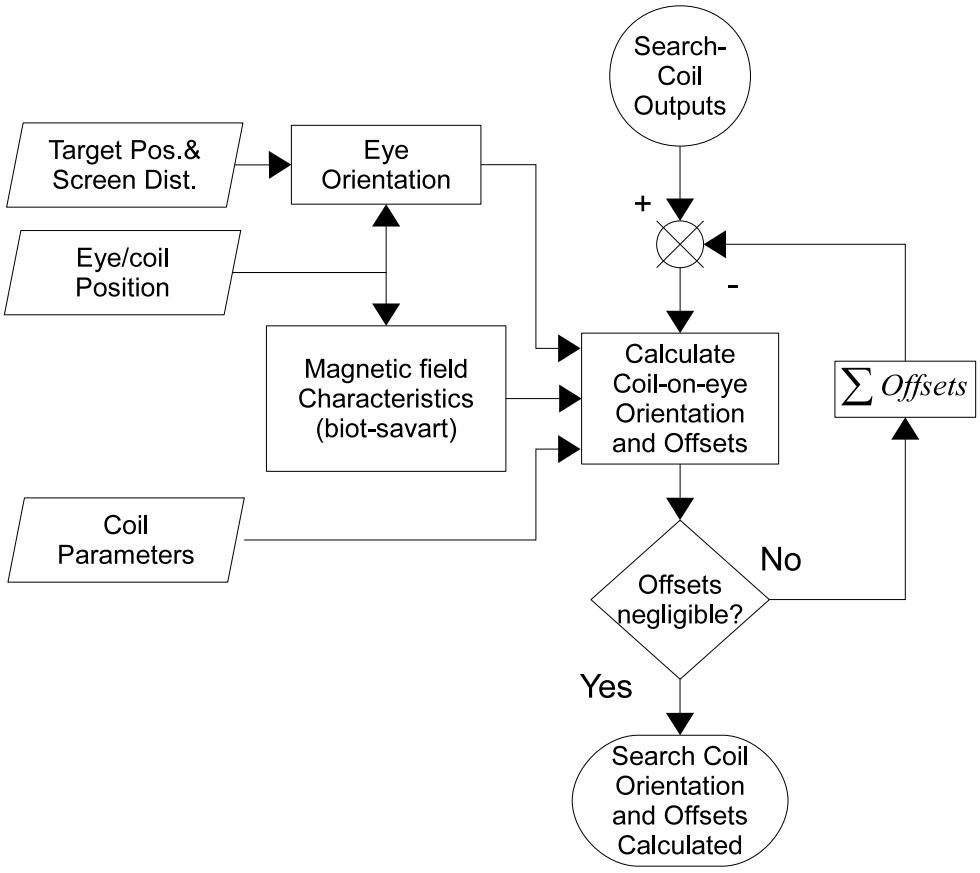

Figure 2-4. Functional block diagram of the procedure for obtaining calibration parameters.

The calibration parameters are calculated by correcting the entire search coil output measured in the non-linear part of the magnetic field and are then corrected recursively to minimize the offsets.

2.3.6 Validation procedures based on eye–head movement recordings in non-human primates

Four female rhesus monkeys (Macaca mulatta, body weights 5–6 kg), prepared with skull bolts for head restraint, were used in these validation procedures as an integral part of a larger project with wider scope. Dual search coils were implanted on one eye under general anesthesia as described in Hess (1990). All procedures and animal care protocols accorded with the NIH Guide for the Care and Use of Laboratory Animals and were approved by the Veterinary Office of

the Canton of Zürich. The animals were trained to fixate nine targets, presented sequentially at locations forming a 3 × 3 matrix with equally spaced rows and columns ranging from −20° to 20°, using a custom-made software package based on Spike2 that controlled LED point targets, the reward delivery and the data acquisition (1401*plus* and Spike2, Cambridge Electronic Design Ltd., Cambridge, England).

The head position and orientation was recorded using a compact ultrasonic tracking device (CMS 20, Zebris Medical GmbH, Isny, Germany). To ensure undisturbed data recording the head position data was routed through a dedicated PC to ensure stable data rate at 200 Hz before being forwarded via a DAC to the main acquisition hardware.

Three ultrasonic emitters were rigidly mounted to the subject's head to measure the translation and rotation of the head. From this, the spatial position of the eye (and thus of the dual search coil) was calculated relative to the field frame. The calculated magnetic field characteristics at the current location of the dual search coil was then used to determine the exact orientation of the coil relative to the external field frame, from which eye-in-space orientation relative to gaze straight-ahead was determined. To reward the animal for accurate target fixation, the search coil signals were demodulated online according to the current spatial position of the eye in the magnetic field. Horizontal and vertical gaze directions, recorded at the time of fixation, were evaluated off line with- and without the Biot-Savart based demodulation. The gaze was corrected for the effect of parallax due to a translation of eye relative to the space-fixed targets. Three dimensional eye movements were measured but the accuracy and precision were only evaluated for the horizontal and vertical directions (relative to the target positions). The torsional eye components in this *in vivo* experiment lack the presence of a natural reference since the head was free to move, i.e. Listing's law was not obeyed (Collewijn et al., 1985; Glenn & Vilis, 1992; Hess, 2008). Figure 2-5 shows a diagram of the steps necessary for calculating the current gaze direction from the recorded search coil and head position sensor signals.

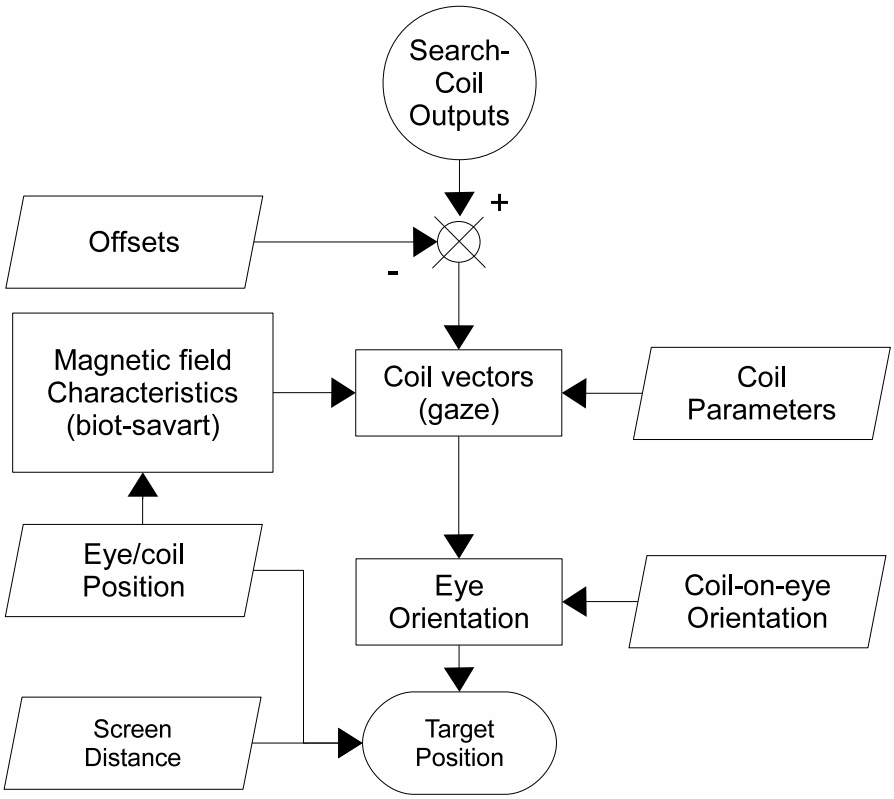

Figure 2-5. Functional block diagram showing the practical algorithm used for calculating the angular direction of the target that the eye was fixating.

The rhomboids denote input parameters and the rectangular boxes denote the algorithm.

2.4 Results

2.4.1 Biot-Savart based demodulation of simulated 3D eye position measurements

The data for the 28 positions in the primary field was collected in 10 groups according to their distance to the center: In the center (group A), at the positions F1, R1, B1 and L1 which were all 5 cm from the center (group B, see Figure 2-3A), and likewise in the other positions with matching distances to the center (collected in groups C thru J, see Fig. 3A and B and inset in Figure 2-6).

As expected, the error increased relatively rapidly relative to the distance to the center (thick curve in Figure 2-6). The data corrected with the Biot-Savart-based demodulation (thin solid curve), however, showed a significant improvement in the accuracy ($P < 0.05$, Wilcoxon signed-rank) for all groups, except the center group, which had a *P*-value of 1 as expected since no correction was performed at this position. The error scores at individual positions, without grouping, were also significantly improved, except at positions F1, FL1 and B1.

The correction performance was considerable for all three dimensions of rotation as demonstrated in Figure 2-7, which shows a box plot of the grouped data separated in each of the three dimensions. The horizontal lines in each box denote the median, the upper- and the lower quartiles. The whiskers from the boxes show the minimum and maximum error measured. The upper row shows the uncorrected errors for each of the three directions, horizontal, vertical and torsional. The respective plots for the Biot-Savart based corrected errors are shown in the three lower plots. It is remarkable that in this 75 cm field frame already positions further than only 15 cm from the center gave very unpredictable measurements with occasionally more than 10° and more than 3° error on average when the magnetic field non-linearities were not taken into account.

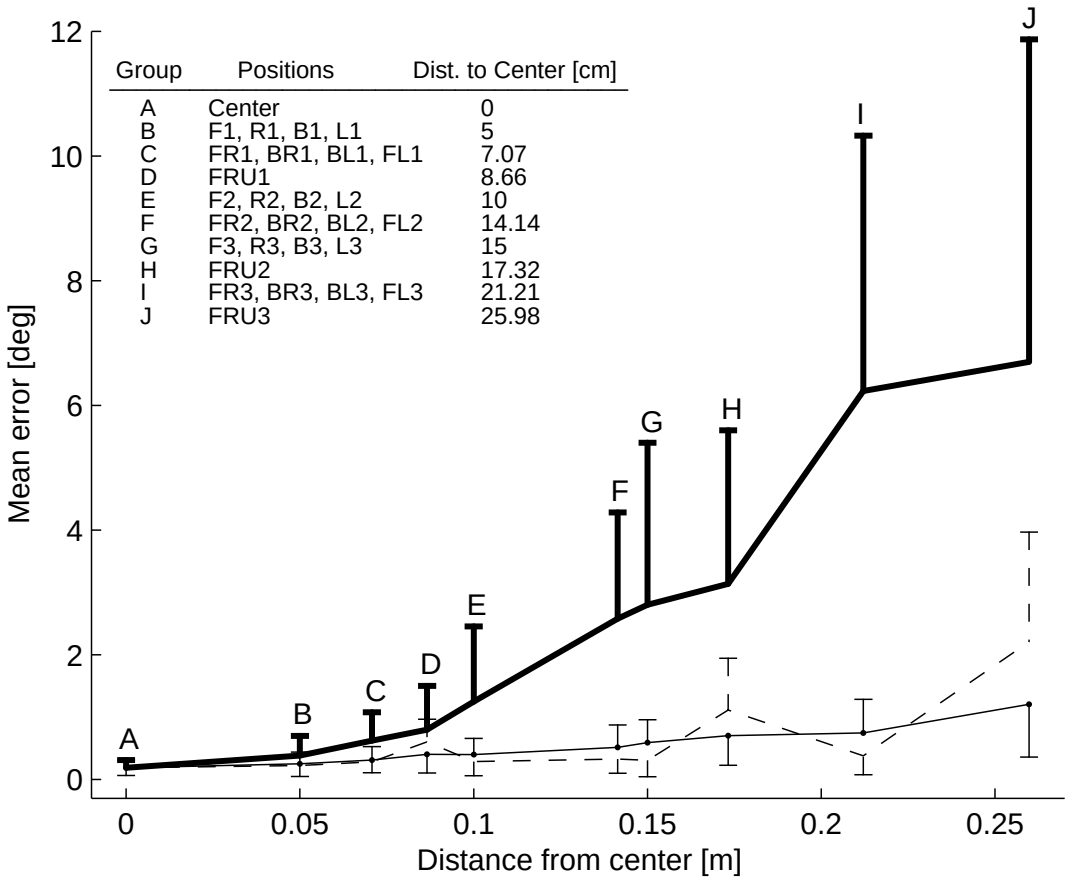

Figure 2-6. Average demodulation error expressed as difference between actual and demodulated direction of a test coil at positions ordered by distance to center.

The thick curve shows the uncorrected demodulation (assuming linear field characteristics), the thin solid curve shows Biot-Savart corrected demodulation and the dashed curve shows the errors when using the experimentally measured field characteristics. Error bars are one standard deviation. Inset: Table of groups with matching distance to the center.

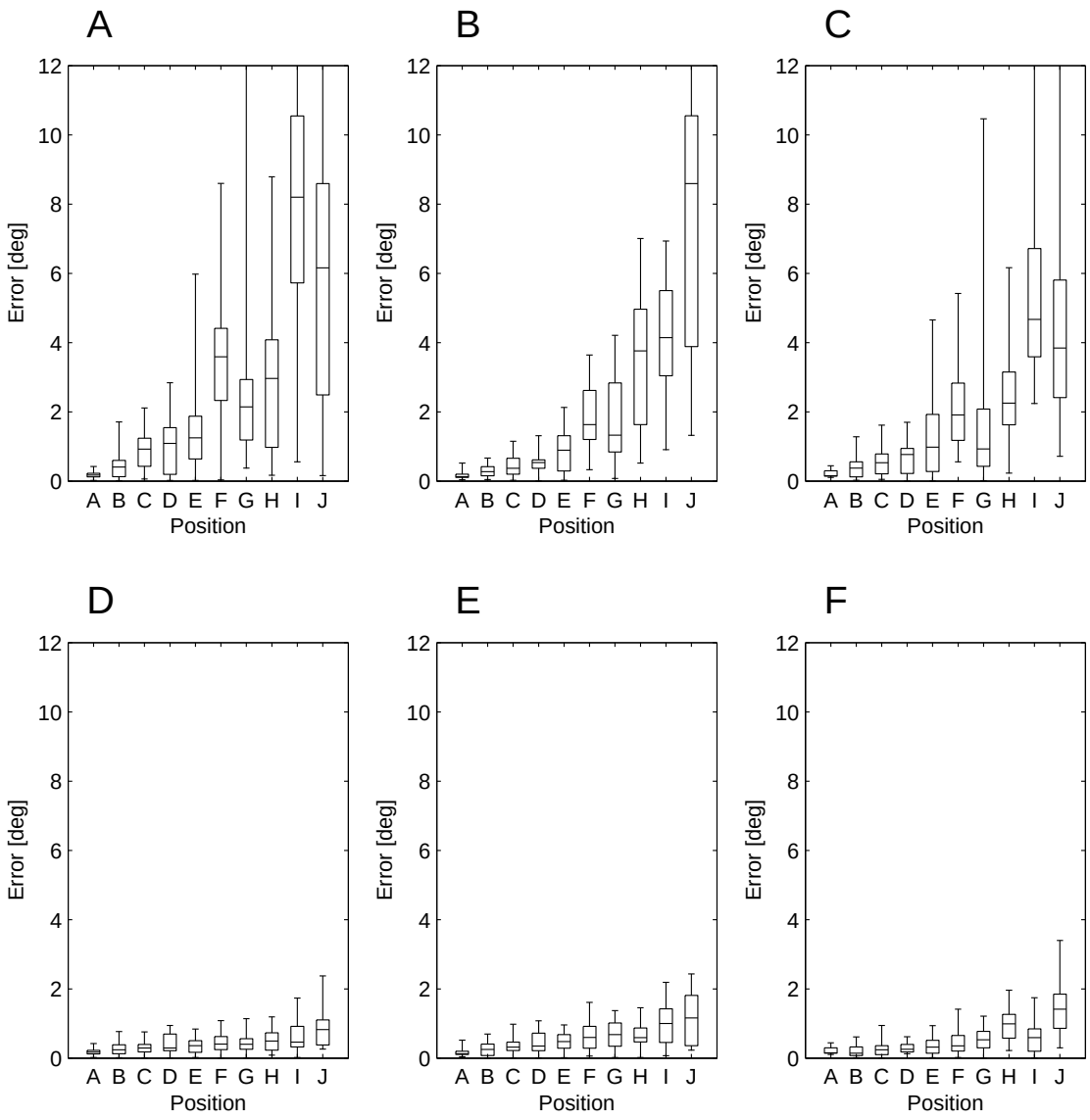

Figure 2-7. Box plot showing the error of the demodulation.

Subplot *A*, *B* and *C* show horizontal, vertical and torsional errors, respectively, when the data was not corrected. *D*, *E* and *F* are the same but showing errors after Biot-Savart based correction. Position A shows the error measured in the center of the field. Positions B thru J shows the errors at the grouped positions in order of distance to the center (see table inset in Fig. 6).

2.4.2 Biot-Savart based- versus experimentally measured magnetic field characteristics

To compare the two approaches we used the data from the simulated 3D eye positions and demodulated it using the experimentally measured magnetic field characteristics in a similar way as was done when using the Biot-Savart based calculations. This showed no significant overall difference in performance between the two procedures (dashed versus solid curve in Figure 2-6), although the Biot-Savart procedure seems to have a more stable increase in error versus distance to center and to perform better for the three groups D, H and J, which are the positions towards upper right front corner but slightly worse for the other groups (the positions in the *x–y* plane).

2.4.3 Biot-Savart based demodulation of eye–head movement recordings in non-human primates

The *in vivo* experiments showed significant improvements in the measured accuracy of fixations performed during head movements when applying the described method. The mean errors for corrected and uncorrected fixations measured in four animals for the nine fixation targets were in the range of 0.64–0.93° and 1.56–4.89° respectively. The uncorrected error depended highly on the relative contribution of the head to the gaze movement. Although the targets were well within the oculomotor range (±20°) so that it was not necessary to move the head, all four animals typically used also the head to variable degrees to fixate the targets. As indicated by the data in Table 2-1, subjects P and M moved the head less than subjects X and L for the same task.

The error score for uncompensated fixations, defined as the distance in degrees between the target and the calculated fixation point, originated from a lack of both accuracy and precision. The accuracy, which can be described as a general shift of the fixation points relative to the target of interest, had two sources (Figure 2-8A): A common shift of eye position of the individual trials for each target due to the correlation of the mean spatial eye position with target position.

E.g. when the target was to the left, the subject generally tended to turn the head to the left, which translated the eye to the left side of the field frame, causing parallax and distortion due to the non-linearity of the magnetic field. The second source, causing a general shift, came from the fact that the overall average of spatial eye positions during the experiments was different from the position where the calibration (with the head restrained) was obtained. To minimize this bias, we attempted to restrain the head in a position as natural (and comfortable for the animal) as possible, in order to obtain the calibration as close as possible to the mean position that the animal was going to assume during the head-unrestrained experiments. A third source of error in the uncompensated fixations was the precision, or the scatter of the fixation directions aimed at a particular target, which reflects the scatter in spatial eye positions for that particular target. This can also be described as biological noise, since it is a consequence of the variation in the ratio of eye and head movement. That is, for a given target fixation the contribution of head movement can be small and the eye movement large or vice versa. As seen in Figure 2-8B, the algorithm improves both accuracy and precision.

Subject	No. of fixations	Uncorrected mean error ± std	Corrected mean error ± std
P	136	1.91 ± 0.67°	0.93 ± 0.48°
M	155	1.56 ± 0.85°	0.64 ± 0.40°
X	24	4.89 ± 1.77°	0.93 ± 0.51°
L	102	4.13 ± 1.94°	0.59 ± 0.35°

Table 2-1. Mean errors and standard deviations for fixations in the four subjects.

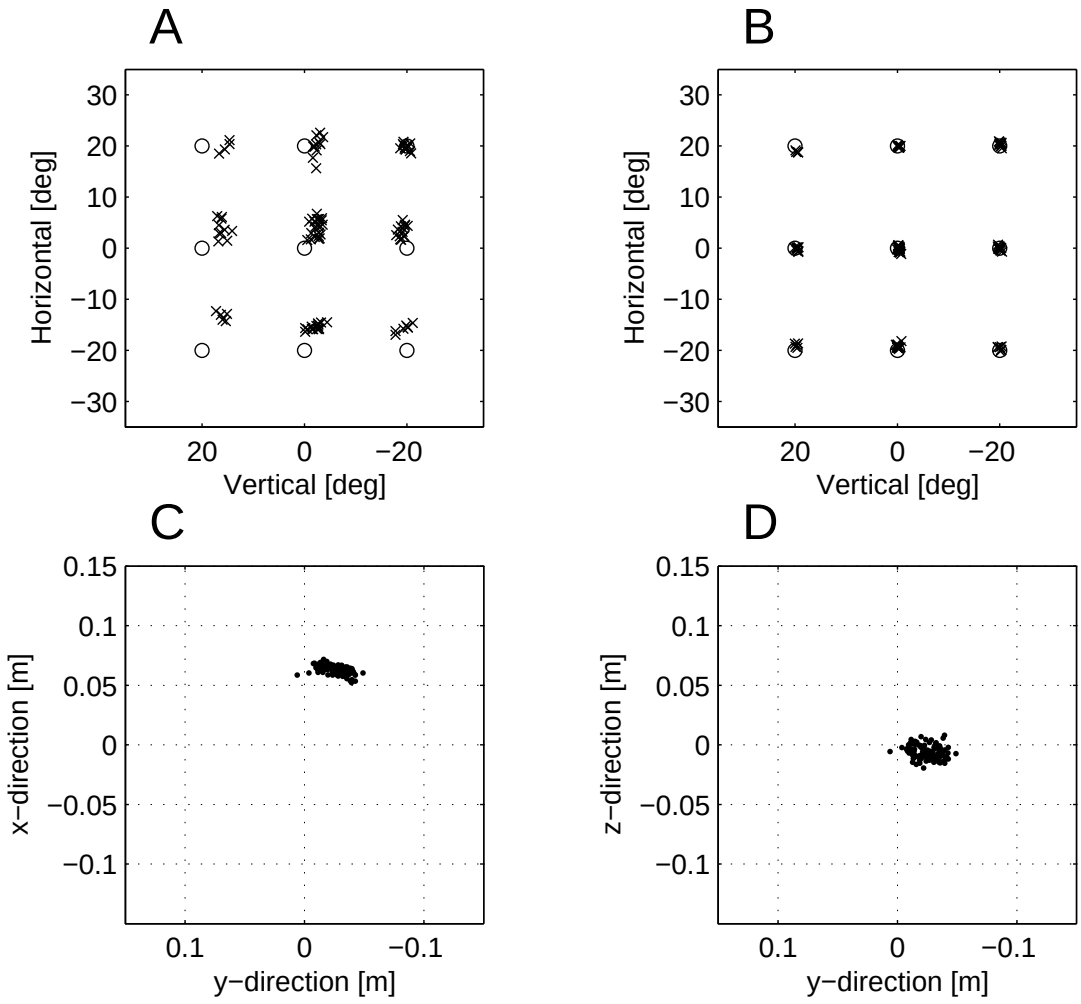

Figure 2-8. In vivo fixations.

One-hundred and two fixations, marked by crosses, made by subject 'L' towards nine targets marked by circles. *A*: Uncorrected fixations. *B*: Biot-Savart based corrected fixations. (*C* and *D*) Top-view and behind-view, respectively, of eye positions in the magnetic field at the time of the fixations.

2.5 Discussion and conclusions

We have quantified the errors in 3D eye movement recordings obtained in the head-unrestrained rhesus monkey during a fixation task, using the magnetic search coil technique in a cubic primary field frame of only 30 cm side length. We developed a method that efficiently minimizes the errors by accounting for the characteristic non-linearities of the magnetic field by using the Biot-Savart law. We show that by this method 3D eye movements can be recorded in the head-unrestrained rhesus monkey during a fixation task with nearly the same precision and accuracy as when 3D eye movements were recorded in the center of the magnetic field, which typically requires restraining head movements.

In the *in vivo* experiments the location of the eye in the external field was on average 4–7 cm from the field center of the 30 cm cubic frame. In comparison with the 75 cm field frame, which was used in the *simulations*, these distances translate into 10–17.5 cm. Comparing the average errors at comparable distances from the field center, there is a good correspondence between the errors measured in the *in vivo* and the *simulation* experiments, suggesting that the errors found in the *simulation* can serve as a predictor of the errors in *in vivo* recordings (see Figure 2-6). The robot-controlled measurements mapping out the magnetic field characteristics offer no practical advantage over calculating the field characteristics with the more effortless 'stick method'. The here presented Biot-Savart demodulation technique allows one to perform eye–head movement studies at sufficiently high precision in all degrees of rotational and translational freedom within relatively compact primary magnetic field frames.

Alternatively to our approach several other studies have shown that artificial neural networks, trained with back propagation on a subset of sampled fixation data, can be used to calibrate eye movements or eye–head movements in 2D, at least in the homogeneous range of the magnetic field (Goossens & Van Opstal, 1997; for EOG measurements: Coughlin, Cutmore & Hine, 2004; Bremen, Van der Willigen & Van Opstal, 2007). In fact, a similar procedure could be used for

calibrating the 2D eye movements in the non-homogeneous range. A difficulty in applying this approach for calibration of 3D eye position would be to specify appropriate assumptions about the torsion that the eye assumes during 2D gaze shifts in the head-free condition. Without such assumptions, training of the artificial neural network on a subset of all accessible targets would not yield physiologically meaningful torsion. The reason for this is that although it is not possible to voluntarily control ocular torsion during target fixation, the actual amount of torsion is in general not only a function of gaze direction but depends also on other parameters like head orientation relative to gravity or other vestibular signals. Since our primary interest was to develop a model-free calibration method in order to be able to study gaze control in stationary as well as non-stationary environments, an implementation of artificial neural network techniques was beyond the focus of this study.

Real-time application of the here presented Biot-Savart demodulation technique depends on measuring online head position within the field frame. For this we used a small-sized sensor system, using travel time measurements of ultrasonic pulses, which fitted in the limited space available above the subjects head. The main disadvantage of this solution is the relatively narrow temporal bandwidth due the comparably slow sonic travel speed. An elegant way to overcome this restriction would be to equip the conventional two-field system used here for measuring 3D eye movements with a gradient magnetic field along the third dimension (*x*-direction). As shown by Schilstra & van Hateren (1998a; 1998b), such a configuration would in fact allow one to measure head orientation and position with a 3D miniature sensor mounted on the subject's head. Thus, this technique for measuring head position (and orientation) in combination with the here presented Biot-Savart demodulation technique in a conventional two-field system, using an easy implantable dual search coil, can be used for reliably measuring 3D eye position during head-free gaze shifts irrespective of the off-center magnetic field non-linearity.

3. Gaze control during target tracking in the periprimary oculomotor range*

3.1 Abstract

Gaze control in a periprimary range of ±15° is typically dominated by eye movements due to the much smaller inertia of the eye compared to the head. Although considerably more sluggish head movements help keeping the eyes close to primary position. For large gaze saccades in oblique directions, it has been shown that (1) the head has a preference for moving in the horizontal direction while the eye moves preferentially in the vertical direction and that (2) the head orientations in three dimensions resemble the motions of a Fick-gimbal (Fick-like strategy), either due to the alignment of the interocular axis with horizon or as a result of the particular anatomical configuration of the head–neck motor system.

Using two geometrically complementary paradigms, one involving active and the other compensatory eye–head movements, we investigated to what extent these behaviorally different strategies also hold for eye–head movements in the subject's periprimary oculomotor range, defined as movements within ±15° of straight ahead.

Our results show (1) that there is a clear eye–head directional specificity in accordance with the behavior observed during large eye–head gaze saccades yet due to anatomical rather than a dynamic (neural) energy conservation mechanism, and (2) that the Fick-like strategy found in head orientations between large eye–head saccades is not an appropriate description of the strategy underlying small eye–head movements. Even though we show that the effects of

* A preliminary account of this work has been presented at the Society for Neuroscience Annual Meeting in 2009 with the abstract: J. S. THOMASSEN, B. J. M. HESS. Direction specific eye-head coordination during target tracking in the periprimary oculomotor range. Program No. 559.17. 2009 Neuroscience Meeting Planner. Chicago, IL: Society for Neuroscience, 2009. Online.

a Fick-like strategy could reliably be measured in such relatively small range of movements if at all present our results indicate a behavioral strategy optimizing fixed-axis movements (Listing's law).

3.2 Introduction

By rotating the eyes in the orbit we direct the small high acuity region of the retina, called the fovea, onto objects of interest. The visual line from the fovea to the target is called the line of sight. Controlling the direction of the line of sight requires control of just two out of the three rotatory degrees of freedom of the eye namely control of the one in the horizontal and the other one in the vertical direction. However, to completely determine the eye's orientation in the head (or re space) additional control of its torsional degree of freedom is required, which ultimately specifies the orientation of the eye *around* the line of sight, also called cyclo-torsion. Donder's law for eye movement says that for any direction of the line of sight the cyclo-torsion of the eye is independent of how the eye rotates to reach that particular orientation (Donders, 1848). It was Johannes Listing, who first described a particularly simple variant of Donders' law that is characterized by a simple trigonometric relation between the direction of the line of sight and the cyclo-torsion of the eye, now called Listing's law (as reported in: Handbuch der Physiologischen Optik by H von Helmholtz, 1867). See also section 1.5.
The head can also contribute to redirecting the line of sight since it provides the reference frame of the eye with respect to space and in that way extends the limits of eye rotation relative to space (see section 1.4 about reference frames). In this more general condition the torsion of the eye is no longer subject to Listing's law, because it can now be affected by the vestibulo-ocular reflex (VOR). This reflex seeks to keep the eye stable in space: Whenever the head passively moves the VOR rotates the eye around the same axis as the head but in the opposite direction, which typically violates Listing's law (see description of the half-angle rule in section 1.5). During combined eye–head saccades, on the other hand, the eye will typically start to rotate before the head, due to the difference in inertia of the eye and head, and it can initially violate Listing's law by anticipating the subsequent head movement. Thus the system not only directs gaze towards the

target, but it also controls the ocular cyclo-torsion so that Listing's law is obeyed in the new reference position when the head has rotated to its new orientation (Tweed, Haslwanter & Fetter, 1998; Crawford, Ceylan, Klier & Guitton, 1999). Thus the oculomotor system anticipates the new 'workspace' (reference frame) of the eye and the more sluggishly moving head simply rotates around the eye keeping it stable in all three dimensions relative to space, facilitated by the VOR. See also section 1.2 and 1.3.

This predictive strategy provides evidence that the head and eye motor systems share higher level gaze commands and that the final orientation of the eye relies on the orientation of the workspace provided by the final head orientation. The strategy may also suggest that head movements obey Donders' law. When rotations obeying Listing's law are represented by rotation vectors the end-points of the vectors lie in a plane called Listing's plane. There has been a debate whether the head orientation is restrained to such a Listing's plane like the eye or whether it follows another restraint similar to that of a Fick gimbal (another variant of Donders' law).

It has been shown that within a limited range of eye–head gaze shifts head orientation seems to follow Listing's law (Straumann, Haslwanter, Hepp-Reymond & Hepp, 1991; Tweed & Vilis, 1992). In fact, Straumann et al. demonstrated that head orientation for movements within ±25° was restricted to a plane as required by Listing's law. The restriction was relative to the local workspace (not body-fixed) in a similar manner as the restriction for the eye is relative to the workspace provided by the head (and not the body). In the following, this restriction for head orientation will be called the "*workspace hypothesis*". Examination of larger eye–head gaze shifts later showed that in this range the head followed a Fick-like strategy. This finding raised the question whether measuring head movements in a too small range might mask the curvature of the twisted surface since it might look like a plane in analogy to a circle's arc that appear straight if the inspected part subtends a too small angle. This explanation will be called the "*Fick-like hypothesis*" (Humans: Glenn &

Vilis, 1992; Radau, Tweed & Vilis, 1994; Non-human primates: Crawford et al., 1999).

In case the inspected head movement range becomes large and approaches the limits of head movement relative to the torso, the orienting behavior might be defined by the anatomy of the neck and the way the articulations of the cervical vertebrae in combination with the atlanto-occipital joint favors a Fick-like strategy (Glenn & Vilis, 1992). A Fick-like strategy could, however, also be of a neural origin since it preserves the interaural axis horizontal and thus keeps the eyes leveled at the horizon when the body is upright (Glenn & Vilis, 1992; Hore, Watts & Vilis, 1992).

To investigate the neural based head orienting behavior and the coordination of eye and head we compared two complementally paradigms: (1) a circular smooth pursuit task and (2) a fixation task where the torso of the subjects was rotated in a way which made the fixation point, relative to the torso, move in an analogous circular fashion. The purpose of the two tasks was to enable us to discriminate, in the periprimary range, whether the head orienting behavior is a strategy that serves to keep the eyes leveled (Fick-like hypothesis) or whether Listing's law in the workspace is obeyed (workspace hypothesis). In addition, the two paradigms also enabled us to investigate the underlying cause of the direction specificity seen in eye–head coordination, i.e. why the head prefers movement in the horizontal direction while the eyes move more in the vertical direction.

3.3 Methods

3.3.1 General experimental setup

Experiments were performed on four female rhesus monkeys (*Macaca mulatta*, body weights 5–6 kg). Each animal underwent two sessions of aseptic surgery under general anesthesia (isoflurane). In a first session they where prepared with an acrylic skull cap with four bolts embedded to allow head restrain when needed. In a second session, a dual search coil for measuring three dimensional (3D) eye movements was sutured to the sclera under the conjunctiva. The lead wires were led subcutaneously to a plug embedded in the skull cap. The dual search coil was manually assembled by integrating two miniature (torsional) coils at the periphery of a conventional (directional) search coil. For further details of this approach see Hess (1990). All procedures and animal care protocols accorded with the NIH Guide for the Care and Use of Laboratory Animals and were preapproved by the Veterinary Office of the Canton of Zürich.
During the experiments the animals were seated in custom-made primate chairs where the collar plate was approximately 30° forward tilted to enable unrestrained head movement within a range appropriate for the experiment. The chair was furthermore fitted with groves for the shoulders in the collar plate and a waist belt was used to restrain movements of the torso. The primate chair with the animal was placed inside the inner frame of a motorized 4-axis gimbaled motion device, from here on referred to as turn chair (Acutrol, Acutronic Schweiz AG, Bubikon, Switzerland). Visual targets were presented on the inner wall of a spherical dome (radius = 88 cm) that completely surrounded the turn chair. Depending on the task, either a fixed LED or a moving laser point controlled by a pair of mirror galvanometers presented the target.
The magnetic search coil technique (Robinson, 1963) was implemented with a magnetic field system fitted inside the inner frame of the turn chair (Eye Position

Meter 3000, Skalar Instruments, Delft, The Netherlands). Due to the limited space in the turn chair, the primary frame had a size of less than 30 cm. Thus, for the head unrestrained experiments performed in this work the search coil was not always located in the linear parts of the magnetic field due to the head movements. To ensure reliable eye movement measurements we compensated for the field non-homogeneity by taking the magnitude and direction of the magnetic field into account using the Biot–Savart law as described in detail previously (Thomassen et al., 2010).

The head position was tracked with an ultrasonic system which measured each of the three rotatory and translational degrees of freedom (DOF) of the head (CMS 20, Zebris Medical GmbH, Isny, Germany). The spatial positions of three ultrasonic emitters attached to the subject's head were evaluated relative to the location of four microphones placed approx. 20 cm above the subject's head in the turn chair. Since the eye and head trackers were placed inside the turn chair, the data was measured relative to the torso of the subject rather than the surrounding space. In this way the eye tracker measured eye orientation relative to the torso (Et) while the head tracker measured head position relative to torso (Ht). The eye relative to head (Eh) was calculated as described in Appendix A.5.

A reward delivery system provided the animals with a small liquid reward periodically throughout every successful trial. During the experiment two tubes were led down from the skull cap on each side of the head such that the reward could be delivered independent of head orientation. The whole setup, including the reward delivery system, was controlled by custom made software and the data were digitized at 833 Hz (1401*plus* and Spike2, Cambridge Electronic Design Ltd., Cambridge, England). For further details about the setup see Appendix C.1.

3.3.2 Visual tasks

The subjects were trained to perform two complementary tasks. In the first task, called smooth pursuit task (SP), the subjects were trained to track a small laser point moving along a circle (radius 15°, velocity at 0.1 or 0.2 Hz,) on the screen in clockwise (CW) or counterclockwise (CCW) direction and centered relative to the straight ahead reference position. In this task the turn chair was in upright position without moving.

In the second task, called 'circular fixation' (CF), the subjects were fixating the space fixed LED centered on the screen at the same reference position as in the smooth pursuit task while the turn chair rotated the subject's torso in yaw (around a vertical axis) and pitch (around a horizontal axis) such that the LED in front of the subject performed a circular motion relative to the subject (±15° amplitude, velocity at 0.067 or 0.1 Hz and 90° phase difference between the yaw and pitch axes). The two rotation axes were nested corresponding to a Fick-gimbal. In both tasks the subjects were able to freely move their heads to assist directing their gaze.

3.3.3 Data analysis

3D eye and head orientations were expressed as rotation vectors in space-fixed x- (orthogonal to the y- and z-coordinates), y- (interaural axis) and z-coordinates (head vertical axis). A rotation vector $\vec{r}$ describes an orientation of the eye (or head) as a rotation around an axis relative to a reference position, whereby the rotation vector is parallel with this axis and its length encodes the amount of rotation by the tangent of half the rotation angle, i.e. $|\vec{r}| = \tan(\theta/2)$. For easy readability, however, we converted the rotation vectors to orientation vectors $\vec{o} = \arctan(\vec{r}) \cdot 360/\pi$ with length $|\vec{o}| = \theta$ in degrees, before plotting (Haustein, 1989). The direction of rotation is defined by the right hand rule (i.e. when the thumb points in the direction of the vector the fingers curl in the direction of the rotation). The eye's orientation while looking straight-ahead was taken as

reference position and only the tip of the vectors are plotted (see section 1.4.3 or Appendix A.5 for information about rotation vectors).

To examine the eye and head coordination temporally and spatially the horizontal and vertical gaze components (represented as components of a rotation vector) were fitted with first order sinusoids and the amplitudes and phases of the fits were quantitatively compared. The quality of the fit was evaluated by the standard deviation (std) of the residuals.

To describe qualitatively and quantitatively how the head and eye conformed to Donders' law, second order surfaces were fitted to the rotation vector end points in a similar manner as described earlier by others (Tweed & Vilis, 1990; Glenn & Vilis, 1992; Crawford et al., 1999). The formula for the second-order surface used in the least-square fits was:

$$v_1 = \alpha_1 + \alpha_2 v_2 + \alpha_3 v_3 + \alpha_4 (v_2)^2 + \alpha_5 v_2 v_3 + \alpha_6 (v_3)^2 \qquad (3\text{-}1)$$

Where v_1, v_2 and v_3 are the rotation vector components of torsional, vertical and horizontal, respectively. The coefficient α_1 is the offset whereas the coefficients α_2 and α_3 are the vertical and horizontal slopes, respectively. The coefficients α_4 and α_6 are the vertical and horizontal curvatures, respectively, and α_5 is the twist of the fitted surface. When Listing's law is obeyed, α_4, α_5 and α_6 must be (near) zero since these coefficients define non-planar surfaces. Otherwise the surfaces characterize different embodiments of Donders' law. The conformity of Donders' law was measured qualitatively by the standard deviation of the residuals and was calculated separately for each trial. The data was furthermore fitted to first and third order surfaces and their respective mean standard deviations were compared. This part is discussed in Appendix B.

Unlike when fitting a surface to quaternions (see Glenn and Vilis 1992), the twist coefficient from rotation vector fits (not orientation vector), α_5, can be directly

used as an indicator for how much the twist resembles a Fick- or Helmholtz gimbal (see section 1.4.2) independent of the range of the fitted data. That is, when the underlying rotation of the eye in space resembles that of an object that is rotated with a Fick gimbal the fitted surface will have a twist (α_5) of –1 and if it resembles the rotation performed with a Helmholtz gimbal it will have a twist (α_5) of +1. Eq. (3-2) provides a quantitative measure of this relationship:

$$\alpha_5 = \frac{v_1}{v_2 v_3} \tag{3-2}$$

Second order surface fits can assume four main shapes (Figure 3-1). When analyzing circular movements the surfaces can be described in the following manner: (A) a constant torsion which gives an offset of the fitted plane (coef. α_1), (B) a torsion sensitive to the horizontal or vertical direction and with the same frequency which gives a tilted plane (coef. α_2 or α_3), (C) a torsion sensitive to the horizontal or vertical direction but with the double frequency which gives a curved surface (coef. α_4 or α_6) and (D) a torsion sensitive to both horizontal and vertical directions and with the double frequency which gives a twisted surface (coef. α_5).

Even though the subjects often performed smooth pursuit (SP) or circular fixation (CF) for several cycles, all data was separated and analyzed in single cycles only (both sinusoidal and surface fits). The data was selected to only use trials were the behavior was relative stable and continuous. That is, data from the beginning of the tasks where the initial head position had an effect was discarded. The data were analyzed using MATLAB (The Mathworks Inc., Natrick, MA, USA) and statistical analysis consisted of one-tailed one-sample t-tests.

Procedure of trial selection for surface fitting

In the experiments, the head was free to move but did not necessarily have to move since the target was always well within the oculomotor range. Trials with a span of less than 5° of head rotation in any direction in the horizontal–vertical plane where omitted from the surface analysis. This was done in order to avoid fitting a surface to points that were scattered around a point or in a single dimension which therefore would yield unreliable plane fits. To find the direction in the vertical–horizontal plane which had the minimum data spread a least-square fit was performed with the formula:

$$f(x) = \max(a) - \min(a),$$
$$\text{where } a = v_2 \cos(x) - v_3 \sin(x) \tag{3-3}$$

Here v_2 and v_3 are the vertical and horizontal vector components of the rotation vector and x is the direction in radians. The residuals obtained provided the data used to decide whether the trial should be discarded.

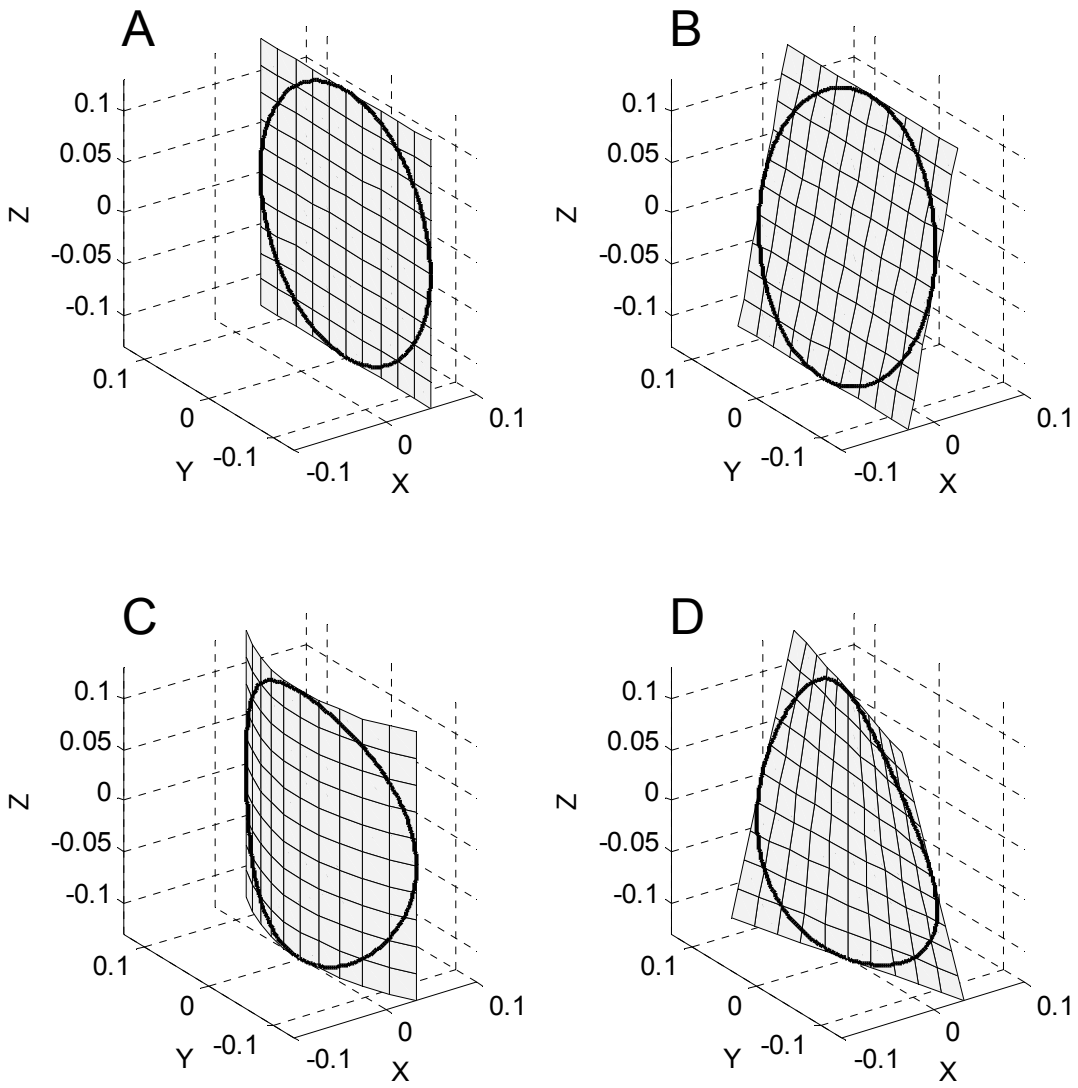

Figure 3-1. Examples of the four main shapes of a second order surface fit.

A: The plane has an offset of 0.05 (α_1). *B*: A slope with a ratio of 0.2 in the Z-direction, i.e. horizontal direction sensitivity of torsion, (α_3). A Y-slope indicates vertical direction sensitivity (α_2). *C*: A curvature in the Y direction, i.e. vertical direction, with a factor (α_4) of 2. Curvature in the Z-direction (α_6) indicates horizontal direction sensitivity. *D*: A twist of the surface with a factor (α_5) of 2.

3.4 Results

3.4.1 Sinusoidal fit

The most conspicuous characteristic of the eye–head coordination during both the ‘circular fixation’ and smooth pursuit paradigm was the direction-specific contribution of the head. A representative example of one ’circular fixation‘ trial is illustrated in Figure 3-2.

The orientation vector end-points of the eye-on-torso (Et), illustrated by the roughly circular trace (dark gray in Figure 3-2A), shows the eye orientation relative to the torso that moved with the turn chair while the subject fixated the space-fixed target. This trace was typically not perfectly circle-shaped even if the target was fixated perfectly because of the parallax effect from the translating eye when the head moved and the finite distance of the target. Head-on-torso (Ht) and eye-in-head (Eh), illustrated in black and light gray respectively, show the relative direction specificity; head-on-torso extends more in the horizontal than the vertical direction and, as a consequence, eye-in-head extends more in the vertical than the horizontal direction. This was quantified by comparing the amplitudes of the first order sinusoidal fits of each of the horizontal and vertical components (Figure 3-2B). The standard deviations of all residuals of the fits were 0.66° and 0.74° for eye-on-torso horizontal and vertical components, respectively, for CF-trials and 0.41° and 0.40° for SP-trials. For head-on-torso the standard deviations were 2.37° and 1.88° for CF-trials and 1.97° and 1.74° for SP-trials, horizontal and vertical, respectively. For eye-in-head the standard deviations were 2.52° and 2.10° for CF-trials and 2.08° and 1.87° for SP-trials, horizontal and vertical, respectively.

The total number of successful trials recorded was 411 and 53 for circular fixation and smooth pursuit, respectively. The mean amplitudes of the fits of the horizontal and vertical components of head-on-torso data showed clear direction specificity for both the circular fixation and smooth pursuit trials (Figure 3-3). Each of the four subjects had significant higher mean horizontal than vertical

amplitudes when comparing the subject individually, but comparisons in between subjects showed high inter-subject variability (Figure 3-3A). E.g. Subject M1, who generally had small head contributions, had lower horizontal amplitudes than M3's vertical amplitudes.

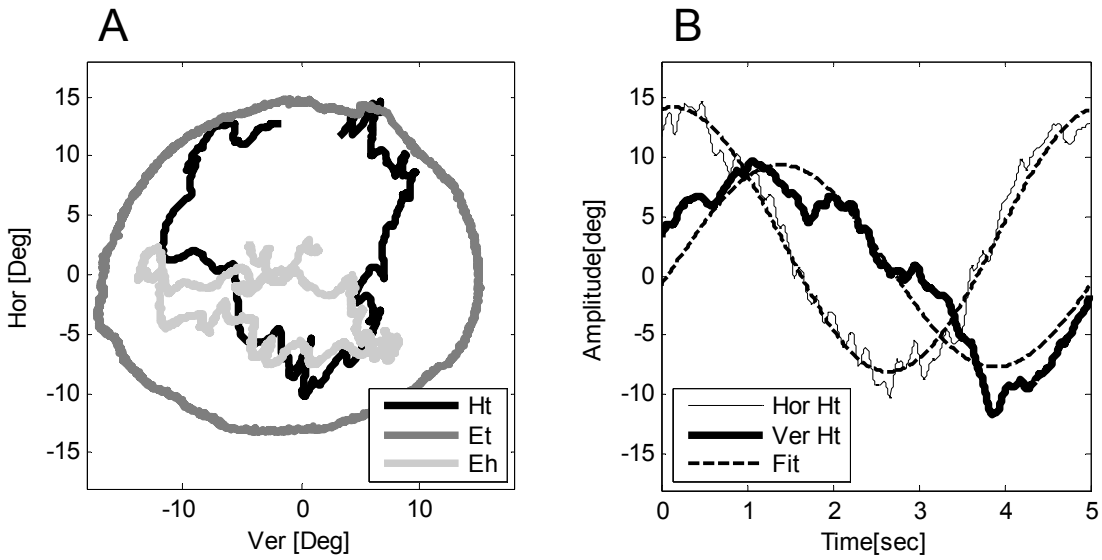

Figure 3-2. Example of one 'circular fixation' trial.

A: Orientation vector end-points for horizontal versus vertical directions for one 'Circular fixation' trial. Black denotes head orientation relative to torso (Ht), dark gray denotes eye relative to torso (Et) and light gray denotes eye relative to head orientation (Eh). *B*: Thin plot denotes horizontal component of Ht and the thick plot denotes the vertical component while the dashed denotes the sinusoidal fit of each of the components. Target frequency: 0.2 Hz. Subject: M3.

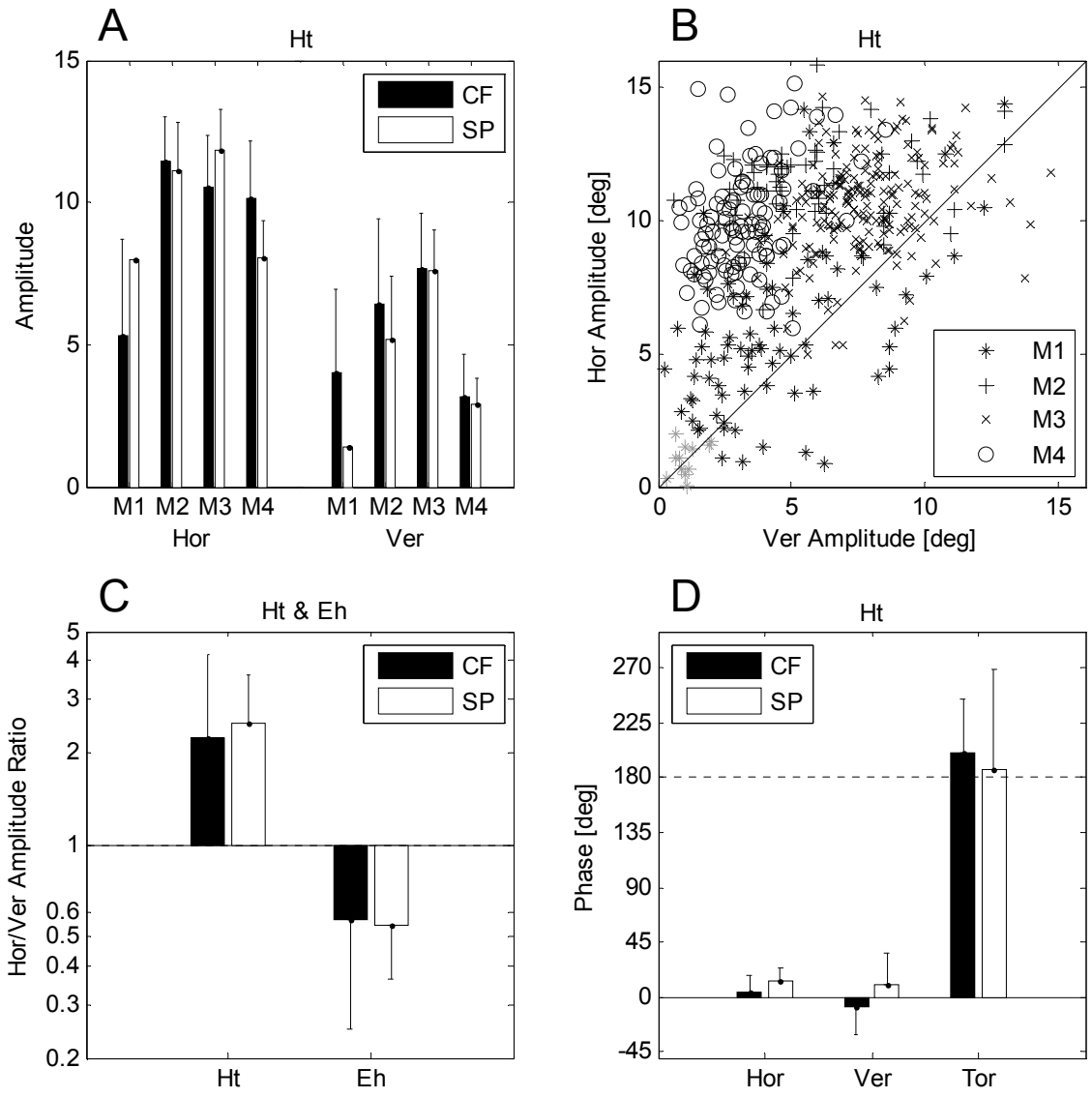

Figure 3-3. Sinusoidal fit data.

A and *B*: Horizontal and vertical amplitudes of the sinusoidal fit of head-on-torso. *A*: Mean amplitudes for each subject and trial type (CF and SP). *B*: Scatter plot of the amplitudes showing a mark for each trial with different mark types for each subject (CF and SP together). Trials not used for horizontal–vertical ratio evaluation are shown in gray *C*: Mean Horizontal/vertical gain ratio of Head-on-torso (Ht) and Eye-in-head (Eh). *D*: Phase of sinusoidal fits of Head-on-torso for horizontal, vertical and torsional components relative to the target. The torsional component is relative to the horizontal target component (positive phase means lag). Error bars are one standard deviation.

Furthermore we found a rather large intra-subject variability The subjects each performed a minimum of 7 trials for smooth pursuit and 29 trials for circular fixation except subject M1, from whom we had only one successful trial for smooth pursuit (no error bars for this trial in Figure 3-3A). The intra-subject variability in terms of the range of the smallest to the largest head contribution was 5.78°±3.02 and 9.74°±3.52 (mean ± std across subjects) for smooth pursuit and circular fixation, respectively.

Both the inter- and intra-subject variability can best be observed by plotting the horizontal and vertical amplitudes of the fits for each trial in a scatter plot with the horizontal component along the ordinate and the vertical component along the abscissa (Figure 3-3B). The marks that lie in the upper-left half of the plot will indicate trials that have higher horizontal than vertical amplitudes and marks in the lower-right half indicate trials that have higher vertical than horizontal amplitude. Although the amplitudes of the fits vary greatly (from almost zero to over the range of the target at 15°) more than 90% of all the trials had higher horizontal amplitude than vertical amplitude (410 out of 452). The mean horizontal to vertical amplitude ratio for the head-on-torso response component for all subjects were 2.24°±1.99 (mean ± std) and 2.51°±1.06 for circular fixation and smooth pursuit trials, respectively (Figure 3-3C). For eye-in-head the mean ratio is below 1 (0.56°±0.32 for CF and 0.55°± 0.18 for SP) indicating the inverse relationship of the eye-in-head and head-on-torso components. Both Ht and Eh ratios are significantly higher and lower than one, respectively ($P<0.001$, single-sided test). For each subject individually the ratio was also significant ($P<0.01$).

Subject M1 had a wide range of amplitudes from almost zero to almost full head tracking (15° amplitude) whereas subjects M2-M4 had smaller ranges of head contribution. Twelve out of 92 of the circular fixation trials performed by subject M1 were discarded in the ratio evaluation due to a very small head movement of less than 2° for *both* the horizontal and vertical response component (marked in gray in the lower left corner of Figure 3-3B). Like-wise, to avoid unreliable

results due to low amplitudes, trials were filtered out if they had amplitudes of less than 2° for *either* the horizontal, vertical or torsional component when evaluating the phase of the sinusoidal fits (Figure 3-3D).

Evaluation of the phase of the fit of the head-on-torso response component showed that the horizontal and vertical phase component were lagging relative to their respective target ditto for smooth pursuit trials, but for circular fixation trials the head was lagging for horizontal and leading for vertical (all $P<0.02$). The torsional head position was lagging about 180° behind horizontal target position, meaning that the head was tilting left-ear-down (LED) when looking left and right-ear-down (RED) when looking right (left and clockwise directions are positive).

3.4.2 Surface fit

A second order surface was fitted to the end-points of the rotation vectors for all trials for the head-on-torso (Ht), eye-on-torso (Et) and eye-in-head (Eh) response components. An example of such a fit is illustrated in Figure 3-4.

The main advantage of this analysis is that it reveals quantitatively how well and in which way the data conforms to Donders' law. That is, it shows how close the data lie to a surface and what the shape of this surface is. Even though we recorded and analyzed the data from all three response components (Ht, Et and Eh) our main reason for the surface fit analysis was to evaluate the head-on-torso behavior. According to data presented earlier by others the head-on-torso orientation for gaze directions with the body upright (i.e. SP trials), should conform to Donders' law and form a plane for the small range measured (Straumann et al., 1991; Tweed & Vilis, 1992). Alternatively, a Fick-like shape (twist) of the surface earlier reported for large head movements might be expected also for small head movements if the amount of data was large enough. The analysis of our data showed no significant twist of the surface fits of the SP trials (Figure 3-5A). This could be due to one of two possibilities: (1) the head

does in fact move in Listing's plane (workspace hypothesis) or (2) the Fick-like hypothesis also holds for this range but the measured range was too small to reveal any twist. To discriminate between these two possibilities we need to look at the results of the CF trials. Since the turn chair moved the torso of the subject like a Fick gimbal during these trials, the head would have to move like a Helmholtz gimbal if to be stable in space with the interocular axis kept horizontal (Figure 3-6). If, on the other hand, the range recorded was too small to show a twist of the surface like a Helmholtz gimbal the fits of the CF trials also would show insignificant results similar to those of the SP trials. Interestingly, the result of the analysis of CF trials revealed a significant twist with a positive coefficient (median=1.32), indicating a Helmholtz-like movement (Figure 3-5A). This finding suggests that the range recorded is in fact enough to reveal a twist of the fitted surfaces also for SP trials (if there is any) since the range of head movements was the same in both CF and SP trials (Figure 3-3A).

As shown in Eq. (3-1) a positive twist coefficient means that the two quadrants where the y- and z-components of the rotation vector both are positive or both are negative will give a positive x-component and the other two quadrants will have more negative x-components. Thus, the orientations where the head (or eye) is turned left and down or right and up will have a clockwise roll component and vice versa for the other two quadrants. This behavior is similar to that of a Helmholtz gimbal.

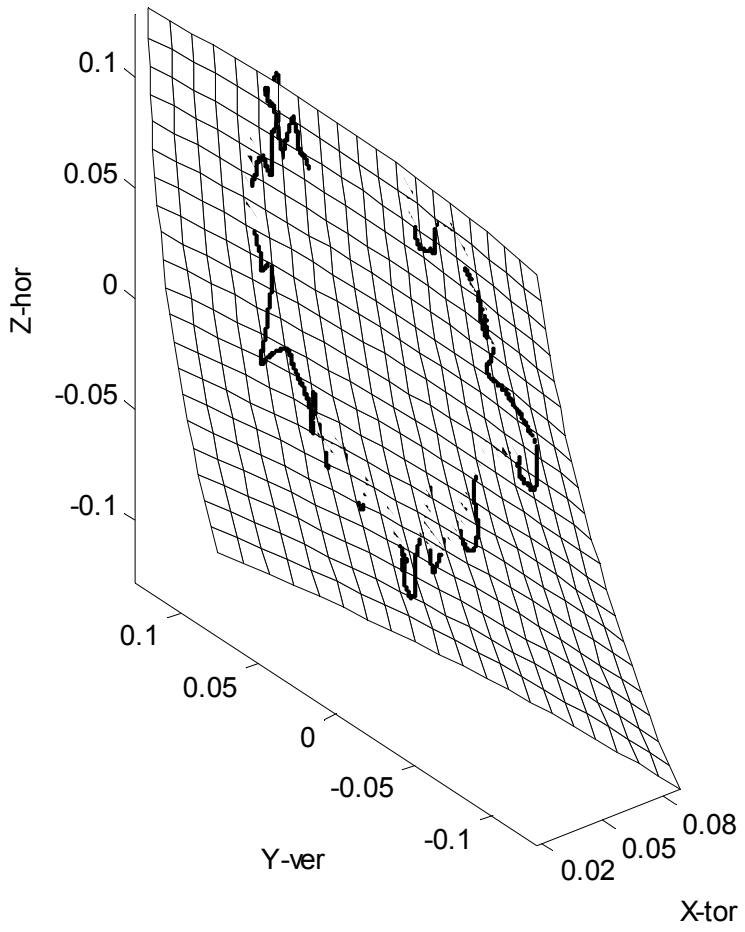

Figure 3-4. Surface fit of one trial of head-on-torso during circular fixation.

The surface is dominated by a tilt in the Z-direction (horizontal) and a twist with a positive coefficient. These characteristics are quantified by the coefficients $\alpha_1 - \alpha_6$ of Eq. (3-1): α_1(offset)=0.046, α_2(Y-slope)=-0.047, α_3(Z-slope)=-0.202, α_4(Y-curve)=-0.443, α_5(twist)=0.547 and α_6(Z-curve)=0.486. Data from subject M3.

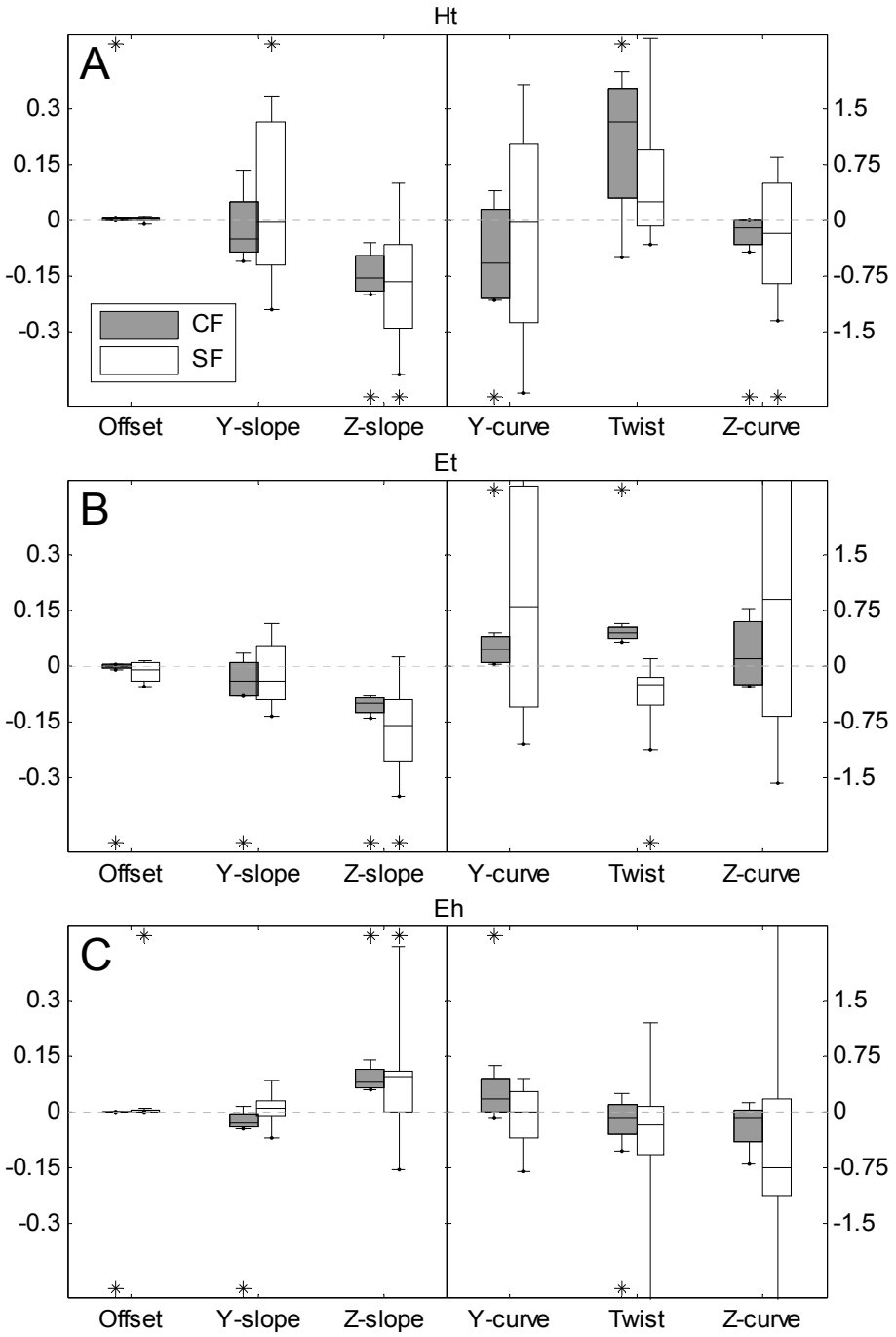

Figure 3-5. Box plots showing the six coefficients for fitted surfaces.

A: head-on-torso (Ht), *B*: eye-on-torso (Et), *C*: eye-in-head (Eh). The asterisk (*) are marked where the data is significantly biased above or below zero ($P<0.05$). Data based on the means of all trials for each subject for each the two protocols. The twist coefficient is zero if the fit is a Listing's plane, –1 if the surface is like a Fick-gimbal and +1 if the surface is like a Helmholtz-gimbal.

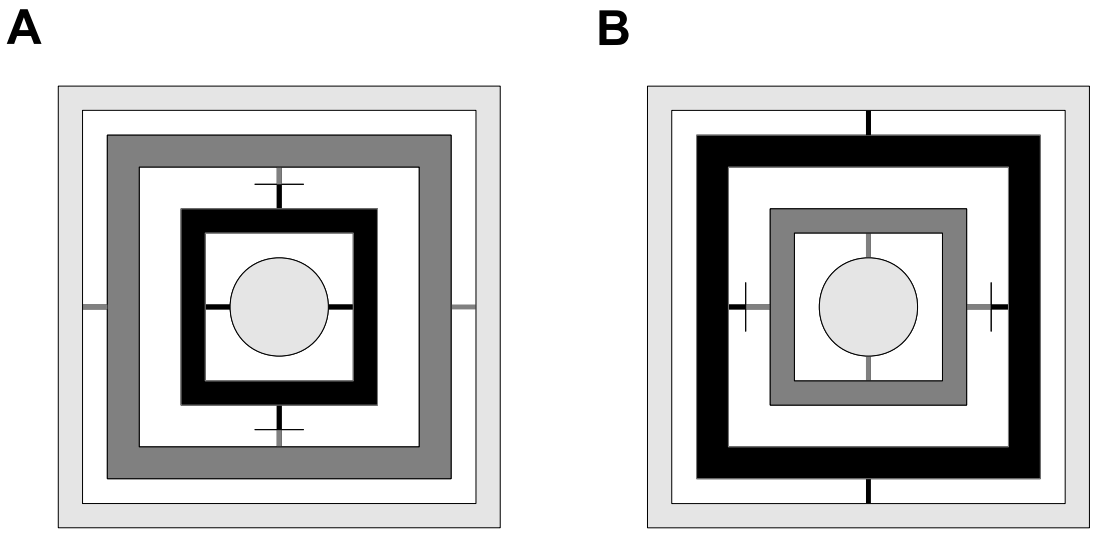

Figure 3-6. Fick- and Helmholtz gimbals compensate each other

The Helmholtz gimbal (dark gray) has an outer *horizontal* axis and an inner *vertical* axis while a Fick gimbal (black) has an outer *vertical* axis and an inner *horizontal* axis. *A*: The rotations mediated by the outer Helmholtz gimbal can be compensated by those of an inner Fick gimbal such that the subject's orientation (circle) remains stable in space. *B*: Similarly, an outer Fick gimbal can compensate rotations mediated by a nested inner Helmholtz gimbal.

The surface fits for both SP trials and CF trials showed also a rather large negative Z-slope which corresponds to horizontal direction. This matches the 180° phase shift of the sinusoidal fit of the torsional component (Figure 3-3D) since a negative Z-slope provides inverse relationship between the horizontal and torsional components (a direct relationship would give zero phase shift and a positive Z-slope). The median for the head-on-torso response component was -0.159 for CF trials and -0.167 for SP trials. For comparison a Z-slope of -0.15 would mean that the head rolls circa 2.25° with right-ear-down for a horizontal head orientation of 15° to the right and circa 2.25° with left-ear-down for a head orientation of 15° to the left. The same trend was seen for the eye-on-torso albeit to a lesser extent with a median Z-slope of -0.101 for CF and -0.161 for SP but for eye-in-head the trend was reversed with a median Z-slope of 0.075 for CF

and 0.092 for SP. The slope in Y-direction was either not significant or very small compared to the slope in the Z-direction.

The other two second order components, besides the twist component, showed a significant bias of the Y-curve for head-on-torso movements only for CF with median coefficients of -0.59 and a significant Z-curve for both CF and SP, although relatively small. Notice that these coefficients are of second order and thus equal to the square of the respective vector component meaning that a Z-curve of 1 would mean that the head was rolled circa 2° right-ear-down at head orientations of either 15° left or right. This is also the reason why the scales in Figure 3-5 are different for first and second order coefficients.

The second order components for eye-on-torso and eye-in-head movements were either not significantly biased or only with a relatively small median.

The offsets for head-on-torso, eye-on-torso and eye-in-head movement components were generally small and highly dependent on the position of the calibration and therefore not physiologically interesting even if a significant bias is shown.

To determine how well the rotation vector end-points were limited to a surface we evaluated the standard deviation of the sampling points relative to the fitted surface in the torsional direction. This provides a measure of the 'thickness' of the surface and thus a qualitative measure of how well Donders' law was obeyed. The median standard deviation for the head-on-torso movement component was 0.97° of CF trials and 0.71° for SP trials across all subjects. For the eye-on-torso movement component the standard deviation was somewhat lower at 0.54° for CF trials and 0.52 for SP trials. The standard deviation for eye-in-head was 0.89° for CF trials and 0.65° for SP trials.

3.5 Discussion

Eye–head coordination

In both paradigms, we found that the head had a clear preference for moving in the horizontal direction whereas the eye, conversely, rotated more in the vertical direction. We quantified these preferences in the eye–head coordination by a sinusoidal fit analysis. Although generally not on a quantified basis, a segregation into horizontal and vertical direction-specific eye and head contributions has been reported in numerous previous studies for large eye–head saccades over ranges where the head was forced to contribute due to the limited oculomotor range (see e.g. Glenn & Vilis, 1992; Radau et al., 1994; Ceylan, Henriques, Tweed & Crawford, 2000). In our study we show and quantify that the same direction specificity holds for eye–head movements even in the periprimary range where the head contribution is optional. This observation supports the notion that the oculomotor and head–neck motor system share higher level commands found both in the superior colliculus of the midbrain and the supplementary- and frontal eye fields of the cortex (see e.g. Klier, Wang & Crawford, 2001; Martinez-Trujillo, Wang & Crawford, 2003; Knight & Fuchs, 2007). We have shown that this direction specificity holds not only for changes in head orientation relative to space (SP-paradigm) but also for a head stabilization task where the orientation of the torso was systematically disturbed during a target fixation paradigm (CF-paradigm). The ratio of eye to head contribution is roughly equal in both paradigms (see Figure 3-3C), which suggests that this ratio is somewhat fixed regardless of the effect of other factors such as gravity. The reluctance of performing head vertical movements during SP-tasks could be explained by either a dynamic (neural) energy conservation strategy optimizing movements within the gravitational field or a more static mechanism perhaps defined by the head–neck anatomy.

Since both paradigms showed an equal ratio of direction specificity despite the fact that only the CF-task encourages vertical head movement seen strictly from a gravity balance perspective, we conclude that the underlying strategy is more of a static nature.

Head orientation

The main objective of our spatial analysis was to try to discriminate between the workspace hypothesis and the Fick-like hypothesis for gaze control in the periprimary range. The outcome expected for each of the two hypotheses depends on the following two distinctive scenarios as summarized in Table 3-1: One is that the range of data points collected was too narrow to detect any curvature and the other is that the range of data was sufficient to detect curvature. If the range measured was too small to detect curvature both the SP- and CF-tasks for both hypotheses would either show Listing's plane-like data fits (LP) or the fit would be inconclusive due to biological noise (N/A). If however the range was sufficient to detect curvature one would expect to observe during the SP-tasks the Fick-like curvature if the Fick-like hypothesis holds and the LP-shaped data-fits if the workspace hypothesis holds. In contrast, during the CF-tasks one might expect either a Fick-like shape or a Helmholtz-like shape if the Fick-like hypothesis holds; Fick-like if the head orienting behavior is believed to be of a static or mechanical origin defined by head–neck anatomy and Helmholtz-like if the reason for Fick-like behavior is to keep the interocular axis horizontal relative to space, since Helmholtz-like behavior would reverse the disturbance of the Fick-gimbal movement produced by the turn chair during this task. The workspace hypothesis would likewise give preference to a Helmholtz-like behavior to compensate for the imposed passive rotation.

The results of the head-on-torso measurement show a clear tendency of Helmholtz-like behavior for CF-trials (Figure 3-5A) with a twist coefficient significantly larger than zero. The reason why the twist coefficient on average was more than 1 (the median was 1.32 ± 1.09) can be explained by the fact that

when the head contributes less than 100% a twist of more than 1 indicates that the roll of the head compensates more to keep the interocular axis aligned with space-horizontal than to direct the head towards the target. Thus, it does not indicate an over-compensation of head roll per-se.

Since the data shows a significant Helmholtz-like curvature in the head-on-torso movement component for CF-tasks, the range of data is apparently sufficient for detecting curvature. Furthermore, since the range of data covered in SP-tasks was similar (see Figure 3-3A) it is fair to assume that the curvature, if any, should have manifested itself also in the SP-tasks. However, the twist coefficients for the head-on-torso movement component shows no significant bias above or below zero and thus no indication of curvature for SP trials (Figure 3-5A). In fact, with a median twist coefficient of 0.23 for SP-trials, most of the trials showed more Helmholtz-like than Fick-like behavior which indicates that the Fick-like hypothesis is probably not true for small head movements during gaze control in the preprimary range. With a twist coefficient of 0.23 the surface is actually closer to Listing's plane than to the surface of a Fick-gimbal. One reason for this could be that, in order to constantly obey Donders' law, the optimal strategy is to follow Listing's law since movements in Listing's plane can be performed with fixed-axis rotations. This indicates that for small head movements the strategy for preserving the eyes leveled with horizontal is waived in favor of a more kinetically optimized strategy.

In our experiments we used smooth pursuit and fixation for changing the gaze direction relative to the subject while the Fick-like head orientation behavior, which was demonstrated by others, was observed for fixations made while making eye–head saccades between targets. Therefore, it could be argued that the reason why we do not see Fick-like behavior for our SP trials is because we used smooth pursuit to control the gaze and not saccades to various fixation points. However, it has been shown that the Fick-like behavior is not present during movement between fixation points (Crawford et al., 1999) or when head position (not gaze) is the primary task e.g. when wearing pinhole goggles or during head

fixations with a laser pointer helmet (Ceylan et al., 2000). In contrast, it seems that the Fick-like behavior is present whenever the head serves as a platform for gaze, which is also the case during smooth pursuit (i.e. for a large enough movement range). Furthermore the speeds of the targets were relatively slow during the SP trials (5 or 10 seconds per revolution) which in turn made the head movements so slow that they were below the threshold of the semicircular canal sensitivity (unlike head movements made during a typical large eye–head saccade).

It should be noted however, that the number of SP-trials (46) was considerably less than that of CF-trials (380) which made the median coefficients calculated less accurate for SP-trials. On the other hand, the evaluation of the 'thickness' of the surfaces showed rather low standard deviations even when compared to the small range of head movements indicating robust fits. Furthermore, the median standard deviation for SP trials was lower than that of the CF trials.

In addition to the Fick-like behavior, it has also been reported that the head, although to a lesser extent, tilts clockwise (CW) when heading right and counter-clockwise (CCW) when heading left during large eye–head saccades (Crawford et al., 1999; Ceylan et al., 2000). Unlike the Fick-like behavior, this tilting behavior was also seen in our experiments. This is manifested by the negative Z-slope (coefficient a_3) of the fits for the head-on-torso movement component. Both paradigms show roughly the same amount of Z-slope, which is not surprising since the instantaneous conditions are the same for both paradigms when the target is directly to the right or left: the chair is upright and the target is either 15° to the right or left. But the purpose underlying for this behavior can not be explained from an energy conservation perspective. By tilting the head weight is displaced in much the same way in both paradigms. It can also not be explained by a strategy that aims at keeping the eyes leveled with the horizontal, since a tilt counteracts this purpose. One explanation could be that this is simply the most suitable way for turning the head due to the anatomical layout.

We conclude that the Fick-like strategy seen for large head movements is not the adequate description for small head movements that are present in a surprisingly consistent manner during gaze movement in the periprimary range. On the contrary, both the low twist coefficient observed during SP trials and the Helmholtz-twist during CP trials, favor the workspace hypothesis. Apart from the subtle head tilt, these different strategies must each apply dependent on the range of head movement performed by the subject. It would be interesting to investigate in a future study when and how the transition from one strategy to the other occurs when the animals do head movement over a large range of amplitudes. It could also be interesting to see how the head would orient during fixations of targets at random directions compared to a complimentary paradigm where a turn chair would move the subject to random orientations (fast) while fixating a stationary target.

	SP	CF
Range too small to detect curvature		
Fick-like hypothesis	LP or N/A	LP or N/A
Workspace hypothesis	LP or N/A	LP or N/A
Range large enough to detect curvature		
Fick-like hypothesis	Fick-like	Fick-like or Helmholtz
Workspace hypothesis	LP	Helmholtz

Table 3-1. Table showing the expected outcome possibilities for the twist coefficient for the two hypotheses.

If the range of data is too narrow to detect curvature no significant bias is expected for the twist coefficient. If the range covered is sufficient it is expected that the Fick-like hypothesis would show Fick-like curvature for SP-trials and Fick-like or Helmholtz-like curvature for CF-trials – depending on the underlying cause for the Fick-like strategy. If the range is sufficient and the head orienting behavior is better described by the workspace hypothesis, the SP trials would show Listing's plane behavior and Helmholtz-like behavior during CF-trials.

4. Conclusions and Outlook

The central motivation for the research presented in this thesis was to gain knowledge of how the brain controls head orientation in order to direct gaze. Whereas the extraocular muscles serve as a fast and precise mechanism to control the orientation of the eyes relative to the head, the head serves in this context as a platform or reference frame for this apparatus. When directing the gaze to a new visual target the eyes move fast to quickly direct the fovea on the target while the head usually takes part with a much slower movement in order to keep the orientation of the eyes relative to the head directed approximately forward. In addition to this, the platform of the head, the chest, might also contribute to the overall gaze shift.

To stay updated about these movements the brain receives visual cues and somatosensory inputs in addition to signals from the vestibular system. A major challenge of the brain is to process these different sensory inputs and creating an internal model of self-orientation and to provide appropriate responses in order to control gaze. One strategy of motor control is to reduce to number of dimensions from three to two dimensions. This is done for eye movements by obeying Listing's law whereas head movements are known to obey Donders' law (Donders' law can be implemented in many ways while Listing's law is just one particular implementation of Donders' law).

By discovering how the brain chooses to implement Donders' law for head orientation under various sensory input it was possible to reveal some of the mechanisms underlying the motor control of the head and to enlighten, in combination with gaze control, the relative priorities between eye and head movements.

These behavioral strategies are important to disclose and to further the understanding of how eye and head movements are implemented in the brain. It can therefore also contribute to the understanding of the pathology of the ocular and head orienting mechanisms. For example, patients with lower brain stem

infarctions may show deviations of the subjective visual vertical (Brodsky, Donahue, Vaphiades & Brandt, 2006), transient upside-down of vision (Malis & Guyot, 2003) or torticollis (Munchau & Bronstein, 2001; Klier, Wang, Constantin & Crawford, 2002).

In addition to these findings a novel method of measuring eye and head movements has been developed. Whereas research in eye–head coordination used to be limited to stationary laboratories with large frame coils, the method presented in this dissertation has made the standard vestibular turn chairs and motion platforms available for such research. This way eye–head coordination can now be studied under various translational and rotational stimuli of body orientation in a new subfield of eye–head coordination research.

Appendix A*

A.1 Search coil signal demodulation using three primary fields

For the primary field generated in the x-direction, we denote the magnetic field vector calculated at point *P* by the function (superscript "*T*" stands for transpose):

$$\vec{u}(P) = [u_1, u_2, u_3]^T \tag{A-1}$$

Similarly, for the primary field generated in the *y*-direction:

$$\vec{v}(P) = [v_1, v_2, v_3]^T \tag{A-2}$$

And the field generated *z*-direction:

$$\vec{w}(P) = [w_1, w_2, w_3]^T \tag{A-3}$$

For simplicity we summarize these three functions in a matrix, called Biot-Savart matrix, as follows:

$$[M_{BS}]_P = [\vec{u}, \vec{v}, \vec{w}]^T{}_P \tag{A-4}$$

Consider now a search coil, called *direction coil*, with a sensitivity vector $\vec{d} = [d_1, d_2, d_3]^T$ (orthogonal to the plane spanned by the coil) at position *P* in the external field (Figure 2-2) which describes the coils direction relative to the field frame. The induced current output $\vec{D}(P,E) = [d_u, d_v, d_w]_{P,E}$ of this coil is a function of its position $P = [x_P, y_P, z_P]$ in the magnetic field and can be

* This section has been published as: Thomassen J.S., Benedetto G.D. & Hess B.J. (2010). *Vision Res.*, 80 (13), 1203-1213.

described by the dot product of the sensitivity vector and the magnetic field vector for each field:

$$\begin{aligned} d_u(P,E) &= \vec{d}(E) \bullet \vec{u}(P) \\ d_v(P,E) &= \vec{d}(E) \bullet \vec{v}(P) \\ d_w(P,E) &= \vec{d}(E) \bullet \vec{w}(P) \end{aligned} \tag{A-5}$$

The dummy variable "*E*" in these equations indicates that the direction of the sensitivity vector $\vec{d}$ in the field in fact depends on eye position because the direction coil is supposed to be firmly fixed to the eye. Together with a second search coil, it is possible to describe the orientation (*E*) of the eye relative to the field frame. Thus, to measure 3D orientation of the eye we need information from a second search coil, which must be fixed to the eye ball such that the two coil vectors span a plane. The optimal orientation of the second search coil, called *torsion coil*, with sensitivity vector $\vec{t} = [t_1, t_2, t_3]^T$ is in a plane perpendicular to the first one. The output signal $\vec{T}(P,E) = [t_u, t_v, t_w]_{P,E}$ of the torsion coil can likewise be written as functions of the direction and position of the coil in the external field:

$$\begin{aligned} t_u(P,E) &= \vec{t}(E) \bullet \vec{u}(P) \\ t_v(P,E) &= \vec{t}(E) \bullet \vec{v}(P) \\ t_w(P,E) &= \vec{t}(E) \bullet \vec{w}(P) \end{aligned} \tag{A-6}$$

The set of equations in (A-5) and (A-6) is a system of linear equations for the vectors $\vec{d}(E)$ and $\vec{t}(E)$. Summarizing the functions $\vec{u}(P)$, $\vec{v}(P)$ and $\vec{w}(P)$ in the Biot-Savart matrix $[M_{BS}]_P$ we can write the solutions to (A-5) and (A-6) as:

$$\begin{aligned} \vec{d}(E) &= [M_{BS}]_P^{-1} \cdot \vec{D}(P,E) \\ \vec{t}(E) &= [M_{BS}]_P^{-1} \cdot \vec{T}(P,E) \end{aligned} \tag{A-7}$$

From these two coil sensitivity vectors we can calculate the rotation matrix as described in Section 3.2.2.

A.2 Demodulation of simulated 3D eye position measurements using three primary fields

Like for the two field evaluation the mean errors and standard deviations of three-field evaluation was increasing rapidly with distance from the center although the general error score was lower (compare thick lines in Figure 2-6 and Figure A-1). Small decreases in the mean error scores were also found for the Biot-Savart based demodulation and the one based on the experimentally measured magnetic field characteristics when compared with the two field evaluation.

The decrease of error scores for the Biot-Savart based corrected data when compared with the uncorrected data was significant for all groups ($P < 0.01$), except in the center position as expected ($P = 1$). The error scores at individual positions, without grouping, were also significantly improved, except for F1 and FL1.

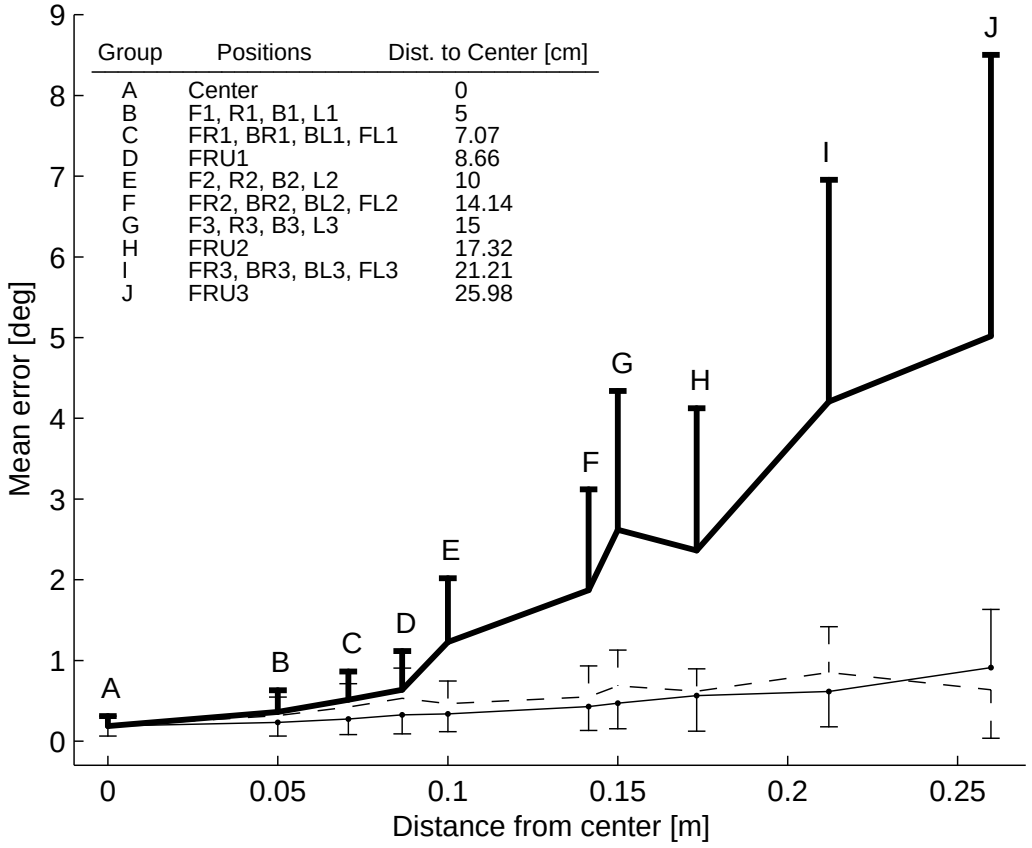

Figure A-1. Average demodulation error using three primary fields.

The thick curve shows the uncorrected demodulation, the thin solid curve shows Biot-Savart corrected demodulation and the dashed curve shows the errors when using the experimentally measured field characteristics.

A.3 Simulation of 3D eye position data during head-free gaze movements

This section describes the simulation of 3D eye position data used to verify the described Biot-Savart decoding algorithm and search coil demodulation procedure. The eye was simulated to be directed towards nine targets at locations forming a 3 × 3 matrix with equally spaced rows and columns (−20°, 0° and 20°). The head was simulated to be located in the center of the frame coils such that its yaw plane was parallel to the *x*–*y* plane of the field frame and the naso-occipital

axis intersected the central target (0°). The eye (dual search coil) was simulated to be located at $x = 4.5$ cm (forward positive) and $y = -1.5$ cm (left positive), corresponding roughly to the proportions of the rhesus monkeys used for the *in vivo* experiments. The gaze movements were simulated as random rotations of the head and eye such that the head contributed on average 80% of the gaze movement (normal distribution with $\mu_{head} = 0.8 \times$ target angle, standard deviation $\sigma_{head} = 10°$). We evaluated a total of 135 simulated fixations (15 fixations for each of the nine different target positions), for which the head contribution was used to determine the location of the eye and, accounting for parallax, calculated the gaze-on-target directions relative to a spherical screen with radius 88 cm, surrounding in its center the frame coils (see Matlab script in Appendix E.3). From the orientation and location of the eye we calculated the induced currents in the search coils as outlined in Figure A-2.

The orientation of the dual search coil relative to the eye was simulated with data from a calibration of a test coil where the relationship was defined by a rotation matrix. From this rotation matrix we derived the direction coil sensitivity vector from the first column which corresponds to the direction coil defined as a unit vector, multiplied by the sensitivity:

$$\vec{d} = \hat{d}\left|\vec{d}_{pre}\right| \tag{A-8}$$

The subscript "pre" indicates that in *in vivo* experiments the sensitivity is determined before the search coil is implanted as described in Section 3.2.5.
From the second column of the calibration rotation matrix, which is the normalized orthogonal component of the torsion coil sensitivity vector, we derived the vector as follows:

$$\vec{t} = \hat{t}\left|\vec{t}_{pre}\right| \text{ with}$$
$$\hat{t} = \left(\hat{t}^{\perp} + \hat{d} / \tan(\rho)\right) \Big/ \left|\hat{t}^{\perp} + \hat{d} / \tan(\rho)\right| \quad \text{(A-9)}$$

where ρ was the angle between the direction and torsion coil vector. The two vectors were then rotated as required to hit the target:

$$\vec{d}_{gaze} = R_{gaze}\ \vec{d}$$
$$\vec{t}_{gaze} = R_{gaze}\ \vec{t} \quad \text{(A-10)}$$

R_{gaze} is the rotation matrix describing the eye's orientation. The coil vectors were multiplied with the Biot-Savart matrix at the given field position:

$$\vec{d}_{BS} = M_{BS}\ \vec{d}_{gaze}$$
$$\vec{t}_{BS} = M_{BS}\ \vec{t}_{gaze} \quad \text{(A-11)}$$

from which the induced output current was derived after adding the offsets voltages:

$$\vec{d}_{out} = \vec{d}_{BS} + \vec{d}_{offset}$$
$$\vec{t}_{out} = \vec{t}_{BS} + \vec{t}_{offset} \quad \text{(A-12)}$$

The simulated output was then demodulated as described in Section 2.3.2 and the gaze direction was compared with the target position for accuracy.

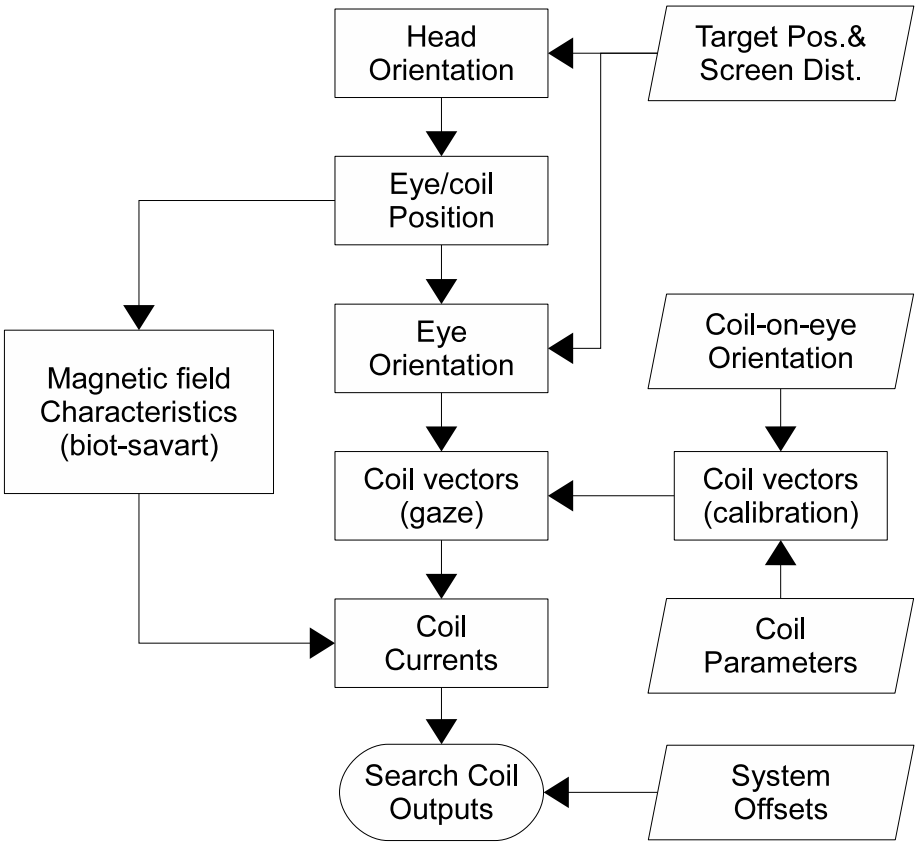

Figure A-2. Functional block diagram showing the algorithm used to simulate the current induced in the search coil.

The rhomboids denote input parameters and the rectangular boxes denote the algorithm.

A.4 Biot-Savart based demodulation of simulated eye–head movement recordings

We applied the same algorithm as used in the *in vivo* experiments to the simulated induced currents for calculating the gaze direction. Since the magnetic field calculations used in the simulation for the induced currents were the same as the ones for the reconstruction, the errors for corrected fixations were, as expected, very low (on average close to machine precision). The uncorrected fixations showed a mean error of $2.49 \pm 1.03°$ comparable to the ones found in the *in vivo* experiments. The gaze directions for corrected and uncorrected

fixations are shown along with the spatial location of the eye at the time of fixation in Figure A-3.

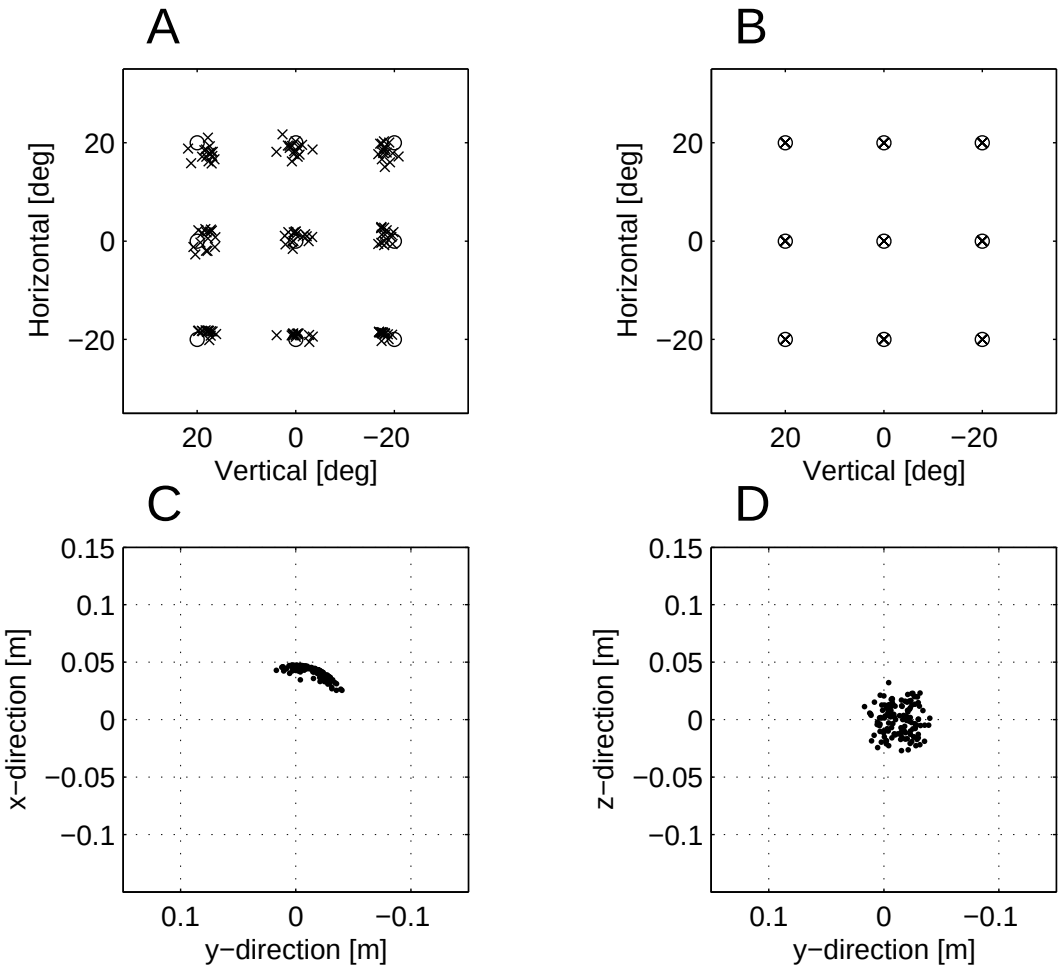

Figure A-3. Eye–head movement computer simulations.

Nine targets marked by circles and 135 fixations marked by crosses (simulated with 0.8 head–eye ratio and 10° std head rotation). *A*: Uncorrected fixations. *B*: Biot-Savart based corrected fixations. *C*: and *D*: Top-view and behind-view, respectively, of eye positions in the magnetic field at the time of the fixations.

A.5 Properties of the rotation vector

A rotation R in 3D space can be described by a 3×3 matrix, whose components are restricted by the requirement of orthogonally. Another way to express 3D

rotations is by exploiting the fact that any 3D rotation can be characterized by an axis or unity vector (which is in fact the real eigenvector of the associated rotation matrix) and a rotation angle (corresponding to the associated eigenvalue). Thus, a rotation vector is a vector ($\vec{r}$) that represents the axis of rotation and, by its length, the angle of rotation (Haustein, 1989). The polarity of the vector describes the direction of the rotation by the right hand rule (thumb of right hand pointing in direction of the vector and the fingers curl in the direction of the rotation). The rules of combining rotations require that the length of the rotation vector is set as the tangent of half the angle of rotation: $|\vec{r}| = \tan(\theta/2)$. The conversion between rotation matrix and rotation vector uses the fact that $\vec{r}$ is an eigenvector of *R*. With $\alpha = 1 + R_{11} + R_{22} + R_{33}$ one obtains $r_1 = (R_{32} - R_{23})/\alpha$, $r_2 = (R_{13} - R_{31})/\alpha$ and $r_3 = (R_{21} - R_{12})/\alpha$, where R_{ik} is defined as the matrix element in row "*i*" and column "*k*": $R_{ik} = [R]_{ik}$. The angle of rotation θ is defined by $\theta = \arccos((R_{11} + R_{22} + R_{33} - 1)/2)$.

Inverse rotations are obtained by taking the transpose of the rotation matrix $R^{-1} = R^T$ with $[R^T]_{ik} = [R]_{ki}$. As seen from the above relations, this translates into simply taking the negative rotation vector (r^{-1}=-*r*). It can be useful to combine consecutive rotations (Haustein, 1989; Hepp, 1990). For example, when calculating the eye orientation relative head orientation ($\vec{r}_{EH}$) when eye and head orientations are both recorded relative to the field frame (eye-in-space: $\vec{r}_{ES}$ and head-in-space: $\vec{r}_{HS}$, respectively):

$$\vec{r}_{EH} = \vec{r}_{HS}^{\,-1} \circ \vec{r}_{ES} = \frac{\vec{r}_{ES} - \vec{r}_{HS} + \vec{r}_{ES} \times \vec{r}_{HS}}{1 + \vec{r}_{ES} \bullet \vec{r}_{HS}} \qquad \text{(A-13)}$$

Appendix B – Third order surface fit

To test if the rotation vector end-points might be better described by higher order surface fits, we fitted a third order surface equation to the data by adding an additional four parameters to Eq. (3-1):

$$\begin{aligned} v_1 = {} & \alpha_1 + \alpha_2 v_2 + \alpha_3 v_3 + \alpha_4 (v_2)^2 + \alpha_5 v_2 v_3 + \alpha_6 (v_3)^2 \\ & + \alpha_7 (v_2)^3 + \alpha_8 (v_2)^2 v_3 + \alpha_9 v_2 (v_3)^2 + \alpha_{10} (v_3)^3 \end{aligned} \tag{B-1}$$

The four additional parameters describe two main shapes (Figure B-1): A cubic curvature in the horizontal (α_{10}) and vertical (α_7) directions and a quadratic curvature in the horizontal (α_9) and vertical (α_8) directions combined with a linear slope in the vertical and horizontal direction, respectively. By adding these additional parameters it was possible to reduce the mean standard deviation of the difference between the data and the fitted surface, also called the 'torsional thickness'. The fact that the standard deviation is reduced by fitting the data to a higher order surface is obvious and expected and is not by itself a reason to conclude that the behavior is better described this way (Schwarz, 1978). A higher order model will practically always provide better fits to data that has some degree of variance. To reduce the complexity of the analysis one should choose the model with the lowest possible number of parameters up to the point where higher order models would only give a relative small improvement. Previous studies of large eye–head movements have shown that while second order surface fitting provides large improvement over first order surface fitting, a third order surface only improves the fit little compared to the second order surface (Radau et al., 1994; Crawford et al., 1999). However, in contrast to these findings, this study shows a roughly equal improvement of the fits between first and second order compared to the improvement between second and third order surface fits (Figure B-2). However, in this study the range of head movements

was considerably smaller which could cause a relative greater variance of the parameters of the surface fits. Furthermore, each surface was fitted to the data from only one trial compared to a cloud of data, which means that the surface fits would easier adapt to the variance in head orientation when higher order surface fits were used (Figure B-3). In this light, we nevertheless consider a second order fit most appropriate to describe head orientation.

Another way of spotting this variance is to look at the coefficients which are sensitive to non-symmetrical behavior: while coefficients $\alpha_2, \alpha_3, \alpha_5, \alpha_7$ and α_{10} are sensitive to left-right mirror-symmetrical behavior (when looking right the head would have an equal amount but opposite torsion than when looking left), the coefficients α_1, α_4, α_6, α_8 and α_9 are all sensitive to non-symmetrical behavior. Consistent asymmetry around the midsagittal plane can not be explained by the anatomy and should not be considered natural and therefore these parameters can be seen as a measure of the level of variance.

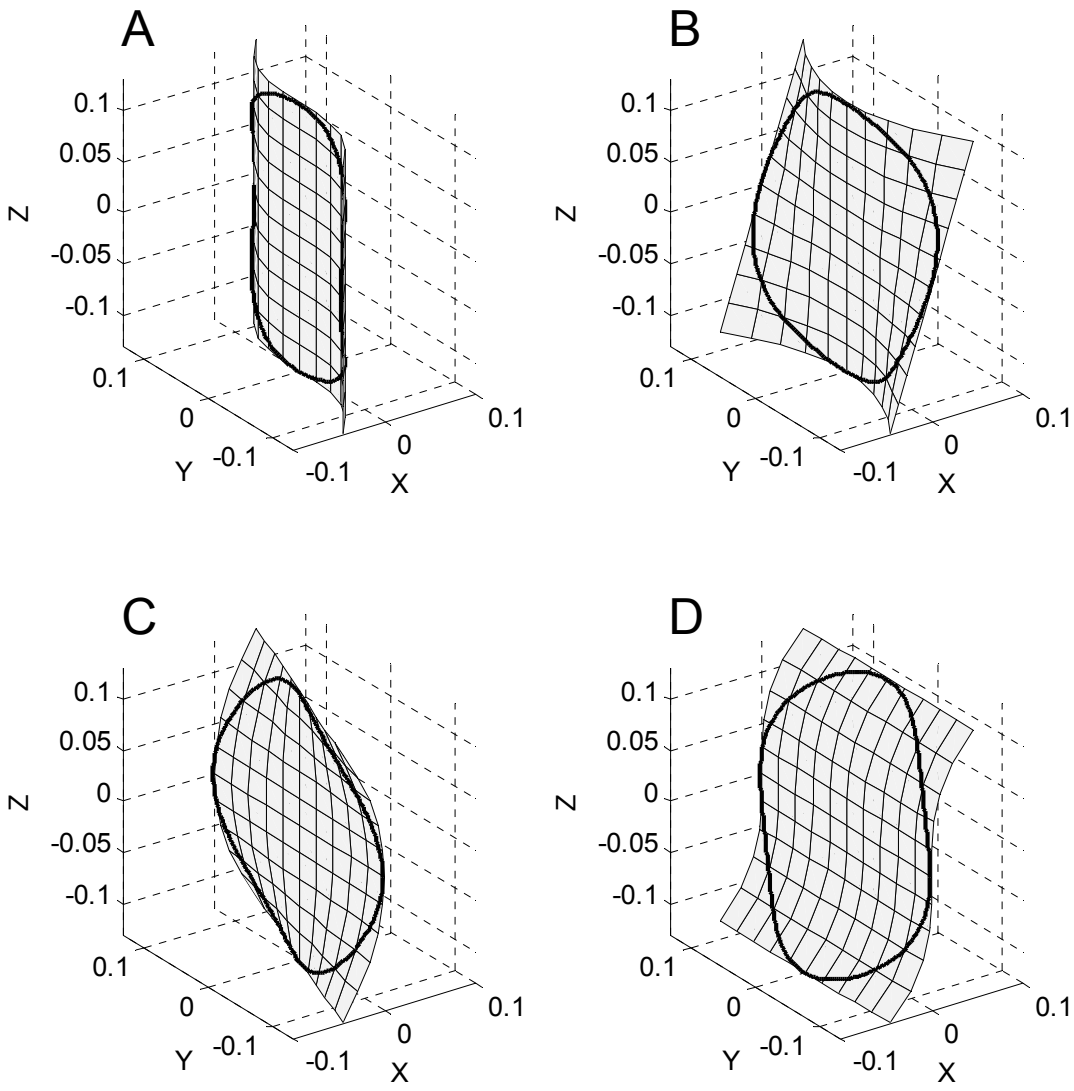

Figure B-1. Examples of the four third order shapes of surface fits.

A: The surface has a curvature (cubic) in the Y direction, i.e. vertical direction, with a factor (α_7) of 20. *B*: The surface has a curvature (quadratic) in the vertical direction combined with a linear slope in the horizontal direction with a factor (α_8) of 20. *C*: The corresponding shape of (*B*), defined by the coefficient α_9, has a horizontal curvature (quadratic) and vertical linear slope. *D*: The corresponding shape of (*A*), with curvature (cubic) in the Z direction defined by the coefficient α_{10}.

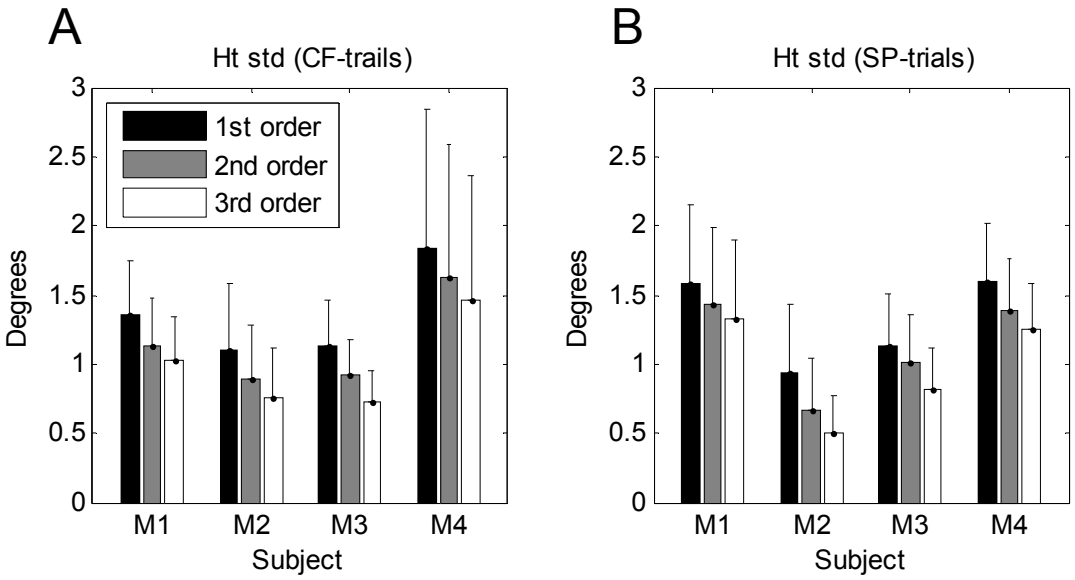

Figure B-2. Standard deviations of first, second and third order surface fits.

Mean standard deviations of first (black), second (gray), and third (white) order surface fits of Head-on-torso (Ht). Error bars are one standard deviation. *A*: Trials recorded during the 'circular fixation' (CF) paradigm. *B*: Trials recorded during the smooth pursuit (SP) paradigm.

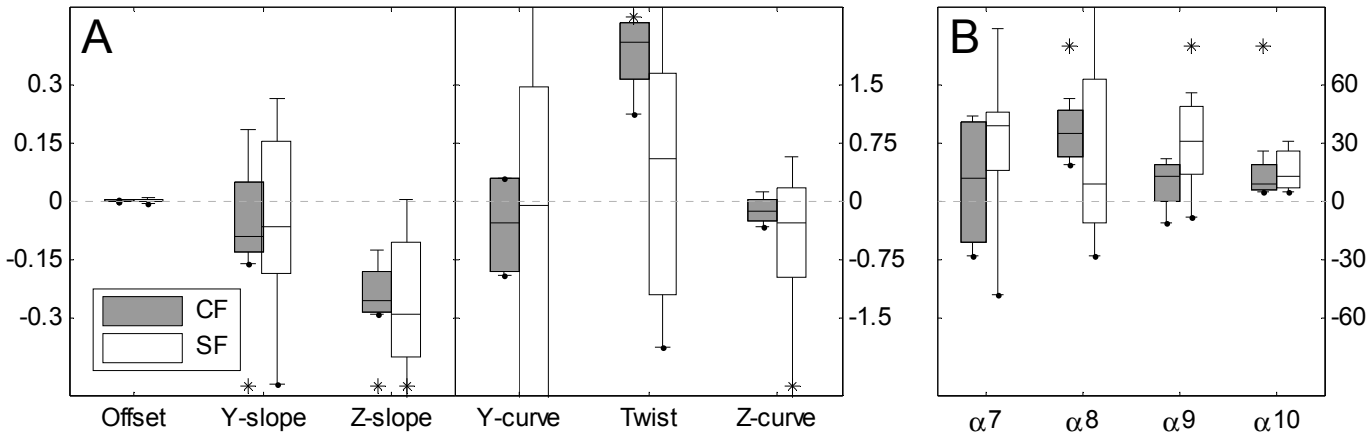

Figure B-3. Box plots showing the coefficients for third order fits surface fits of Head-on-torso.

A: The first six coefficients are similar to the coefficients of second order surface fits. *B*: The last four coefficients show the third order components of the fits.

Appendix C – Hardware overview

C.1 The turn chair setup

For both the *in vivo* experiments, verifying the decoding technique in Chapter 2 and the experiments in Chapter 3 a multi-axis turn chair was used (manufactured by Acutronic, Bubikon, Switzerland). Figure C-1 shows a photograph of the turn chair and its surrounding spherical screen. It has three servo-controlled gimbaled/nested motorized axes; the subject is placed inside a frame connected to the innermost axis (Axis 1) which rotates the subject in the yaw plane (see section 1.4 for a definition of reference frames). Axis 1 is placed within the middle axis (Axis 2) which rotates the subject in either the pitch- or roll plane depending on the position of Axis 1. Axis 2 is placed within the outer axis (Axis 3) which rotates the subject in either the yaw- pitch- or roll planes depending on the positions of Axis 1 and 2. A fourth axis (not shown in picture) is able to manually tilt Axis 3.

The surrounding spherical screen can rotate around a motorized axis aligned with Axis 3. The *in vivo* experiments described in Chapter 2 used visual stimuli in form of nine LEDs attached to the interior of this screen. The experiments involving smooth pursuit as described in Chapter 3 used a laser attached to the inner frame above the subject with galvanometer-controlled mirrors for redirection of the laser beam.

C.1.1 The eye tracker (Skalar system)

The frame coils, generating the primary magnetic field for eye movement recording (see description of the technique in section 1.6), is located inside Axis 1 of the turn chair with the head of the subject in the center (Eye Position Meter 3000, Skalar Instruments, Delft, The Netherlands). As opposed to a large frame surrounding the whole turn chair this small frame, of about 30 cm in side length, provides a magnetic field minimally affected by movement of the externally

rotating apparatus. The frame coils generate two primary alternating magnetic fields orthogonal in the center of the frame with the same frequency but with a 90° phase difference. See section 2.3 for further details about the Skalar system.

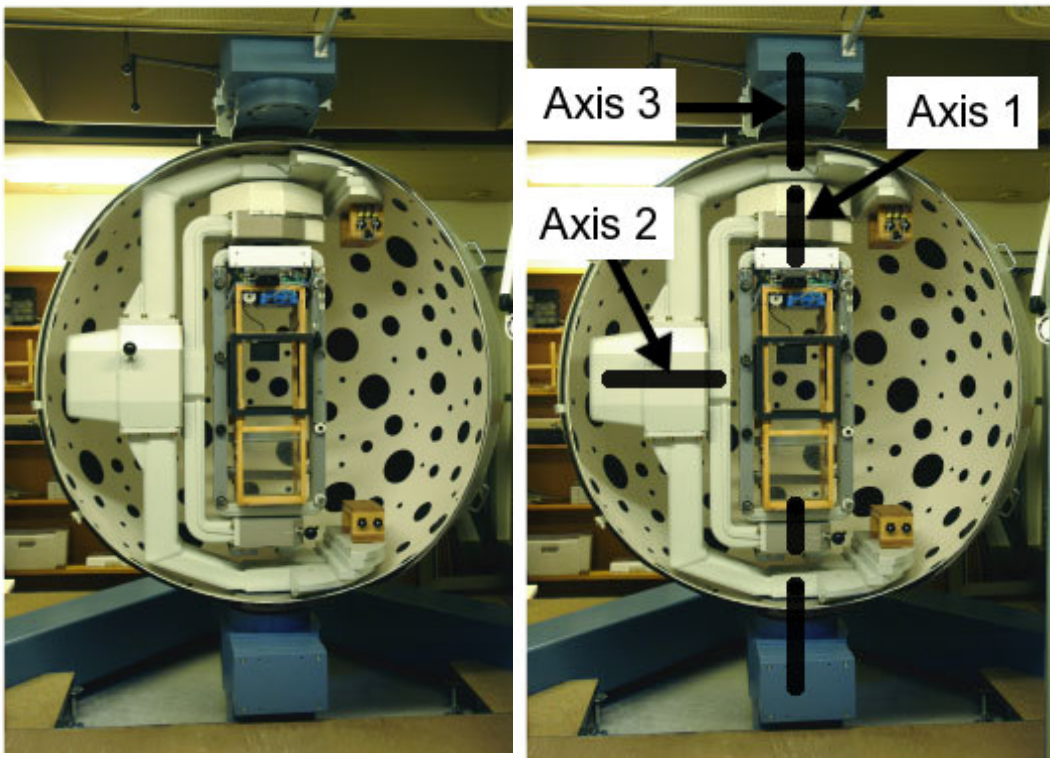

Figure C-1. The motorized multi-axis gimbaled turn chair.
The turn chair has three gimbaled motorized axes (labeled in the right-most picture) in addition to one manual axis for tilting the whole setup. The spherical screen exterior to Axis 1 and Axis 2 is likewise motorized and rotates independently around an axis aligned with Axis 3.

C.1.2 The head tracker (Zebris system)

The head tracker consists of four ultrasonic microphones, mounted directly above the frame coils of the Skalar system inside the inner frame of Axis 1, and three ultrasonic emitters placed on the head of the subject (CMS 20, Zebris Medical GmbH, Isny, Germany).
See section 2.3 for further details about the Zebris system.

C.2 The fixed chair setup

For the *in vitro* experiments verifying the decoding technique in Chapter 2 a fixed chair system was used. This system consists of a search coil eye tracker (Primelec), an optic head tracker (Optotrak) and a custom build gimbaled protractor. These three components are described in the following.

C.2.1 The eye tracker (Primelec system)

The eye tracker used for the simulation experiments in Chapter 2 was constructed with larger frame coils of approximately 75 cm (Angle-Meter NT, Primelec, Regensdorf, Switzerland). This enabled uncomplicated manipulation of the gimbaled protractor used for simulating eye movements. Figure C-2 shows a photograph of the system. The frame coils generates three primary alternating magnetic fields orthogonal in the center of the frame with different frequencies. See section 2.3 for further details about the Primelec system.

C.2.2 The head tracker (Optotrak system)

During the simulation experiment the gimbaled protractor was moved to different positions measured by an optical tracking system (OPTOTRAK 3020, Northern Digital, Canada). Three sensors mounted in the ceiling of the room detect the three dimensional position of infrared emitting diode markers mounted on the platform of the protractor. The system has a very high spatial accuracy (~0.1 mm) and is thus optimal for accurate positioning of the protractor. Six markers were mounted on the platform to ensure good measurements of both position and orientation.

C.2.3 The gimbaled protractor

A custom made gimbaled protractor was used to orient the search coil in the magnetic field (see Figure C-3). The outmost axis rotates around a vertical axis (horizontal movement). The middle axis, nested within the outer axis, rotates

around a forward pointing horizontal axis (torsional movement). The innermost axis, nested with the middle axis, rotates around a horizontal axis orthogonal to the outmost and the middle axis (vertical movement).

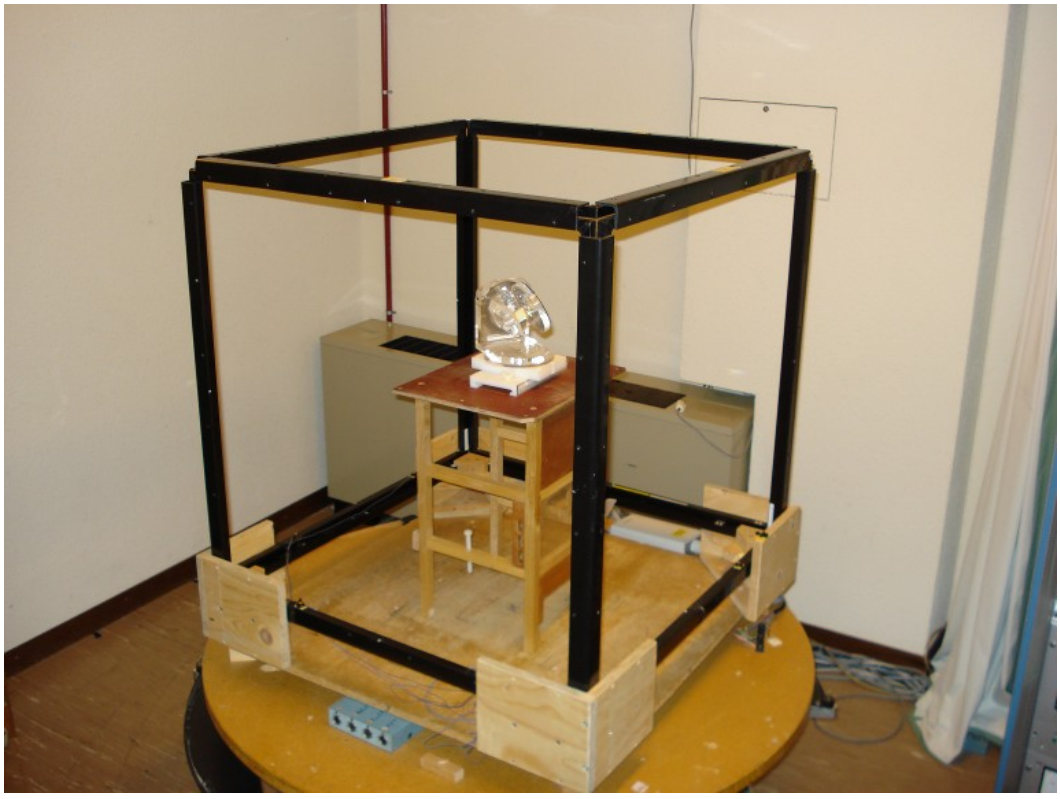

Figure C-2. The eye tracking system (Primelec) used in simulation experiments.
The frame coils with side length of 75 cm provide space for manipulation of the gimbaled protractor.

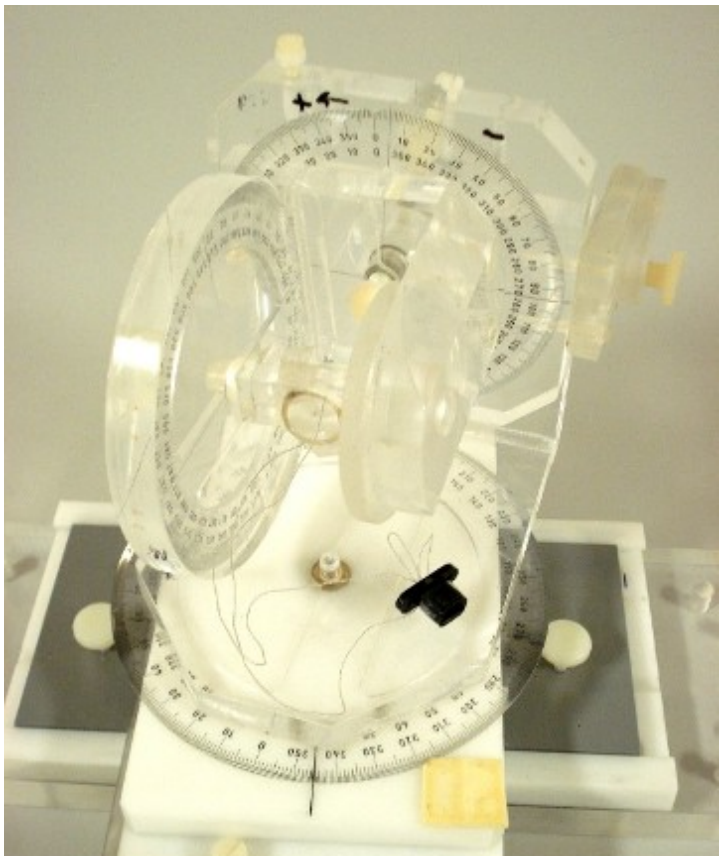

Figure C-3. Three-axis gimbaled protractor for accurate adjustment of orientation of the search coil.

Appendix D

D.1 Extraction of Fick- and Helmholtz angles from a rotation matrix

The Fick angles can be extracted from a rotation matrix by multiplying the corresponding sequence of basic rotation matrices (horizontal, vertical and then torsional):

$$R_{Fick} = R_{hor}(\theta_F)R_{ver}(\varphi_F)R_{tor}(\psi_F) = \begin{bmatrix} \cos(\theta_F) & -\sin(\theta_F) & 0 \\ \sin(\theta_F) & \cos(\theta_F) & 0 \\ 0 & 0 & 1 \end{bmatrix}\begin{bmatrix} \cos(\varphi_F) & 0 & \sin(\varphi_F) \\ 0 & 1 & 0 \\ -\sin(\varphi_F) & 0 & \cos(\varphi_F) \end{bmatrix}\begin{bmatrix} 1 & 0 & 0 \\ 0 & \cos(\psi_F) & -\sin(\psi_F) \\ 0 & \sin(\psi_F) & \cos(\psi_F) \end{bmatrix}$$

$$\Updownarrow$$

$$R_{Fick} = \begin{bmatrix} \cos(\theta_F)\cos(\varphi_F) & \cos(\theta_F)\sin(\varphi_F)\sin(\psi_F) - \sin(\theta_F)\cos(\psi_F) & \cos(\theta_F)\sin(\varphi_F)\cos(\psi_F) + \sin(\theta_F)\sin(\psi_F) \\ \sin(\theta_F)\cos(\varphi_F) & \sin(\theta_F)\sin(\varphi_F)\sin(\psi_F) + \cos(\theta_F)\cos(\psi_F) & \sin(\theta_F)\sin(\varphi_F)\sin(\psi_F) - \cos(\theta_F)\sin(\psi_F) \\ -\sin(\varphi_F) & \cos(\varphi_F)\sin(\psi_F) & \cos(\varphi_F)\cos(\psi_F) \end{bmatrix}$$

For the reverse transformation, the Fick angle θ_{Fick} (horizontal) can be obtained from the two-component arctangents (atan2) of R_{21} and R_{11}, where R_{ik} is defined as the matrix element in row "*i*" and column "*k*". The Fick angle φ_{Fick} (vertical) can easily be obtained $-\arcsin(R_{31})$, but this only hold for angles up to ±90°. For larger angles it is necessary to include a term that contains $\cos(\varphi_F)$ which can be done by taking the second component of atan2 as the square root of the sum of squared R_{21} and R_{11} with the first component as $-R_{31}$. The Fick angle ψ_{Fick} (torsional) can be obtained from R_{32} and R_{33} in the same way as θ_{Fick} was obtained.

$$R_{Helm} = R_{ver}(\varphi_H)R_{hor}(\theta_H)R_{tor}(\psi_H) = \begin{bmatrix} \cos(\varphi_H) & 0 & \sin(\varphi_H) \\ 0 & 1 & 0 \\ -\sin(\varphi_H) & 0 & \cos(\varphi_H) \end{bmatrix}\begin{bmatrix} \cos(\theta_H) & -\sin(\theta_H) & 0 \\ \sin(\theta_H) & \cos(\theta_H) & 0 \\ 0 & 0 & 1 \end{bmatrix}\begin{bmatrix} 1 & 0 & 0 \\ 0 & \cos(\psi_H) & -\sin(\psi_H) \\ 0 & \sin(\psi_H) & \cos(\psi_H) \end{bmatrix}$$

$$\Updownarrow$$

$$R_{Helm} = \begin{bmatrix} \cos(\theta_H)\cos(\varphi_H) & -\sin(\theta_H)\cos(\varphi_H)\cos(\psi_H) + \sin(\varphi_H)\sin(\psi_H) & \sin(\theta_H)\cos(\varphi_H)\sin(\psi_H) + \sin(\varphi_H)\cos(\psi_H) \\ \sin(\theta_H) & \cos(\theta_H)\cos(\psi_H) & -\cos(\theta_H)\sin(\psi_H) \\ -\cos(\theta_H)\sin(\varphi_H) & \sin(\theta_H)\sin(\varphi_H)\cos(\psi_H) + \cos(\varphi_H)\sin(\psi_H) & -\sin(\theta_H)\sin(\varphi_H)\sin(\psi_H) + \cos(\varphi_H)\cos(\psi_H) \end{bmatrix}$$

Similarly, the three Helmholtz angles can be obtained from R_{11}, R_{21}, R_{31}, R_{22} and R_{23}.

D.2 Gimbal lock

Since the Fick and Helmholtz angles are gimbaled rotations there are situations where two of the three gimbal axes align and the system is said to be in "gimbal lock". When this occurs the system loses a dimension and for a Fick gimbal it occurs exactly at 90° or –90° pitch and for a Helmholtz gimbal at 90° or –90° yaw. In this situation the inner and the outer axes are aligned and redundant. This problem is normally not an issue when using Fick- or Helmholtz angles for the measurement of head-fixed eye movements since the oculomotor range keeps the eye far from the gimbal lock positions, but for an unrestrained head it will be an issue, and especially for Helmholtz angles since the gimbal lock positions here are easily reachable for the gaze (±90° yaw).

When the position is at gimbal lock the second component in the atan2 calculation above will become zero and since the first term is divided by the second, it will not solve. A solution can be to check if the term is close to zero and in this case select the position of one of the two redundant axes and calculate the other with another component of the rotation matrix.

Appendix E – Matlab functions

E.1 Function to calculate the magnetic field (absolute)

```
function biot=biotmag(pos,frame,cur)
%BIOTMAG Magnetic field vector calculator
%   The function calculates the absolute magnetic
%   field in a rectangular frame.
%   Inputs:
%   pos   -> matrix with the dimension: 3xN, where N is the
%            number positions to calculate. First, second and
%            third rows are the positions in meters relative to
%            the forward pointing X-axis, the left pointing Y-
%            axis and the upward pointing Z-axis, respectively.
%            The origin is in the center of the frame.
%   frame -> Frame size in meters in the order: X,Y,Z.
%   cur   -> Current flow in amperes in each of the three coil
%            pairs.
%   Output:
%   biot  -> Matrix with the dimension: 3x3xN, where each row
%            consists of a three-point magnetic field vector for
%            each of the three magnetic fields (X,Y,Z).
%   JST 2008

%% Check if arguments are correct
if size(pos,1) == 3 && size(pos,2) ~= 3
    pos = pos';
end

if length(frame) ~= 3,
    frame(1:3) = frame(1);
    warning('Framesize set to cube'); %#ok<WNTAG>
end

%% define the 8 corners of the frame relative to center:
% the corners are numbered in the following order:
% frd,fld,flu,fru,brd,bld,blu,bru - 1 to 8
% f=front,b=back,l=left,r=right,u=up,d=down.
% with rows being corner number and columns being direction
% (x,y,z) the sign of the location relative to center is:
sign = [1 -1 -1; 1  1 -1; 1  1  1; 1 -1  1;...
       -1 -1 -1;-1  1 -1;-1  1  1;-1 -1  1];
cor = zeros(size(sign));
for i=1:8,
    for k=1:3,
        cor(i,k) = sign(i,k)*(frame(k)/2);
    end
end
```

```
%% define current flow (cf) for each field:

cf(1,:,:) = [1 2;2 3;3 4;4 1;5 6;6 7;7 8;8 5]; % X-field
cf(2,:,:) = [2 6;6 7;7 3;3 2;1 5;5 8;8 4;4 1]; % Y-field
cf(3,:,:) = [4 3;3 7;7 8;8 4;1 2;2 6;6 5;5 1]; % Z-field

%% define the "stick" vectors:
% Vector (a) is the stick vector aligned with the current flow.
% Vector (b) goes from pos to base of (a).
% Vector (c) goes from pos to the tip of (a).

b = zeros([3 size(pos,1)]);
c = zeros([3 size(pos,1)]);
biot(3,3,1:size(pos,1)) = 0;
for k=1:3, % fields
    for i=1:8, % sticks
        a = cor(cf(k,i,2),:)-cor(cf(k,i,1),:);
        for d=1:3, % directions
            b(d,:) = cor(cf(k,i,1),d)-pos(:,d);
            c(d,:) = cor(cf(k,i,2),d)-pos(:,d);
        end
        cross_ca(1,:) =  c(2,:).*a(3)-c(3,:).*a(2);
        cross_ca(2,:) =-(c(1,:).*a(3)-c(3,:).*a(1));
        cross_ca(3,:) =  c(1,:).*a(2)-c(2,:).*a(1);
        dot_ac = a(1).*c(1,:)+a(2).*c(2,:)+a(3).*c(3,:);
        dot_ab = a(1).*b(1,:)+a(2).*b(2,:)+a(3).*b(3,:);
        length_c = sqrt(sum(c(1:3,:).^2,1));
        length_b = sqrt(sum(b(1:3,:).^2,1));
        length_cross_ca = sqrt(sum(cross_ca(1:3,:).^2,1));
        biot(k,1,:) = squeeze(biot(k,1,:))' +
(cur(k)/(4*pi))*cross_ca(1,:)./((length_cross_ca).^2).*(dot_ac./(
length_c)-dot_ab./length_b);
        biot(k,2,:) = squeeze(biot(k,2,:))' +
(cur(k)/(4*pi))*cross_ca(2,:)./((length_cross_ca).^2).*(dot_ac./(
length_c)-dot_ab./length_b);
        biot(k,3,:) = squeeze(biot(k,3,:))' +
(cur(k)/(4*pi))*cross_ca(3,:)./((length_cross_ca).^2).*(dot_ac./(
length_c)-dot_ab./length_b);
    end
end
```

E.2 Function to calculate the magnetic field (relative)

```
function biot=biotmagnorm(pos,frame)
%BIOTMAGNORM Function to calculate the relative magnetic
%   field in a rectangular frame.
%   Calculates the Biot Savart matrix that describes the magnetic
%   fields at positions (pos) relative to the magnetic field at
%   the center.
%   JST 2008
```

```
%% calculate the magnetic field at the center
% for the given frame size and coil current
pos0(1:3) = 0;
cur = [1 1 1];
biot0 = biotmag(pos0,frame,cur);

%% calculate the magnetic field relative to the center
biot = biotmag(pos,frame,cur);

for i=1:3,
    if (abs(biot0(i,i)) ~= 0),
        for k=1:3,
            biot(k,i,:) = biot(k,i,:)/abs(biot0(i,i));
        end
    else
        biot(:,i,:) = biot(:,i,:)*0;
    end
end
```

E.3 Function to correct for parallax

```
function [newtgt]=h2c(pos,tgt,scrShape,scrDist)
%H2C  Function to correct for parallax
% Inputs:
% pos     -> New position relative to center (x,y and z)
% tgt     -> Target direction as seen from head position (pos)
%            given in horizontal and vertical Fick angles
%            (radians).
% scrShape-> Flat or sphere.
% scrDist -> Distance from ref. pos. (center).
% Output:
% newtgt  -> Target angles seen from ref. pos. (center) given in
%            horizontal and vertical Fick angles (radians).
%
%   Ex.:                            Screen
%     ----------------------------------------X----------------
%                                               -target
%
%                       X -pos
%
%
%                                  X -center
%

% convert from Fick angles to a Cartesian unit vector:
unit(:,1) = cos(tgt(:,1)).*cos(tgt(:,2));
unit(:,2) = sin(tgt(:,1)).*cos(tgt(:,2));
unit(:,3) = -sin(tgt(:,2));
```

```
if size(pos,1)==1 && size(pos,2)==3,
    % only one position given - use it for all calculations
    pos(1:size(unit,1),1) = pos(1,1);
    pos(1:size(unit,1),2) = pos(1,2);
    pos(1:size(unit,1),3) = pos(1,3);
end

if strcmp(scrShape,'sphere') % if screen is a sphere
    A = 1;
    B = 2*dot(pos',unit');
    C = dot(pos',pos')-scrDist^2;
    u(:,1) = (-B+sqrt(B.^2-4.*A.*C))./(2.*A);
    u(:,2) = (-B-sqrt(B.^2-4.*A.*C))./(2.*A);
    u(u(:,1)<0,1) = u(u(:,1)<0,2); %swap if first not positive
elseif strcmp(screenShape,'flat') % if screen is flat
    u = (scrDist-pos(:,1))./unit(:,1);
else
    error('choose flat or sphere screen shape')
end
tgtVec(:,1) = pos(:,1)+u(:,1).*unit(:,1);
tgtVec(:,2) = pos(:,2)+u(:,1).*unit(:,2);
tgtVec(:,3) = pos(:,3)+u(:,1).*unit(:,3);

% convert back from Cartesian unit vector to Fick angles:
ltgtVec = sqrt(tgtVec(:,1).^2+tgtVec(:,2).^2+tgtVec(:,3).^2);
tgtVec(:,1) = tgtVec(:,1)./ltgtVec;
tgtVec(:,2) = tgtVec(:,2)./ltgtVec;
tgtVec(:,3) = tgtVec(:,3)./ltgtVec;
newtgt(:,2) = -asin(tgtVec(:,3));
newtgt(:,1) = atan2(tgtVec(:,2),tgtVec(:,1));
newtgt(:,3) = zeros(size(newtgt(:,1)));
```

Appendix F – List of figures and tables

Appendix G – Abbreviations

Hor	Horizontal
Ver	Vertical
Tor	Torsional
VOR	Vestibular-Ocular Reflex
rVor	rotational Vestibular-Ocular Reflex
tVOR	translational Vestibular-Ocular Reflex
MSC	Magnetic Search Coil
3D	Three-dimensional
DOF	Degrees of Freedom
EOG	Electrooculography
Std	Standard deviation
Ht	Head-on-torso
Et	Eye-on-torso
Eh	Eye-in-head

5. References

Angelaki, D.E. (2004). Eyes on target: what neurons must do for the vestibuloocular reflex during linear motion. *J Neurophysiol, 92* (1), 20-35.

Angelaki, D.E., & Dickman, J.D. (2003). Premotor neurons encode torsional eye velocity during smooth-pursuit eye movements. *J Neurosci, 23* (7), 2971-2979.

Angelaki, D.E., & Hess, B.J. (2004). Control of eye orientation: where does the brain's role end and the muscle's begin? *Eur J Neurosci, 19* (1), 1-10.

Bahill, A.T., Clark, M.R., & Stark, L. (1975). The main sequence, a tool for studying human eye movements. *Mathematical Biosciences, 24* (3-4), 191-204.

Baloh, R.W., Sills, A.W., Kumley, W.E., & Honrubia, V. (1975). Quantitative measurement of saccade amplitude, duration, and velocity. *Neurology, 25* (11), 1065-1070.

Bartl, K., Siebold, C., Glasauer, S., Helmchen, C., & Buttner, U. (1996). A simplified calibration method for three-dimensional eye movement recordings using search-coils. *Vision Res, 36* (7), 997-1006.

Becker, W. (1989). The neurobiology of saccadic eye movements. Metrics. *Rev Oculomot Res, 3*, 13-67.

Bremen, P., Van der Willigen, R.F., & Van Opstal, A.J. (2007). Using double-magnetic induction to measure head-unrestrained gaze shifts. I. Theory and validation. *J Neurosci Methods, 160* (1), 75-84.

Brodsky, M.C., Donahue, S.P., Vaphiades, M., & Brandt, T. (2006). Skew deviation revisited. *Surv Ophthalmol, 51* (2), 105-128.

Cabungcal, J.H., Misslisch, H., Hepp, K., & Hess, B.J. (2002). Geometrical properties of three-dimensional binocular eye position in light sleep. *Vision Res, 42* (1), 89-98.

Cannon, S.C., & Robinson, D.A. (1987). Loss of the neural integrator of the oculomotor system from brain stem lesions in monkey. *J.Neurophysiol., 57* (5), 1383-1409.

Ceylan, M., Henriques, D.Y., Tweed, D.B., & Crawford, J.D. (2000). Task-dependent constraints in motor control: pinhole goggles make the head move like an eye. *J.Neurosci., 20* (7), 2719-2730.

Cohen, B., & Komatsuzaki, A. (1972). Eye movements induced by stimulation of the pontine reticular formation: evidence for integration in oculomotor pathways. *Exp Neurol, 36* (1), 101-117.

Collewijn, H. (1977). Eye- and head movements in freely moving rabbits. *J.Physiol (Lond), 266* (2), 471-498.

Collewijn, H., & Tamminga, E.P. (1984). Human smooth and saccadic eye movements during voluntary pursuit of different target motions on different backgrounds. *J Physiol, 351*, 217-250.

Collewijn, H., van der Steen, J., Ferman, L., & Jansen, T.C. (1985). Human ocular counterroll: assessment of static and dynamic properties from electromagnetic scleral coil recordings. *Exp.Brain Res., 59* (1), 185-196.

Coughlin, M.J., Cutmore, T.R., & Hine, T.J. (2004). Automated eye tracking system calibration using artificial neural networks. *Comput Methods Programs Biomed, 76* (3), 207-220.

Crane, B.T., & Demer, J.L. (1999). A linear canal-otolith interaction model to describe the human vestibulo-ocular reflex. *Biol Cybern, 81* (2), 109-118.

Crawford, J.D., Cadera, W., & Vilis, T. (1991). Generation of torsional and vertical eye position signals by the interstitial nucleus of Cajal. *Science, 252* (5012), 1551-1553.

Crawford, J.D., Ceylan, M.Z., Klier, E.M., & Guitton, D. (1999). Three-dimensional eye-head coordination during gaze saccades in the primate. *J Neurophysiol, 81* (4), 1760-1782.

Delabarre, E.B. (1898). A method of recording eye movements. *American Journal of Psychology, 9*, 572-574.

Demer, J.L., Miller, J.M., Poukens, V., Vinters, H.V., & Glasgow, B.J. (1995). Evidence for fibromuscular pulleys of the recti extraocular muscles. *Invest Ophthalmol Vis Sci, 36* (6), 1125-1136.

Ditterich, J., & Eggert, T. (2001). Improving the homogeneity of the magnetic field in the magnetic search coil technique. *IEEE Trans Biomed Eng, 48* (10), 1178-1185.

Dodge, R., & Cline, T.S. (1901). The angle velocity of eye movements. *Psychological Review, 8*, 145-157.

Donders, F.C. (1848). Beitrag zur lehre von den bewegungen des menschlichen auges. *Holländ Beitr Anat Physiol Wiss,* (1), 104-145.

Ferman, L., Collewijn, H., & van den Berg, A.V. (1987). A direct test of Listing's law--I. Human ocular torsion measured in static tertiary positions. *Vision Res, 27* (6), 929-938.

Fernandez, C., & Goldberg, J.M. (1971). Physiology of peripheral neurons innervating semicircular canals of the squirrel monkey. II. Response to sinusoidal stimulation and dynamics of peripheral vestibular system. *J Neurophysiol, 34* (4), 661-675.

Fernandez, C., & Goldberg, J.M. (1976). Physiology of peripheral neurons innervating otolith organs of the squirrel monkey. III. Response dynamics. *J Neurophysiol, 39* (5), 996-1008.

Fischer, B., & Boch, R. (1983). Saccadic eye movements after extremely short reaction times in the monkey. *Brain Res, 260* (1), 21-26.

Freedman, E.G. (2008). Coordination of the eyes and head during visual orienting. *Exp Brain Res, 190* (4), 369-387.

Freedman, E.G., & Cecala, A.L. (2008). Oblique gaze shifts: head movements reveal new aspects of component coupling. *Prog Brain Res, 171*, 323-330.

Freedman, E.G., & Sparks, D.L. (1997). Eye-head coordination during head-unrestrained gaze shifts in rhesus monkeys. *J Neurophysiol, 77* (5), 2328-2348.

Fuchs, A.F., & Robinson, D.A. (1966). A method for measuring horizontal and vertical eye movement chronically in the monkey. *J Appl Physiol, 21* (3), 1068-1070.

Fukushima, K. (1991). The interstitial nucleus of Cajal in the midbrain reticular formation and vertical eye movement. *Neurosci.Res, 10* (3), 159-187.

Ghasia, F.F., & Angelaki, D.E. (2005). Do motoneurons encode the noncommutativity of ocular rotations? *Neuron, 47* (2), 281-293.

Glenn, B., & Vilis, T. (1992). Violations of Listing's law after large eye and head gaze shifts. *J Neurophysiol, 68* (1), 309-318.

Goossens, H.H., & Van Opstal, A.J. (1997). Human eye-head coordination in two dimensions under different sensorimotor conditions. *Exp Brain Res, 114* (3), 542-560.

Grant, W. (1999). Vestibular Mechanics. In: *The Biomedical Engineering Handbook, Second Edition. 2 Volume Set,* null (CRC Press.

Grossman, G.E., Leigh, R.J., Abel, L.A., Lanska, D.J., & Thurston, S.E. (1988). Frequency and velocity of rotational head perturbations during locomotion. *Exp Brain Res, 70* (3), 470-476.

Guitton, D., & Volle, M. (1987). Gaze control in humans: eye-head coordination during orienting movements to targets within and beyond the oculomotor range. *J Neurophysiol, 58* (3), 427-459.

Hamilton, W.R. (1899). Elements of quaternions. Cambridge, UK: Cambridge University Press.

Haslwanter, T. (1995). Mathematics of three-dimensional eye rotations. *Vision Res, 35* (12), 1727-1739.

Haslwanter, T., Straumann, D., Hepp, K., Hess, B.J., & Henn, V. (1991). Smooth pursuit eye movements obey Listing's law in the monkey. *Exp Brain Res, 87* (2), 470-472.

Haslwanter, T., Straumann, D., Hess, B.J., & Henn, V. (1992). Static roll and pitch in the monkey: shift and rotation of Listing's plane. *Vision Res, 32* (7), 1341-1348.

Haus, H.A., & Melcher, J.R. (1989). Electromagnetic Fields and Energy. Englewood Cliffs, NJ: Prentice Hall.

Haustein, W. (1989). Considerations on Listing's Law and the primary position by means of a matrix description of eye position control. *Biol.Cybern., 60* (6), 411-420.

Hepp, K. (1990). On listing's law. *Commun.Math.Phys, 132*, 285-292.

Hess, B.J. (1990). Dual-search coil for measuring 3-dimensional eye movements in experimental animals. *Vision Res, 30* (4), 597-602.

Hess, B.J. (2008). Control of ocular torsion in the rotational vestibulo-ocular reflexes. *Prog Brain Res, 171*, 199-206.

Hess, B.J., & Angelaki, D.E. (2003). Gravity modulates Listing's plane orientation during both pursuit and saccades. *J Neurophysiol, 90* (2), 1340-1345.

Hess, B.J., Van Opstal, A.J., Straumann, D., & Hepp, K. (1992). Calibration of three-dimensional eye position using search coil signals in the rhesus monkey. *Vision Res, 32* (9), 1647-1654.

Hore, J., Watts, S., & Vilis, T. (1992). Constraints on arm position when pointing in three dimensions: Donders' law and the Fick gimbal strategy. *J Neurophysiol, 68* (2), 374-383.

Houben, M.M., Goumans, J., & van der Steen, J. (2006). Recording three-dimensional eye movements: scleral search coils versus video oculography. *Invest Ophthalmol Vis Sci, 47* (1), 179-187.

Huey, E.B. (1898). Preliminary experiments in the physiology and psychology of reading. *American Journal of Psychology, 9*, 575-586.

Huey, E.B. (1900). On the psychology and physiology of reading
. *American Journal of Psychology,* (11), 283-302.

Imai, T., Sekine, K., Hattori, K., Takeda, N., Koizuka, I., Nakamae, K., Miura, K., Fujioka, H., & Kubo, T. (2005). Comparing the accuracy of video-oculography and the scleral search coil system in human eye movement analysis. *Auris Nasus Larynx, 32* (1), 3-9.

Judge, S.J., Richmond, B.J., & Chu, F.C. (1980). Implantation of magnetic search coils for measurement of eye position: an improved method. *Vision Res, 20* (6), 535-538.

Klier, E.M., Wang, H., Constantin, A.G., & Crawford, J.D. (2002). Midbrain control of three-dimensional head orientation. *Science, 295* (5558), 1314-1316.

Klier, E.M., Wang, H., & Crawford, J.D. (2001). The superior colliculus encodes gaze commands in retinal coordinates1. *Nat.Neurosci., 4* (6), 627-632.

Knight, T.A., & Fuchs, A.F. (2007). Contribution of the Frontal Eye Field to Gaze Shifts in the Head-Unrestrained Monkey: Effects of Microstimulation. *J Neurophysiol, 97*, 618-634.

Krauzlis, R.J., & Lisberger, S.G. (1994). Temporal properties of visual motion signals for the initiation of smooth pursuit eye movements in monkeys. *J Neurophysiol, 72* (1), 150-162.

Lefevre, P., Bottemanne, I., & Roucoux, A. (1992). Experimental study and modeling of vestibulo-ocular reflex modulation during large shifts of gaze in humans. *Exp Brain Res, 91* (3), 496-508.

Malis, D.D., & Guyot, J.P. (2003). Room tilt illusion as a manifestation of peripheral vestibular disorders. *Ann Otol Rhinol Laryngol, 112* (7), 600-605.

Martinez-Trujillo, J.C., Wang, H., & Crawford, J.D. (2003). Electrical stimulation of the supplementary eye fields in the head-free macaque evokes kinematically normal gaze shifts. *J.Neurophysiol., 89* (6), 2961-2974.

McLaren, J.W., & Hillman, D.E. (1976). Configuration of the cupula during endolymph pressure changes. *Soc. Neuroscience Abs. 2* (p. 1060).

Minken, A.W., Van Opstal, A.J., & van Gisbergen, J.A. (1993). Three-dimensional analysis of strongly curved saccades elicited by double-step stimuli. *Exp Brain Res, 93* (3), 521-533.

Mok, D., Ro, A., Cadera, W., Crawford, J.D., & Vilis, T. (1992). Rotation of Listing's plane during vergence. *Vision Res, 32* (11), 2055-2064.

Munchau, A., & Bronstein, A.M. (2001). Role of the vestibular system in the pathophysiology of spasmodic torticollis. *J Neurol Neurosurg Psychiatry, 71* (3), 285-288.

Rabbitt, R.D., & Damiano, E.R. (1992). A hydroelastic model of macromechanics in the endolymphatic vestibular canal. *Journal of Fluid Mechanics, 238* (-1), 337-369.

Radau, P., Tweed, D., & Vilis, T. (1994). Three-dimensional eye, head, and chest orientations after large gaze shifts and the underlying neural strategies. *J Neurophysiol, 72* (6), 2840-2852.

Raphan, T., Matsuo, V., & Cohen, B. (1979). Velocity storage in the vestibulo-ocular reflex arc (VOR). *Exp Brain Res, 35* (2), 229-248.

Rashbass, C. (1961). The relationship between saccadic and smooth tracking eye movements. *J Physiol, 159*, 326-338.

Robinson, D.A. (1963). A Method of Measuring Eye Movement Using a Scleral Search Coil in a Magnetic Field. *IEEE Trans Biomed Eng, 10*, 137-145.

Robinson, D.A. (1965). The mechanics of human smooth pursuit eye movement. *J Physiol, 180* (3), 569-591.

Robinson, D.A. (1968). Eye movement control in primates. The oculomotor system contains specialized subsystems for acquiring and tracking visual targets. *Science, 161* (847), 1219-1224.

Roy, J.E., & Cullen, K.E. (1998). A neural correlate for vestibulo-ocular reflex suppression during voluntary eye-head gaze shifts. *Nat Neurosci, 1* (5), 404-410.

Rubens, S.M. (1945). Cube-Surface Coil for Producing a Uniform Magnetic Field. *Rev Sci Instr., 16* (9), 243-245.

Ruete, C.G.T. (1845). Lehrbuch der Ophthalmologie für Aerzte und Studirende. Braunschweig: Vieweg.

Schilstra, C., & van Hateren, J.H. (1998a). Stabilizing gaze in flying blowflies. *Nature, 395* (6703), 654.

Schilstra, C., & van Hateren, J.H. (1998b). Using miniature sensor coils for simultaneous measurement of orientation and position of small, fast-moving animals. *J Neurosci Methods, 83* (2), 125-131.

Schor, C.M., Maxwell, J.S., & Graf, E.W. (2001). Plasticity of convergence-dependent variations of cyclovergence with vertical gaze. *Vision Res., 41* (25-26), 3353-3369.

Schwarz, G. (1978). Estimating the dimension of a model. *Annals of Statistics, 6* (3), 461-464.

Stahl, J.S. (2001). Eye-head coordination and the variation of eye-movement accuracy with orbital eccentricity. *Exp Brain Res, 136* (2), 200-210.

Steinhausen, W. (1933). Über die Beobachtung der Cupula in den Bogengangsampullen des Labyrinths des lebenden Hechts. *Pflügers Arch., 232*, 500-512.

Straumann, D., Haslwanter, T., Hepp-Reymond, M.C., & Hepp, K. (1991). Listing's law for eye, head and arm movements and their synergistic control. *Exp Brain Res, 86* (1), 209-215.

Tabak, S., Collewijn, H., Boumans, L.J., & van der Steen, J. (1997). Gain and delay of human vestibulo-ocular reflexes to oscillation and steps of the head by a reactive torque helmet. I. Normal subjects. *Acta Otolaryngol, 117* (6), 785-795.

Thomassen, J.S., Benedetto, G.D., & Hess, B.J. (2010). Decoding 3D search coil signals in a non-homogeneous magnetic field. *Vision Res, 50* (13), 1203-1213.

Tomlinson, R.D., & Bahra, P.S. (1986a). Combined eye-head gaze shifts in the primate. I. Metrics. *J Neurophysiol, 56* (6), 1542-1557.

Tomlinson, R.D., & Bahra, P.S. (1986b). Combined eye-head gaze shifts in the primate. II. Interactions between saccades and the vestibuloocular reflex. *J Neurophysiol, 56* (6), 1558-1570.

Tweed, D. (1997). Visual-motor optimization in binocular control. *Vision Res, 37* (14), 1939-1951.

Tweed, D., Cadera, W., & Vilis, T. (1990). Computing three-dimensional eye position quaternions and eye velocity from search coil signals. *Vision Res, 30* (1), 97-110.

Tweed, D., Fetter, M., Andreadaki, S., Koenig, E., & Dichgans, J. (1992). Three-dimensional properties of human pursuit eye movements. *Vision Res, 32* (7), 1225-1238.

Tweed, D., Glenn, B., & Vilis, T. (1995). Eye-head coordination during large gaze shifts. *J Neurophysiol, 73* (2), 766-779.

Tweed, D., Haslwanter, T., & Fetter, M. (1998). Optimizing gaze control in three dimensions. *Science, 281* (5381), 1363-1366.

Tweed, D., & Vilis, T. (1990). Geometric relations of eye position and velocity vectors during saccades. *Vision Res, 30* (1), 111-127.

Tweed, D., & Vilis, T. (1992). Listing's law for gaze-directing head movements. pp. 387-391): Oxford Univ. Press.

Van Buskirk, W.C., Watts, R.G., & Liu, Y.K. (1976). The fluid mechanics of the semicircular canals. *Journal of Fluid Mechanics, 78* (01), 87-98.

Van Opstal, A.J., & Van Gisbergen, J.A. (1987). Skewness of saccadic velocity profiles: a unifying parameter for normal and slow saccades. *Vision Res, 27* (5), 731-745.

Van Rijn, L.J., & Van den Berg, A.V. (1993). Binocular eye orientation during fixations: Listing's law extended to include eye vergence. *Vision Res, 33* (5-6), 691-708.

von Helmholtz, H. (1867). Handbuch der Physiologischen Optik. 3. Hamburg: Voss.

Wade, N.J. (2007). Scanning the seen: vision and the origins of eye movement research. In: R.P.G. van Gompel, M.H. Fischer, W.S. Murray, & R.L. Hill (Eds.), *Eye Movements: A Window on Mind and Brain* (pp. 31-61). Oxford: Elsevier.

Waespe, W., Henn, V., & Isoviita, V. (1980). Nystagmus slow-phase velocity during vestibular, optokinetic, and combined stimulation in the monkey. *Arch.Psychiatr.Nervenkr., 228* (4), 275-286.

Wells, W.C. (1792). An essay upon single vision with two eyes: Together with experiments and observations on several other subjects in optics. London: Cadell.

Yamauchi, A., Rabbitt, R.D., Boyle, R., & Highstein, S.M. (2002). Relationship between inner-ear fluid pressure and semicircular canal afferent nerve discharge. *J Assoc Res Otolaryngol, 3* (1), 26-44.

6. Curriculum Vitae

Name:	THOMASSEN
First names:	Jakob Skibsted
Date of Birth:	17 May 1979
Nationality:	Danish

Education:

2006- 2011	University of Zürich, Faculty of Natural Sciences. Doctor of Natural Sciences in biomedical engineering at the Vestibulo-Ocular Laboratory, University Hospital Zürich.
2003-2005	University of Aarhus, Faculty of Health Sciences Master of Science in biomedical engineering. Thesis title: “Wavelet Analysis of High Frequency Pressure Fluctuations near Mechanical Heart Valve”
1999-2003	The Engineering College of Aarhus. Bachelor of Science in electrical engineering. Thesis title: “868MHz RF-link til fjernaflæsningssystem”
1995-1998	Horsens Technical High-school. High school degree.